

MODEL-BASED SIMULATIONS OF THE PIERCING PROCESS
IN PIEZO-ICSI

A Dissertation
presented to
the Faculty of the Graduate School
at the University of Missouri-Columbia

In Partial Fulfillment
of the Requirements for the Degree
Doctor of Philosophy

by
YONG GAN
Dr. Zhen Chen, Dissertation Supervisor
MAY 2008

The undersigned, appointed by the dean of the Graduate School, have examined the dissertation entitled

MODEL-BASED SIMULATIONS OF THE PIERCING PROCESS
IN PIEZO-ICSI

presented by Yong Gan,

a candidate for the degree of doctor of philosophy,

and hereby certify that, in their opinion, it is worthy of acceptance.

Professor Zhen Chen

Professor Sam A. Kiger

Professor P. Frank Pai

Professor Stephen Montgomery-Smith

Professor Hani Salim

.....Thanks, Mom and Dad.

ACKNOWLEDGEMENTS

This dissertation would not have been accomplished without the support and contribution of many people. First, I would like to thank my advisor, Professor Zhen Chen, for his guidance, inspiration and patience throughout my Ph.D. study at the University of Missouri-Columbia. Without his help and encouragement, I would never walk so far on the academic road.

Secondly, I am grateful to all other members of my Ph.D. committee, including Professor Sam Kiger, Professor Frank Pai, Professor Hani Salim, and Professor Stephen Montgomery-Smith, for their valuable help in various areas during my doctoral study. Especially, I am thankful to Professor Montgomery-Smith and Professor Pai for their precious opinions of my dissertation.

I also acknowledge Dr. Allen York II and my co-advisor, Timothy Bartel at Sandia National Laboratory, for their stimulating discussions of the Material Point Method and the Equation of State for fluids. I wish to express my appreciation to Dr. Wenqing Hu and Dr. Luming Shen for their suggestions in my research and help in my life. I also thank Craig and Shirley Colbert, Mr. Kenny DeYoung and Mr. Hao Liu for their friendly help.

I also want to thank the National Science Foundation, the Air Force and the Army for their financial support on my doctoral studies at the University of Missouri-Columbia.

Finally, I am deeply indebted to my parents for their endless love, support, encouragement and understanding.

TABLE OF CONTENTS

ACKNOWLEDGEMENTS.....	ii
TABLE OF CONTENTS.....	iii
LIST OF ILLUSTRATIONS.....	vi
LIST OF TABLES.....	x
NOMENCLATURE	xi
ABSTRACT.....	xx
Chapter	
1. INTRODUCTION	1
1.1 <i>In Vitro</i> Fertilization	1
1.2 Piezo-Intracytoplasmic Sperm Injection.....	3
1.3 Objective.....	4
2. LITERATURE REVIEW	6
2.1 Mechanical Models of Biological Cells.....	6
2.1.1 Solid Models.....	7
2.1.2 Cortical Shell-Liquid Core Models (Liquid Drop Models)	8
2.1.3 Tensegrity Model.....	11
2.2 Computational Methods for Fluid-Structure Interaction	12
2.3 Summary.....	22
3. THE MATERIAL POINT METHOD	24
3.1 Introduction.....	24
3.2 Governing Equations and Numerical Implementation of the MPM.....	24
3.3 Numerical Examples.....	32

4. THE MPM FOR FLUID-MEMBRANE INTERACTION	38
4.1 The MPM formulation for Three-dimensional Membranes	38
4.2 The MPM formulation for Fluids	50
4.3 Simulation of Fluid-Membrane Interaction with the MPM.....	55
4.4 Demonstrations	56
4.4.1 One-dimensional shock tube.....	56
4.4.2 Impact between a membrane and an elastic solid.....	63
4.4.3 Simulation of fluid-membrane interaction.....	66
4.5 Summary	69
5. SIMULATIONS OF PIEZO-ICSI	71
5.1 Introduction.....	71
5.2 Equation of State for Medium and Cytoplasm	73
5.3 Constitutive Model of the Mouse Zona Pellucida	77
5.4 The MPM Simulation of the Mouse Zona Piercing in Piezo-ICSI.....	87
5.5 Role of Mercury in the Piercing Process	110
5.6 Summary	118
6. CONCLUDING REMARKS AND FUTURE WORK	119
6.1 Summary	119
6.2 Findings and Conclusions.....	120
6.3 Future Work	122
REFERENCES	123
APPENDIX	
1. LINEAR INTERPOLATION SHAPE FUNCTIONS.....	136

2. RESEARCH PROJECTS UNDERTAKEN BY THE AUTHOR	140
VITA	142

LIST OF ILLUSTRATIONS

Figure	Page
1.1. Procedure of the ICSI experiment (Yanagida et al., 1999).....	2
1.2. Sequence of piezo-ICSI (Yanagida et al., 1999).....	4
2.1. Cortical shell-liquid core model.....	9
2.2. Compound liquid drop model	11
2.3. Sloshing of the water inside the tank (Anghileri et al. 2005)	17
2.4. Interaction between an elastic plate and fluid flow (Antoci et al., 2007)	17
2.5. Flow past a sphere (Yun et al., 2003)	19
2.6. MPM simulation of the airbag impact problem (York II, 1997): (a) Schematic diagram of the airbag impact problem, (b) Displacement of the probe.....	21
3.1. Lagrangian material points and Eulerian mesh in two dimensions	26
3.2. One typical 8-node computational cell	26
3.3. The impact of two bodies.....	33
3.4. The location of point A	33
3.5. The time history of the normal stress in the x -direction at point A: (a) mesh convergence, (b) point convergence.....	34
3.6. A metal bar subject to a step tension	35
3.7. MPM models of a metal bar: (a) $1 \times 1 \times 1$ point per cell, (b) $3 \times 3 \times 3$ points per cell, (c) $5 \times 5 \times 5$ points per cell	36
3.8. The equivalent stress profile along x -direction at different time: (a) $1 \times 1 \times 1$ point per cell, (b) $3 \times 3 \times 3$ points per cell, (c) $5 \times 5 \times 5$ points per cell.....	37
4.1. Viscous fluid droplet model of the oocyte.....	38

4.2. A two-dimensional membrane represented by material points: (a) material point representation in two dimensions, (b) three-dimensional view of the membrane	41
4.3. Determination of tangential angle with the connectivity of material points.....	42
4.4. One-way constitutive model for the membrane wrinkle.....	42
4.5. A sphere triangulated by GTS (http://gts.sourceforge.net/gallery.html)	45
4.6. Calculation of the point normal	46
4.7. Computation of the principal strains in the local tangent plane.....	49
4.8. Illustration of the fluid-membrane interaction in the two-dimensional MPM.....	56
4.9. One-dimensional shock tube problem	58
4.10. Initialization of points in one cell	58
4.11. MPM solutions with no artificial viscosity (averages of material points initialized in one cell)	59
4.12. MPM solutions with artificial viscosity (averages of material points initialized in one cell)	60
4.13. MPM solutions with artificial viscosity (averages of material points initialized in every two consecutive cells).....	62
4.14. MPM solutions with artificial viscosity (averages of material points initialized in every four consecutive cells)	63
4.15. An elastic cuboid impacting a net.....	64
4.16. The z-directional displacement at the central point of the cuboid	65
4.17. Material point position plots for the simulation of a cuboid impacting a net: (a) $t=0.05$ s, (b) $t=0.1$ s, (c) $t=0.15$ s, (d) $t=0.2$ s (0.02 m mesh size).....	66
4.18. Setup of the fluid-membrane interaction problem	67
4.19. Time-history of the z-directional displacement at the central point of the cube.....	68

5.1. Injection pipette and piezo-drill (Ediz and Olgac, 2004).....	72
5.2. Voltage applied to the piezo-drill	73
5.3. Setup of the piezo-ICSI (Ediz and Olgac, 2004)	73
5.4. Schematic diagram of MPM simulations for the ICSI process.....	75
5.5. External mechanical loading function	75
5.6. Time-history of axial displacement of the injection pipette	76
5.7. Effects of c_0 and c_1 on the change of \mathbf{E}^{ed}	79
5.8. Geometry of localized failure condition	83
5.9. The z -directional displacement at the center of the cube	87
5.10. Viscous damping boundary method.....	91
5.11. A boundary point and the grid cell	91
5.12. The piston problem: (a) piston-water interaction example, (b) free boundary and absorbing boundary	91
5.13. The time-histories of σ_{xx} at point p	92
5.14. The indentation on the mouse zona by the injection pipette (Sun et al., 2003)	94
5.15. The MPM model for the simulations of the piercing process in piezo-ICSI (oocyte: cyan, injection pipette: white, medium: red, holding pipette: blue)	97
5.16. Deformation shapes of the oocyte at different times (6 μm cell size and elastodamage model): (a) $t=28 \mu\text{s}$, (b) $t=52 \mu\text{s}$, (c) $t=76 \mu\text{s}$, (d) $t=100 \mu\text{s}$	99
5.17. Deformation shapes of the oocyte at different times (5 μm cell size and elastodamage model): (a) $t=28 \mu\text{s}$, (b) $t=52 \mu\text{s}$, (c) $t=76 \mu\text{s}$, (d) $t=100 \mu\text{s}$	100
5.18. Deformation shapes of the oocyte at different times (4 μm cell size and elastodamage model): (a) $t=28 \mu\text{s}$, (b) $t=52 \mu\text{s}$, (c) $t=76 \mu\text{s}$, (d) $t=100 \mu\text{s}$	101

5.19. Deformation shapes of the oocyte at different times (6 μm cell size and decohesion model): (a) $t=28 \mu\text{s}$, (b) $t=52 \mu\text{s}$, (c) $t=76 \mu\text{s}$, (d) $t=100 \mu\text{s}$	103
5.20. Deformation shapes of the oocyte at different times (5 μm cell size and decohesion model): (a) $t=28 \mu\text{s}$, (b) $t=52 \mu\text{s}$, (c) $t=76 \mu\text{s}$, (d) $t=100 \mu\text{s}$	104
5.21. Deformation shapes of the oocyte at different times (4 μm cell size and decohesion model): (a) $t=28 \mu\text{s}$, (b) $t=52 \mu\text{s}$, (c) $t=76 \mu\text{s}$, (d) $t=100 \mu\text{s}$	105
5.22. Deformation shapes of the oocyte at different times (4 μm cell size and elastodamage model): (a) $t=15 \mu\text{s}$, (b) $t=30 \mu\text{s}$, (c) $t=45 \mu\text{s}$, (d) $t=60 \mu\text{s}$	108
5.23. Deformation shapes of the oocyte at different times (4 μm cell size and decohesion model): (a) $t=15 \mu\text{s}$, (b) $t=30 \mu\text{s}$, (c) $t=45 \mu\text{s}$, (d) $t=60 \mu\text{s}$	109
5.24. Cantilever beam model of the injection micropipette.....	110
5.25. One simply-supported beam subjected to support motion at its left end.....	114
5.26. Time-history of the deflection at the beam center: (a) $\bar{\omega}=5200$, (b) $\bar{\omega}=52000$, (c) $\bar{\omega}=208000$	115
5.27. The triangular support motion	117
5.28. The amplitude of the pipette tip	117

LIST OF TABLES

Table	Page
3.1. Material properties of the aluminum and steel Bodies	34
3.2. Material properties of the bar.....	36
4.1. Dimensions of the cuboid and the net.....	64
4.2. Material properties of the cuboid and the net	64
4.3. Material properties of the cube and the membrane.....	67
5.1. Axial displacement of the pipette	76
5.2. Parameters of elatodamage model for the mouse zona pellucida	94
5.3. Parameters of the stiffened-gas EOS for fluids.....	97
5.4. Total number of material points.....	97
5.5. Physical parameters of the mercury-filled injection pipette	112
5.6. The first six natural frequencies of the mercury-filled injection pipette	113
5.7. Densities of fluids	117

NOMENCLATURE

\mathbf{A}_d	positive definite tensor of material parameters
\mathbf{a}	acceleration vector
\mathbf{a}_i	nodal acceleration vector
a	local sound speed
\mathbf{b}	body force vector
\mathbf{b}_i	external nodal force vector due to the body force
c_p	velocity of the primary wave
c_s	velocity of the secondary wave
c_f	speed of sound in the fluid
c_m	ratio of τ_{nf} to τ_{tf}
\mathbf{E}	isotropic elastic tensor
\mathbf{E}^e	secant stiffness tensor for elastic process
\mathbf{E}^{ed}	secant elastodamage stiffness tensor
\mathbf{E}^d	secant stiffness tensor for damage process
\mathbf{E}_T	tangent stiffness tensor
E	Young's modulus
E_h	hardening modulus

E_s	softening modulus
EI	flexural rigidity of the beam
\mathbf{f}_i^{ext}	external nodal force vector
\mathbf{f}_i^{int}	internal nodal force vector
F^d	flow surface for the decohesion evolution.
f	flow surface for the associated von Mises model
f^d	damage surface function
$f_{i,vis}$	viscous damping force at computational grid nodes ($i=x,y$ and z)
f_n	n th natural frequency
\bar{f}	transverse force applied to the beam
\mathbf{G}_{ip}	gradient of shape function evaluated at material point
G	shear modulus
\mathbf{g}	prescribed displacement vector
h	smoothing length of the smoothed particle hydrodynamics (SPH) method
h_b	boundary layer thickness
\mathbf{I}_3	identity matrix of order 3
I	specific internal energy
I_p	internal state variable corresponding to the peak strength

I_s	internal state variable for the associated von Mises model
J_2	second variant of the deviatoric stress tensor
K	bulk modulus
L_e	effective length
M_p	material point mass
m_i	lumped nodal mass
m_{ij}	consistent nodal mass
\mathbf{n}	vector normal to the moving surface of discontinuity
\mathbf{n}_b	unit outward normal to the boundary of $\partial\Omega_\tau$
\mathbf{n}_i	unit vector normal to triangles on the membrane surface
\mathbf{n}_p	point normal at material points
N^P	total number of membrane material points
N_b	total number of SPH particles
N_i	shape function
N_n	total number of computational grid nodes
N_p	total number of material points
N_{Tri}	total number of triangles surrounding the membrane material point
P	pressure

P_{∞}	fit parameter for stiffened gas equation of state
\mathbf{Q}	direction cosine tensor
\mathbf{Q}^{el}	acoustic tensor of elasticity
q	artificial viscosity used to smooth the oscillation at the shock front
\mathbf{S}	orthogonal rotation matrix for the transformation of the coordinate system
S	damage softening function
S_L	maximum principal strain corresponding to the elastic limit
S_{ij}	viscous damping stresses ($i,j=x,y$ and z)
s	surface area of the membrane
\mathbf{T}	fourth-order tangent stiffness tensor
t	time
t^k	the k th time step
\mathbf{u}	displacement vector
\mathbf{u}^d	decohesion vector
\mathbf{u}_i	nodal displacement vector
U	internal energy per unit volume
U_0	initial energy
U^e	internal energy for elastic process
U^d	internal energy for damage process

u_x	velocity component of material points in the x -direction
u_y	velocity component of material points in the y -direction
u_z	velocity component of material points in the z -direction
\bar{u}_0	reference decohesion
\mathbf{v}	velocity vector
\mathbf{v}_i	nodal velocity vector
\mathbf{v}_p	velocity vector of material points
$\tilde{\mathbf{v}}_i$	nodal velocity vector for the evaluation of the strain increments of material points
V_{cell}	volume of the computational grid cell
v	transverse deflection of the beam
v^*	relative deflection of the beam
v_g	translational deflection of the beam
\mathbf{w}	test function
\mathbf{w}_i	test function at grid nodes
$\bar{\mathbf{w}}$	cross product of the unit point normals at two consecutive time levels
$\hat{\mathbf{w}}$	normalized vector of $\bar{\mathbf{w}}$
\mathcal{W}	kernel function of the smoothed particle hydrodynamics method
\mathbf{X}	position vector at time $t=0$

\mathbf{X}_p	position vector of material points
\mathbf{x}	position vector
\mathbf{x}_i	nodal position vector
Δt	time step
Δx	grid cell size in the x -direction
Δy	grid cell size in the y -direction
Δz	grid cell size in the z -direction
$\Delta \boldsymbol{\varepsilon}_p$	strain increments of material points
$\Delta \boldsymbol{\varepsilon}'_p$	local membrane strain increment tensor
$\Delta \boldsymbol{\sigma}_p$	stress increments of material points
δ	Dirac delta function
$\boldsymbol{\varepsilon}$	strain tensor
$\boldsymbol{\varepsilon}^d$	decohesion strain tensor
$\dot{\boldsymbol{\varepsilon}}^d$	decohesion strain rate tensor
$\boldsymbol{\varepsilon}_p$	total strain tensor of material points
$\dot{\boldsymbol{\varepsilon}}_p$	strain rate tensor of material points
$\boldsymbol{\varepsilon}'_p$	strain tensor of material points in the local normal-tangential coordinate system
$\boldsymbol{\varepsilon}'_{p,pr}$	local membrane strain tensor at the previous time step

ε	strain component
ε_i	i th component of the principal strains ($i=1,2,3$)
ε_{\max}	maximum principal strain
Γ	Grüneisen exponent
γ	ratio of specific heats
λ	bulk viscosity
λ^d	variable parameterizing the development of the decohesion
$\bar{\lambda}$	parameter charactering the loading process
μ	shear viscosity
ν	Poisson's ratio
ρ	mass density
ρ^m	mass per unit area of the membrane
$\bar{\rho}$	mass per unit length of the beam
σ	stress tensor
$\dot{\sigma}$	stress rate tensor
σ^d	deviatoric stress tensor
σ^s	specific stress tensor
σ'_p	stress tensor of material points in the local normal-tangential coordinate system
σ	stress componenet

σ_e	equivalent stress
σ_i	i th component of the principal stresses ($i=1,2,3$)
σ_{kk}	trace of the stress tensor
σ_p	peak strength
σ_y	yield strength
$\bar{\sigma}$	normal stress on the discontinuity surface
$\boldsymbol{\tau}$	stress vector on the decohesion surface
$\boldsymbol{\tau}_b$	prescribed traction vector
$\boldsymbol{\tau}_b^s$	specific traction
$\hat{\boldsymbol{\tau}}_i$	external nodal force vector due to the prescribed traction on the boundary
τ^e	effective traction
τ_{nf}	failure initiation values for pure tension
τ_{tf}	failure initiation values for pure shear
τ_n	normal traction components on the failure surface at the initiation of decohesion
τ_t	tangential traction components on the failure surface at the initiation of decohesion
$\bar{\tau}$	tangential stress on the discontinuity surface
$\bar{\tau}_0$	reference traction

Ω	current configuration of the continuum
ω	state variable parameterizing the damage evolution
ω_n	n th circular frequency
ξ	logical coordinate axis corresponding to the x -coordinate axis
η	logical coordinate axis corresponding to the y -coordinate axis
ς	logical coordinate axis corresponding to the z -coordinate axis
$\partial\Omega$	sum of $\partial\Omega_u$ and $\partial\Omega_\tau$
$\partial\Omega_u$	displacement boundary
$\partial\Omega_\tau$	stress boundary

MODEL-BASED SIMULATIONS OF THE PIERCING PROCESS IN PIEZO INTRACYTOPLASMIC SPERM INJECTION

YONG GAN

Dr. Zhen Chen, Dissertation Supervisor

ABSTRACT

To develop a piezo intracytoplasmic sperm injection (piezo-ICSI) procedure without using mercury, the real physics behind the zona piercing must be understood. An effort has been made to formulate a three-dimensional model for fluid-membrane interaction with the use of the Material Point Method (MPM) so that the mouse zona piercing process could be better simulated for the piezo-ICSI procedure. It is found from the MPM simulations that the lateral vibration of the pipette leads to the noticeable oocyte deformation and the occurrence of the zona failure but no evident deformation and zona failure result from the longitudinal oscillation of the pipette. This outcome confirms the claim that the lateral vibration of the injection pipette plays a key role in the piercing process, and disproves the argument that the axial displacement of the pipette pierces the zona. The lateral vibration of the injection pipette is also analyzed using the finite element method (FEM) to further investigate the role of mercury in the zona piercing. It is shown that the employment of fluids generally reduces the vibration amplitude of the pipette tip and the amplitude decreases with the increase of fluid density. Moreover,

smaller vibration amplitude could be observed as the pulse duration becomes shorter. It can be concluded that the effect of mercury on the piezo-ICSI might yield less oocyte damage due to the reduced amplitude of the pipette tip, and that the development of a piezo-ICSI procedure without using mercury is possible by changing the dynamic characteristics of the injection micropipette and the piezo-drill controller parameters.

CHAPTER 1

INTRODUCTION

1.1 *In Vitro* Fertilization

In vitro fertilization (IVF) is a technique in which the egg cell is fertilized outside of the uterus. The origin of IVF dates back to the work by Min Chueh Chang (1959), where he *in vitro* fertilized a black rabbit's eggs with a black rabbit's sperm, and then cultivated the fertilized eggs in a white rabbit's uterus, and obtained black rabbits. Steptoe and Edwards (1978), inspired by Chang's work, successfully applied the IVF technique for human, which led to the birth of the first test-tube baby in England. Since then, IVF has been widely employed in the treatment of the infertility problems.

However, IVF can not overcome the cases of male infertility, such as low sperm count and sperm with inadequate motility. Thus, a variety of micromanipulation techniques have been proposed to assist fertilization, based on the existing micromanipulation technology developed for the purposes other than the assisted fertilization. Among these techniques, it is the intracytoplasmic sperm injection (ICSI) method that has brought the major breakthrough in assisted fertilization (Mansour, 1998). Hiramoto (1966) performed the first ICSI experiment to prove the occurrence of sperm nuclear decondensation and male pronuclear formation without sperm-oocyte interaction. Interestingly, it was found that the egg fertilized in the ICSI experiment could not only lead to pronuclear formation, but result in embryonic cleavage and normal birth (Hosoi et al., 1988; Iritani, 1989).

Lanzendorf et al. (1988) conducted ICSI for human and Palermo et al. (1992) reported the first human pregnancies following ICSI. ICSI has been extensively and successfully used in the clinical treatments of infertility, such as problems due to severe oligoasthenozoospermia and patients with borderline semen and male immunological infertility (Palermo et al., 1993; van Steirteghem et al., 1993; Payne et al., 1994; Redgment et al., 1994; Mansour et al., 1995). Compared to conventional IVF, ICSI could yield much higher fertilization and pregnancy rates (Palermo et al., 1993; Aboulghar et al., 1996). In a study by Lundin et al. (1996), two 1-day-old oocytes which experienced fertilization failure after IVF were made pregnant by ICSI. Figure 1.1 shows the major steps of a typical ICSI procedure. The selected mature oocyte is initially stabilized by a holding pipette. Then, an injection micropipette containing a sperm pierces the oocyte and is deeply inserted into cytoplasm. Finally, the sperm housed in the pipette is released and the injection micropipette is withdrawn. The oocyte after ICSI will be cultured and monitored for fertilization signs. The ICSI procedure is performed in a microinjection dish, and the oocyte is immersed in a viscous medium to facilitate the operation. As can be seen, the main difference between ICSI and conventional IVF is the way in which the sperm cell is delivered into the oocyte. In conventional IVF, the egg and sperm are placed together for the natural fertilization, while the sperm is directly transferred into the oocyte cytoplasm by laboratory operations in ICSI. Therefore, ICSI is able to treat some male infertility problems for which the conventional IVF method is ineffective.

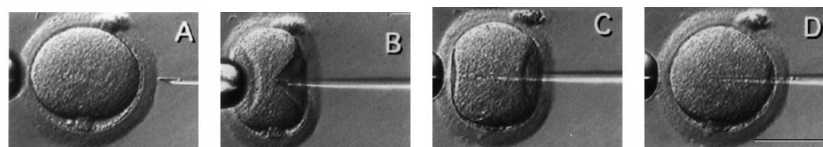


Figure 1.1 Procedure of the ICSI experiment (Yanagida et al., 1999)

1.2 Piezo-Intracytoplasmic Sperm Injection

In general, the employment of human oocytes in ICSI is prohibited as a result of ethical issues, except for the clinical treatment. The mouse oocyte is ideal for ICSI experiments because of the ease of culturing eggs/embryos. However, ICSI in the mouse is extremely difficult and the successful ICSI experiment for mouse eggs has seldom been reported (Kimura and Yanagimachi, 1995). Markert (1983) presented a few mouse blastocysts after ICSI, but many researchers could not repeat his results.

Kimura and Yanagimachi (1995) firstly presented the piezo intracytoplasmic sperm injection (piezo-ICSI) procedure, in which the micropipette is driven by a series of piezo pulses with adjustable frequencies, amplitudes, and durations. With the use of piezo-ICSI, they obtained 80% of survival sperm-injected mouse oocytes, approximately 70% of which developed into blastocysts. Yanagida et al. (1999) applied piezo-ICSI to humans and found higher survival, fertilization and pregnancy rates than those in conventional-ICSI. Takeuchi et al. (2001) compared the efficacy of piezo-ICSI with that of conventional ICSI and concluded that piezo-ICSI yields more favorable fertilization and cleavage rates. It is generally recognized that the conventional ICSI method causes severer damage to the egg than the piezo-ICSI method during the piercing process. The higher success rate, thus, could be obtained for piezo-ICSI. Figure 1.2 shows the sequence of the piezo-ICSI experiment. It is very clear that the oocyte in piezo-ICSI experiences much smaller deformation than that in the conventional ICSI procedure as shown in Figure 1.1.

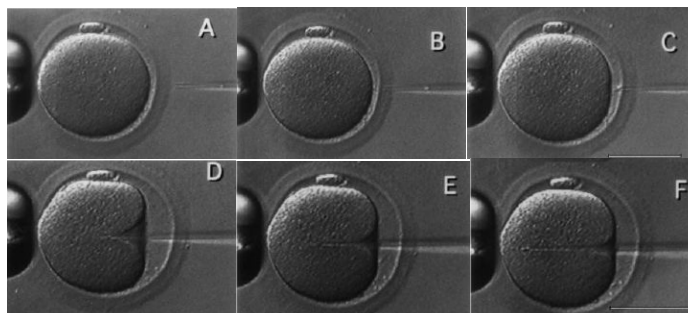


Figure 1.2 Sequence of piezo-ICSI (Yanagida et al., 1999)

1.3 Objective

In the piezo-ICSI procedure, a small amount of mercury in the injection micropipette is found to substantially improve the success rate. The toxicity of mercury, however, may lower the survival and fertilization rates of the egg cell, and result in some defects in the embryo. In spite of this disadvantage, a mercury-filled injection micropipette is commonly used in piezo-ICSI for a higher success rate. Hence, it is desirable to develop a piezo-ICSI procedure without the employment of mercury, for which a better understanding of the role played by mercury in the piercing process of piezo-ICSI is a necessity.

At present, there is no general agreement on the piercing mechanism in piezo-ICSI. In addition, all related simulations have been focused on the micro-dynamics of the injection micropipette subjected to piezo pulses. No work has been done to model the piercing process involving the oocyte, micropipette and medium fluid. As a result, the objective of this research is, through model-based simulations, to investigate the mechanical response of the oocyte in piezo-ICSI, thereby finding out the real physics behind the puncture of the zona pellucida and the effect of mercury on the piercing process. The material point method (MPM), a recently developed spatial discretization

method, is used to simulate the piercing process in piezo-ICSI. An effort is made here to modify the existing MPM algorithm to better simulate thin membranes, fluids and fluid-structure interaction. Moreover, the transient response of the injection micropipette due to piezo pulses is analyzed with the finite element method (FEM) to study the role of mercury in the microdynamics of the micropipette.

The remaining parts of this dissertation are organized as follows. Chapter 2 reviews the mechanical models of biological cells and the numerical methods for fluid-structure interaction problems. The standard algorithm of the MPM is described in Chapter 3. The development and implementation of the three-dimensional MPM formulations for membrane, fluids and fluid-structure interaction are presented in Chapter 4. The MPM simulation of the piercing process in the piezo-ICSI procedure for the mouse oocyte and the vibration analysis of the injection micropipette are given in Chapter 5. The concluding remarks and future work are discussed in Chapter 6.

CHAPTER 2

LITERATURE REVIEW

2.1 Mechanical Models of Biological Cells

As the basic structural and functional unit of living organisms, biological cells take a variety of fundamental functions such as molecule transport, reproduction and metabolism etc. In a physiological circumstance, cells are continuously subjected to physical forces, and thereby experience deformations. This feature could be referred to mechanical properties of cells. The functions of cells are directly influenced by their mechanical environment (Ingber, 2003a and 2003b; Van Vliet et al., 2003). It is believed that the distortion of cells could change cell phases like differentiation, growth and apoptosis. Mechanical forces have been recognized as an important factor for the development and function of the heart and lung, the growth of skin and muscle, the maintenance of cartilage and bone, and the etiology of many debilitating diseases, including hypertension, osteoporosis, asthma and heart failure (Ingber, 2003b). It is also revealed that behaviors required for developmental control, such as growth, differentiation, polarity and motility, are all affected by the physical distortion of cells (Folkman and Moscona, 1978; Ingber et al., 1986; Li et al., 1987; Ingber 1990; Chen et al., 1997; Dike et al., 1999; Parker et al., 2002). On the other hand, mechanical properties of cells could possibly serve as indicators for cellular processes (Elson, 1988) and might be useful as one diagnostic tool for certain medical treatments (Zhou et al., 2004; Suresh

et al., 2005). For example, the cell membrane of oocytes may become stiffer as a result of aging. The parasite causing malaria, *plasmodium falciparum*, could induce the structural change of red blood cells, thus leading to hard cell membrane. Therefore, the interest in mechanical forces as biological indicators and regulators is growing fast recently (Ingber, 2003b). A lot of efforts have been made to investigate the response of cells to mechanical forces via experiments, theoretical studies and numerical simulations. Since the major work in this dissertation is to simulate the piercing process in piezo-ICSI, a brief review of computational models of biological cells is presented in this section.

2.1.1 Solid Models

Some types of cells exhibit behaviors like a solid rather than a liquid. For example, endothelial cells and chondrocytes can not be sucked into a micropipette when the aspiration pressure significantly exceeded the critical suction pressure. Such solid-like properties lay the experimental ground for the solid cell models. Solid models assume that the entire cell is a solid sphere comprising elastic or viscoelastic homogeneous material without the difference between the cortex and the cytoplasm. Solid models have been used to analyze the cell tested by micropipette aspiration (Theret et al. 1988), atomic force microscope (AFM) indentation (Bilodeau, 1992) and cytoindenter (Shin and Athanasiou, 1999).

For cells modeled as a homogeneous solid sphere, a few theories have been developed to characterize their morphological and mechanical properties. When an elastic sphere is subject to one normal load, the radius of the circular contact zone between the sphere and the substrate has been described by Hertz theory in terms of the applied load, the radius

of the sphere and the elastic properties of the contact materials (Johnson, 1985). It is worth noticing that Hertz theory does not take account of the adhesive surface interactions and is only valid for small elastic deformations. Two theories, JKR (Johnson et al., 1971) and DMT (Derjaguin et al., 1975), incorporate the influence of surface forces into the original Hertz theory. JKR theory assumes that there is only an adhesive force within the contact zone between the two continuum bodies, whereas the surface forces considered in DMT theory consist of two parts: the adhesive forces and Van der Waals interaction. Both JKR and DMT are only applicable to small elastic contact cases where the contact radius does not exceed 10% of the particle's radius. It is shown from refined numerical simulations that JKR gives a more favorable description for large and soft bodies with high surface energies, while the DMT theory is more suitable for small and hard solid particles with low surface energies (Greenwood, 1997). Furthermore, the biological cell membrane may exhibit viscoelasticity instead of elasticity and the surface is not perfectly smooth. It is found that the consideration of viscoelasticity yields higher adhesive force (Greenwood and Johnson, 1981) and the presence of surface roughness leads to the decrease of the adhesion (Fuller and Tabor, 1975; Cooper et al., 2000).

2.1.2 Cortical Shell-Liquid Core Models (Liquid Drop Models)

Generally speaking, cortical shell-liquid core models depict cells as an elastic or viscoelastic membrane enclosing liquid, as shown in Figure 2.1. Different properties of the liquid could be chosen corresponding to various types of cells, as presented below.

In a micropipette aspiration experiment, it has been observed that some non-adherent cells such as blood phagocytes are able to continuously deform to flow into the small

micropipette (Evans and Kukan, 1984). Yeung and Evans (1989) developed the Newtonian Liquid Drop Model to simulate the passive flow of liquid-like spherical cells into micropipettes. In the model, the cytoplasm is modeled as the homogeneous Newtonian viscous liquid and the membrane is an anisotropic viscous fluid layer with extensional rigidity only. Based on the Newtonian Liquid Drop Model, Yeung and Evans (1989) derived the close-form solutions to the critical suction pressure and the cell deformation (in terms of the ratio of the projection length to the radius of the pipette) via a variational method. The predicted results have a favorable agreement with the experiments. However, this model is not able to explain the fast elastic recoil in the cell recovery tests and the initial rapid entry in the aspiration test (Evans and Yeung, 1989; Needham and Hochmuth, 1990).

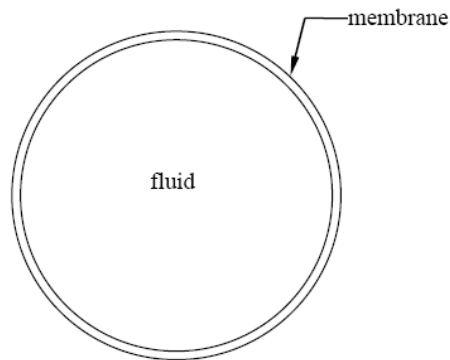


Figure 2.1 Cortical shell-liquid core model

Based on the Newtonian liquid model, the predicted aspiration speed of the cell in the micropipette is almost constant. However, the experiment shows that the aspiration speed would accelerate just before the whole cell flows into the pipette. The shear thinning liquid drop model was then proposed by Tsai et al. (1993) to explain the occurrence of the acceleration. In the model, the fluid viscosity takes the form of a power-law function for the instantaneous mean shear rate. It is shown that this shear thinning model matches

the experiment more favorably than the Newtonian liquid model. In addition, the shear thinning liquid drop model is reasonable for some *in vitro* rheological studies in polymer solutions. Later, Drury and Dembo (2001) demonstrated that the shear thinning liquid drop model is able to basically reflect the dependency of aspiration rate on the pipet diameter and pressure as well, and that the shear thinning is crucial to understanding the pressure dependence of aspiration. It should be noted, however, that the shear thinning has little effect on the small deformation behavior of cells (Fabry et al., 2003). Alternately, Dong et al. (1988) proposed the Maxwell liquid drop model to simulate the fast entry of the cell into the pipette in the micropipette aspiration experiment. The Maxwell liquid drop model comprises a prestressed cortical shell surrounding one Maxwell fluid droplet. Experimental studies have suggested that the Maxwell model is able to explain the initial jump during aspiration as well as the initial rapid recovery of cells held by the pipette for a short time (Dong et al. 1988; Lim et al., 2006). As can be seen, the entire aspiration process of the cell could be simulated by properly combining the liquid drop models mentioned above, in spite of the difficulty of changing the liquid properties at the appropriate time.

It has been known that the nucleus is much stiffer and more viscous than the cytoplasm lying between it and the cell membrane (Dong et al., 1991; Guilak et al., 2000; Caille et al., 2002). Thus, the description of cytoplasm as a homogeneous fluid might not be correct if the nucleus of the cell is comparable to the whole cell in volume. For example, the nucleus of human neutrophils accounts for approximately 21% of the whole cell volume. In such a situation, the compound liquid drop model can serve as a substitution to better reflect the heterogeneity inside the cell. The compound liquid drop model is a

four-layer structure. From the outer portion inward, the successive layers are outer membrane, endoplasm, inner membrane and nucleus, as illustrated in Figure 2.2. Both the outer and inner membranes are assumed to be subject to constant in-plane tensions. The endoplasm and the nucleus are both represented by Newtonian liquids with the nucleus being much more viscous than the endoplasm. The compound liquid drop model can be used to qualitatively explain some experimental observations due to the heterogeneous parts in the cell. For example, the viscosity of the cytoplasm obtained from the aspiration tests might vary with different experimental conditions (Kan et al., 1998).

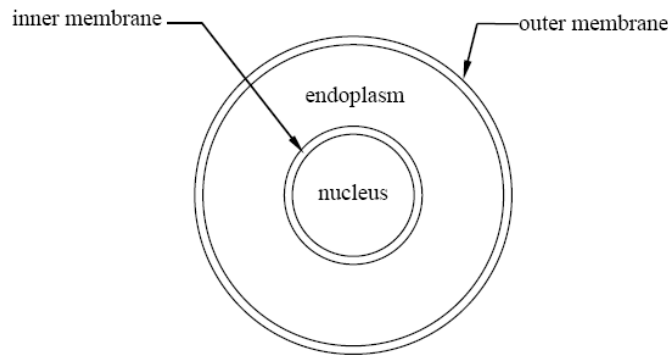


Figure 2.2 Compound liquid drop model

2.1.3 Tensegrity Model

The last mechanical cell model to be mentioned is the tensegrity model. The models discussed earlier are derived on the basis of the continuum assumption, i.e., the structures and properties do not change significantly within the smallest space considered (Zhu et al., 2000). These models are valid for the condition in which the whole-cell scale deformations are of major interest. Therefore, the continuum models have little use in understanding how the cell behavior is affected by the mechanical forces, because they do not include the microstructures of the cell (Ingber, 2003a).

A cellular microstructural model has been developed by introducing the concept of tensegrity structure in the architecture (Ingber and Jamieson, 1982 and 1985; Ingber, 1993, 2003a, 2003b). The cellular tensegrity model is composed of tensile and compressive elements which are subject to the prestress to stabilize the whole cell. As proposed by Ingber (2003a), the tensile forces are borne by cytoskeletal microfilaments and intermediate filaments, and balanced by the internal microtubule struts and extracellular matrix. The tensegrity model has been supported by many studies and invoked to explain a variety of unexplained observations such as lipid micelle formation and morphogenesis of mammalian cells (Ingber, 2003a).

2.2 Computational Methods for Fluid-Structure Interaction

It is very challenging to obtain theoretical solutions to problems with irregular geometry, complex boundary and loading conditions as well as nonlinear constitutive relations. Hence, numerical methods are employed to give approximate solutions by the discretization of the computational domain. Among all the numerical techniques developed so far, the FEM is the most popular one. Drury and Dembo (2001) used the FEM and the Newtonian model to study the aspiration of human neutrophils. Zhou et al. (2004) investigated the micropipette aspiration of malariainfected red blood cells by the FEM. Dong and Skalak (1992) examined the large viscoelastic deformation of leukocytes with the use of the FEM. As can be noticed, one of major difficulties in the simulation of the piercing process in piezo-ICSI lies in the issue due to the fluid-structure interaction. Due to the use of the rigid mesh connectivity, remeshing is required for the FEM as a result of the large deformation of the fluid and the change of the fluid-structure interface.

Hence, an effective numerical method rather than the FEM is required for simulations of the piercing process. So far, a number of numerical methods have been developed for solving fluid-structure interaction problems, as briefly reviewed next.

The deformation of a continuum body can be described in Eulerian or Lagrangian formulation. The Lagrangian description keeps track of each material particle carrying properties such as density, pressure, velocity, strain and stress etc. These properties change as particles advance. The locations of particles at the initial time or the end of the last time step are taken as the reference. Instead of following the material particles, the Eulerian method evaluates the properties at fixed spatial points as time progresses. Basically, the Eulerian method employs a fixed mesh on which the governing equations are solved, whereas the computational grid in the Lagrangian description is attached to the continuum body and deforms with the movement of material particles. Due to the focus on the fixed spatial points, the Eulerian method has an advantage of handling problems with large deformations such as the fluid flow. However, it is very difficult for the Eulerian formulation to define the material interface and boundary and to model history-dependent materials. On the other hand, the Lagrangian method makes it simple to treat materials with history-dependent constitutive equations and to resolve the interface between different materials or phases. When large deformation and discontinuity occur, the employment of the Lagrangian method requires remeshing so that its computational algorithm becomes more complicated.

The simplest way for fluid-structure interaction problems is Euler-Lagrange coupling, i.e., simulating the fluid in the Eulerian formulation and structure in the Lagrangian formulation with the application of boundary conditions at the fluid-structure interface.

The structural solution applies the position and velocity boundary conditions to the fluid, and the structure will be subjected to the pressure boundary condition due to the fluid. An iterative algorithm will be invoked to adjust the prescribed boundary conditions until the fluid pressure and the structure position converge. Many fluid-structure interaction problems have been studied by the Euler-Lagrange coupling or similar methods (Gross and Hofmann, 1977; McMaster, 1984; Prasad and Chou, 1989; Florie et al., 1991; Buijk and Florie, 1991; Buijk and Low, 1993).

The Arbitrary Lagrangian-Eulerian (ALE) formulation is proposed to describe the large material deformation without the requirement of adaptive mesh or remeshing. Unlike the Lagrangian method, the ALE approach allows the mesh to either deform with the material or move at an arbitrary velocity. Thus, the ALE formulation could generate a smooth mesh in the highly distorted region without performing a remeshing and is well suited for simulating the fluid field in the fluid-structure interaction problems. The history of the ALE dates back to the work of Hirt et al. (1974), in which he employed the ALE and the finite difference with an implicit time integration algorithm to conduct the fluid dynamics simulations. Since then, the ALE has been continuously modified and used in the study of a variety of fluid-structure interaction problems. Donea applied the concept of the ALE formulation in the finite element method and demonstrated the potential of the ALE finite element method by the simulation of an underwater explosive detonation (Donea et al., 1977; Donea, 1983). Liu and Ma (1982) used the ALE finite element to find the sloshing motion of the fluid in a three-dimensional cylindrical tank subjected to a 10-second acceleration time history. Nomura (1994) analyzed the nonlinear interaction between the viscous incompressible fluid and a rigid body-spring system with

the ALE finite element approach. Hu et al. (2001) employed the ALE to model the interaction of particles in Newtonian and viscoelastic fluid. Zhang et al. (2003) developed the total ALE formulations using the FEM and successfully solved the problem of the flow past a forced oscillating cylinder. Tanaka and Kashiwama (2006) applied the ALE finite element method in the simulations of the interaction between water and falling objects. Sawada and Hisada (2007) simulated a flapping flexible filament in a flowing soap film with the ALE finite element method and reproduced the three stable dynamical states observed in the experimental study.

Smoothed particle hydrodynamics (SPH) is a particle method originally developed to solve astrophysical problems (Gingold and Monaghan 1977; Lucy 1977). In SPH, the simulated system is modeled as a set of elements or particles with constant mass, and a kernel function is defined such that the kernel function has non-zero values within a circle of radius $2h$ centered on the particle. Then, the conservation equations are discretized by the interpolation of values at the particles. According to Monaghan (1992), the integral interpolant of any function $A(\mathbf{r})$ is expressed as

$$I_n = \int A(\mathbf{r}') W(\mathbf{r} - \mathbf{r}', h) d\mathbf{r}' \quad (2.1)$$

where the integration is over the entire space, \mathbf{r} is the spatial coordinates, $d\mathbf{r}'$ is a differential element volume, and W is the kernel function which satisfies the following equations

$$\int W(\mathbf{r} - \mathbf{r}', h) d\mathbf{r}' = 1 \quad (2.2)$$

$$\lim_{h \rightarrow 0} W(\mathbf{r} - \mathbf{r}', h) = \delta(\mathbf{r} - \mathbf{r}') \quad (2.3)$$

Equation (2.1) could be approximated by a summation defined as

$$\sum_b^{N_b} m_b \frac{A_b}{\rho_b} W(\mathbf{r} - \mathbf{r}_b, h) \quad (2.4)$$

in which index b denotes the particle at $\mathbf{r} = \mathbf{r}_b$, N_b is the total number of particles, m is the mass, ρ is the density, and $A_b = A(\mathbf{r}_b)$. The derivatives of interpolant I_n could be determined by the values at particles and the corresponding derivatives of the differentiable kernel function W . The governing conservation equations could be discretized in the same way. The initially distributed particles evolve according to the SPH approximation of the conservation equations. The physical properties at particles could be updated using numerical integration methods, and the values of variables at any points are interpolated or smoothed using the values at particles and the interpolation function. Based on the properties of the problems to be solved, the kernel function may take various forms (Schoenberg, 1946; Lucy, 1977; Monaghan, 1985 and 2005).

Although it was originally developed for astrophysics, SPH has been extensively applied to different areas, such as quasi-incompressible flows (Monaghan, 1994; Morris et al., 1997), heat conduction (Chen et al., 1999), metal forming (Bonet and Kulasegaram, 2000) and detonation of high explosive (Swegle and Attaway, 1995), etc. Anghileri et al. (2005) simulated the water sloshing in a tank during its impact with the ground by the FEM, Eulerian, ALE, and SPH. The SPH method successfully reproduces the sloshing of the fluid inside the tank and is the most feasible for the analysis of water sloshing among the four models. Figure 2.3 presented the sloshing of the water in the tank by the four methods. However, the major disadvantage of SPH is the large computer time. Antoci et al. (2007) formulated a SPH fluid-structure interaction model in which both the fluid and solid are represented by the SPH particles. With the SPH model, he simulated the outflow

under an elastic sluice gate. The predicted deformations of the elastic structure and the fluid flow are found to have a good agreement with the experiment, as demonstrated in Figure 2.4 (In each snapshot, the left figure is the experiment result and the right one is from the simulation).

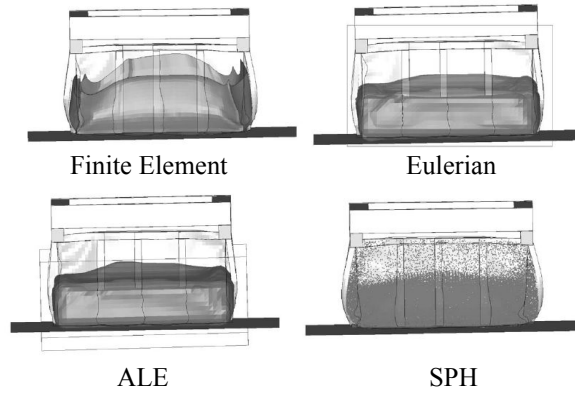


Figure 2.3 Sloshing of the water inside the tank (Anghileri et al. 2005)

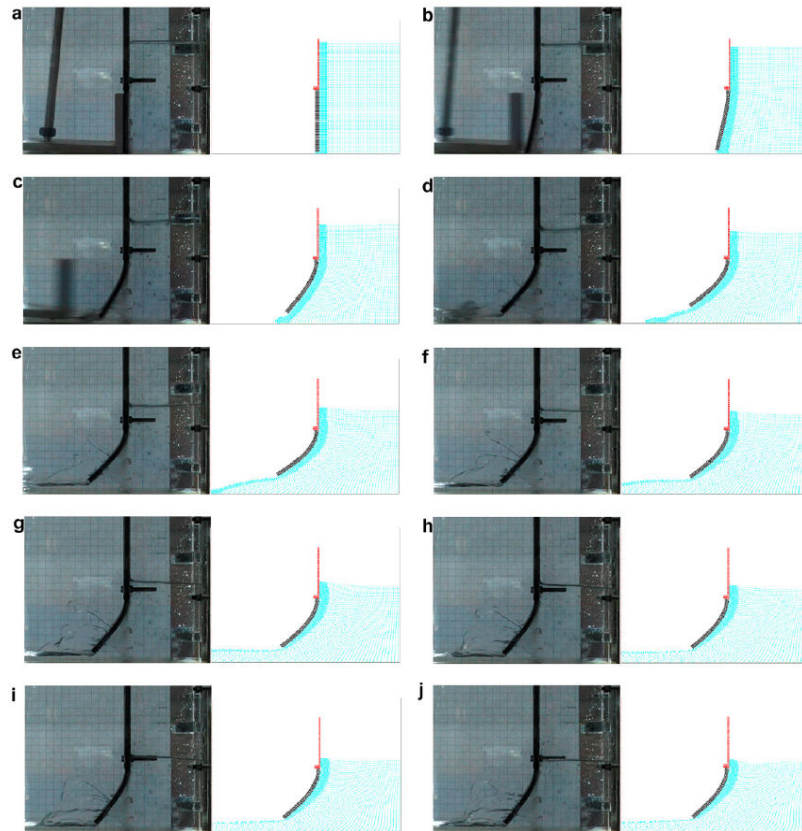


Figure 2.4 Interaction between an elastic plate and fluid flow (Antoci et al., 2007)

Peskin (1972) reported a new method, the immersed boundary (IB) method, for simulations of the blood flow around heart valves. This method takes the Eulerian description for the fluid and the Lagrangian description for the solid. The fluid flow is governed by the Navier-Stokes equations, which are solved on a fixed Eulerian mesh. The immersed structure is modeled as elastic fibers composed of meshless points which move with the local fluid. The stresses of Lagrangian points are calculated with the constitutive equations and transmitted to Eulerian grid nodes through the Dirac delta function (Mittal and Iaccarino, 2005).

Due to its advantage of the automatic handling of the fluid-structure interface, the IB has become a popular tool for the study of various phenomena involving fluid-structure interactions. Peskin and McQueen studied blood flow in the heart with the IB method (Peskin, 1972, 1977; Peskin and McQueen, 1989, 1992, 1994, 1995 and 1996; McQueen and Peskin, 2001). Zhu and Peskin (2003) performed the IB simulations of the motion of two flapping filaments in a flowing soap film. Kalitzin et al. (2003), through their IB simulations of the air flow around a pickup truck, found that a large recirculation occurs in the downstream of the cabin and inside the truck bed. Yun et al. (2003) simulated the flow past a sphere at high Reynolds numbers with the IB method and obtained vortex rings immediately behind the sphere as observed in the experiment, as illustrated in Figure 2.5. Miller and Peskin (2004) modeled a two-dimensional wing with the IB method to investigate the lift generation and vortex dynamics in tiny insect flight. Bagchi et al. (2005) employed a variant of the IB method, the front tracking method, to simulate the aggregation of deformable cells in a shear flow. In addition to exciting potentials in engineering applications, the IB method has made a great contribution to the

development of a number of novel numerical approaches. The immersed finite element method (IFEM) is one of such examples (Zhang et al., 2004; Liu et al., 2006; Zhang and Gay, 2007).

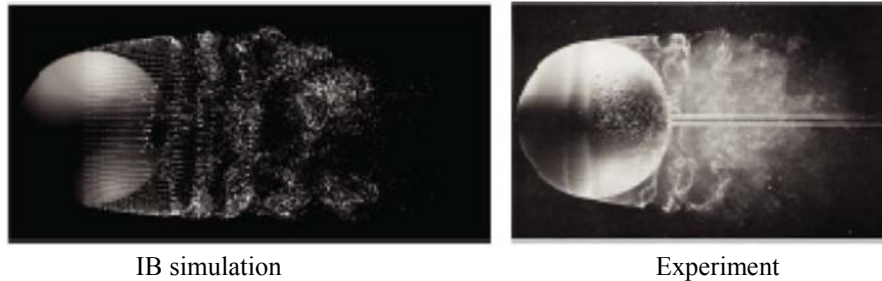


Figure 2.5 Flow past a sphere (Yun et al., 2003)

The IFEM was developed based on the fundamental concept of the IB method, along with some features of the extended immersed boundary method (EIBM) and the reproducing kernel particle method (RKPM). For a structure totally immersed in the fluid, the solid is described using the Lagrangian formulation in the IFEM and the Eulerian description is used for the fluid. The IFEM introduces the artificial fluid which exists in the solid domain so that the fluid and solid have independent meshes and the equations for the fluid and solid are solved separately. Within the overlapping domain in which the solid and the artificial fluid coexist, the RKPM delta function is employed to couple the fluid and solid. The velocity at a solid node is updated by the interpolation of the velocities at its surrounding fluid nodes, and the interaction forces calculated at a solid node will be distributed to its influencing fluid nodes. With the interpolation algorithm described above, existing codes could be easily tailored for fluid-structure interaction problems.

The IFEM has been successfully applied in the simulations of the biological system at various scale levels. Liu et al. (2006) conducted the IFEM simulation of the valve-

viscous fluid interaction with a rubber sheet representing the heart valve. The displacement of the rubber sheet obtained by the IFEM exhibits an excellent agreement with that observed in the experiment. Gay et al. (2006) studied the process of the deployment of the coronary stent by a polyamide balloon with the IFEM. Liu et al. (2004) investigated the behaviors of the red blood cell (RBC) aggregation and its effects on the blood rheology with a combination of the protein molecular potentials and the IFEM, in which the Morse potential is adopted to derive the cell-cell adhesive/repulsive forces. However, some assumptions made in the development of the IFEM restrain its potentials in engineering applications. For example, the fluid and the solid are incompressible, and the solid must be entirely immersed in the fluid throughout the simulation. Thus, the IFEM might not be able to solve problems involving compressible materials and partially immersed structures.

Harlow developed the Particle-in-Cell (PIC) method for fluid dynamics problems at Los Alamos National Laboratory (Harlow, 1964). The PIC uses Lagrangian mass particles to represent the fluid, and the particles move through an Eulerian grid throughout the deformation history. The properties of the fluid are temporarily assigned to particles for the convection of the information from one cell to another cell of the grid. The equations of motion are solved on the Eulerian grid and the solutions are then mapped to the surrounding particles. Based on the use of the PIC in plasma simulation (McCrory et al., 1977; Leboeuf et al. 1979; Dawson, 1983), Brackbill and Ruppel (Brackbill and Ruppel, 1986; Brackbill, 1987, 1988 and 1991) developed a low-dissipation PIC algorithm for fluid flow, FLIP, in which each mass particle carries its

state variables while the grid takes no permanent information and works for the purpose of computational convenience.

According to the FLIP algorithm, Sulsky et al. (1994, 1995) developed the MPM for solid mechanics. The MPM follows the FLIP algorithm to solve the equations of motion on an Eulerian grid. The strains at material particles are evaluated from the velocities at grid nodes, and the stresses at solid points are calculated with the constitutive equations. Later, York II (1997) successfully modified the original MPM algorithm to simulate thin membranes and compressible fluids. Since the equations of motion are solved on the computational grid nodes, the MPM could handle the fluid-structure interaction without the consideration of the interface between different materials. An example of the fluid-structure interaction simulation by the MPM is the airbag impact problem (York II, 1997). Figure 2.6(a) shows the problem of an inflated airbag impacted by a probe, and the displacement of the probe is presented in Figure 2.6(b). It can be seen that the MPM results favorably agree with those by the experiment and the FEM.

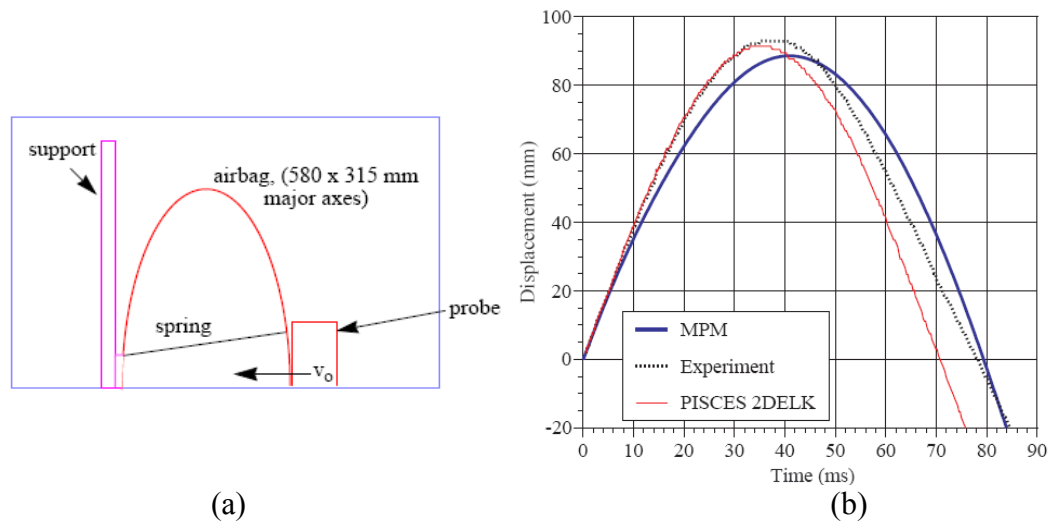


Figure 2.6 MPM simulation of the airbag impact problem (York II, 1997): (a) Schematic diagram of the airbag impact problem, (b) Displacement of the probe

2.3 Summary

It is estimated that there are 100 trillion cells in a human body. Different types of cells have different biological functions and exhibit various responses to mechanical forces. Therefore, a unified mechanical cell model for any kind of cell does not exist. The proper formulation of a cell model should be based on the experimental observation and the loading situation. Several mechanical models of biological cells, such as solid models, liquid drop models, compound liquid drop model and tensegrity model, have been proposed on the basis of experiments and computer simulations.

In the experimental and physiological circumstances, any cell is immersed in the bio-fluid. Thus, the interactions between the cell membrane and fluids inside and outside of the cell must be considered in computer simulations. The fluid-structure interaction is still a challenging problem in computational mechanics. Many approaches for simulating the fluid-structure interaction, such as the Euler-Lagrange coupling method, the IB and the IFEM, solve the structure and the fluid separately, and couple the fluid and the structure with the interpolation of the velocity and force at the interface. Due to the Lagrangian mesh used for the structure, the material failure may require frequent remeshing for this kind of methods. As one of meshfree particle methods, the SPH method has been successfully employed to solve various fluid-structure interaction problems. However, for the cases with large deformations and impulsive loadings, the SPH particles are usually highly disordered, and the obtained results are not reliable and accurate (Liu and Liu, 2003). On the other hand, the MPM combines the advantages of Lagrangian and Eulerian descriptions of the material. The equations of motion are solved on the background Eulerian mesh which carries no permanent information of state

variables. The coupling of the fluid and the structure are automatically treated on the background grid mesh without resolving the fluid-structure interface. Moreover, the material discontinuities could be easily tracked in the MPM due to the use of Lagrangian material particles. In summary, the MPM appears to be an effective numerical method for the simulation of the piercing process in piezo-ICSI involving the fluid-structure interaction and the penetration through cell membrane, although much work remains to be done for general applications.

CHAPTER 3

THE MATERIAL POINT METHOD

3.1 Introduction

The essential idea of the MPM is to take advantage of both the Eulerian and Lagrangian methods while avoiding the shortcomings of each. In the MPM, the material is discretized by a set of material points, each of which carries the material properties and is tracked throughout the deformation history. The deformation of the continuum, hence, is described by the movement of the Lagrangian material points. One Eulerian background mesh is constructed to solve the equations of motion, and the internal state variables carried by material points are updated by the interpolation of the solutions at the mesh nodes. With the deformation history recorded at material points for the given history-dependent constitutive equations, the MPM is able to handle engineering problems with discontinuity, large deformation and multiple materials, such as impact/contact, penetration and perforation, and fluid-structure interactions, as demonstrated by Sulsky et al. (1991, 1994 and 1995) and York II (1997).

In the following sections, the governing equations and numerical algorithm of the MPM are first outlined, and the application of the MPM to solid mechanics is then demonstrated by numerical examples.

3.2 Governing Equations and Numerical Implementation of the MPM

The conservation of mass and momentum can be formulated as follows

$$\frac{d\rho}{dt} + \rho \nabla \cdot \mathbf{v} = 0 \quad (3.1)$$

$$\rho \mathbf{a} = \nabla \cdot \boldsymbol{\sigma} + \rho \mathbf{b} \quad (3.2)$$

where ρ is the mass density, $\mathbf{a}(\mathbf{x}, t)$ is the acceleration, $\mathbf{v}(\mathbf{x}, t)$ is the velocity, $\mathbf{b}(\mathbf{x}, t)$ is the body force, and $\boldsymbol{\sigma}(\mathbf{x}, t)$ is the symmetric stress tensor. The vector \mathbf{x} is the current position at time t of the material which started at position \mathbf{X} at time $t=0$. Equations (3.1) and (3.2) can be solved numerically with given initial conditions and appropriate conditions on the boundary $\partial\Omega$. The conservation of energy is necessary if the heat transfer is noticeable. However, the energy equation is not considered here due to the negligible thermal effect on the piezo-ICSI procedure. The boundary conditions take the form of

$$\mathbf{u}(\mathbf{x}, t) = \mathbf{g}(t) \quad \text{on } \partial\Omega_u$$

$$\boldsymbol{\sigma}(\mathbf{x}, t) \cdot \mathbf{n}_b = \boldsymbol{\tau}_b(t) \quad \text{on } \partial\Omega_\tau$$

where \mathbf{n}_b denotes the unit outward normal to the boundary, the displacement $\mathbf{g}(t)$ and traction $\boldsymbol{\tau}_b(t)$ are prescribed on $\partial\Omega_u$ and $\partial\Omega_\tau$, respectively. With the small deformation assumption, a strain rate tensor is defined to be

$$\frac{d\boldsymbol{\varepsilon}}{dt} = \frac{1}{2} [\nabla \mathbf{v} + (\nabla \mathbf{v})^T] \quad (3.3)$$

which can be employed to update the stress at any material point with the use of an appropriate constitutive model.

As shown in Figure 3.1, a continuum body is divided into a finite set of mass points. Each point contains a fixed amount of mass at all times. For a finite collection of N_p material points with a fixed mass M_p at each point, it follows that

$$\rho(\mathbf{x}, t) = \sum_{p=1}^{N_p} M_p \delta(\mathbf{x} - \mathbf{X}_p(t)) \quad (3.4)$$

where δ is the Dirac delta function, and $\mathbf{X}_p(t)$ is the position of material point p at time t . Since M_p is fixed, the mass conservation equation, Equation (3.1), is automatically satisfied. Through multiplying Equation (3.2) by a test function \mathbf{w} and integrating over the current configuration Ω , we obtain

$$\int_{\Omega} \rho \mathbf{w} \cdot \mathbf{a} d\Omega = - \int_{\Omega} \rho \boldsymbol{\sigma}^s : \nabla \mathbf{w} d\Omega + \int_{\partial\Omega_\tau} \boldsymbol{\tau}_b \cdot \mathbf{w} dS + \int_{\Omega} \rho \mathbf{w} \cdot \mathbf{b} d\Omega \quad (3.5)$$

with $\rho \boldsymbol{\sigma}^s = \boldsymbol{\sigma}$. The combination of Equations (3.4) and (3.5) yields

$$\begin{aligned} \sum_{p=1}^{N_p} M_p \mathbf{w}(\mathbf{X}_p(t), t) \cdot \mathbf{a}(\mathbf{X}_p(t), t) &= - \sum_{p=1}^{N_p} M_p \boldsymbol{\sigma}^s(\mathbf{X}_p(t), t) : \nabla \mathbf{w}(\mathbf{x}, t) |_{\mathbf{x}=\mathbf{X}_p(t)} + \int_{\partial\Omega_\tau} \mathbf{w} \cdot \boldsymbol{\tau}_b dS \\ &+ \sum_{p=1}^{N_p} M_p \mathbf{w}(\mathbf{X}_p(t), t) \cdot \mathbf{b}(\mathbf{X}_p(t), t) \end{aligned} \quad (3.6)$$

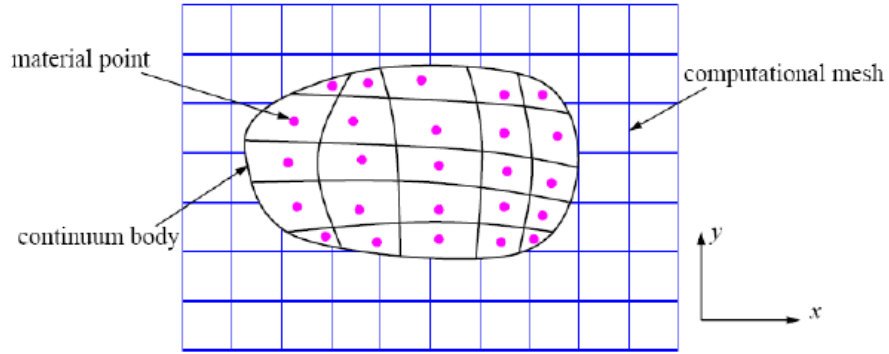


Figure 3.1 Lagrangian material points and Eulerian mesh in two dimensions

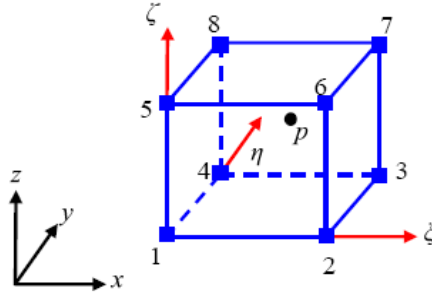


Figure 3.2 One typical 8-node computational cell

One background computational mesh shown in Figure 3.1 is defined to calculate the gradient terms in the MPM. The background mesh is composed of a set of 4-node cells for two-dimensional problems or constructed of 8-node cells in three dimensions. Figure 3.2 demonstrated a typical 8-node cell and the definition of the natural coordinate system. With the use of the conventional 4-node or 8-node FEM shape functions $N_i(\mathbf{x})$ ($i=1,2, \dots, N_n$) (York II, 1997; Appendix A1), the field variables and test function are computed by the following interpolation equations

$$\mathbf{x} = \sum_{i=1}^{N_n} \mathbf{x}_i(t) N_i(\mathbf{x}) \quad (3.7)$$

$$\mathbf{u}(\mathbf{x}, t) = \sum_{i=1}^{N_n} \mathbf{u}_i(t) N_i(\mathbf{x}) \quad (3.8)$$

$$\mathbf{v}(\mathbf{x}, t) = \sum_{i=1}^{N_n} \mathbf{v}_i(t) N_i(\mathbf{x}) \quad (3.9)$$

$$\mathbf{a}(\mathbf{x}, t) = \sum_{i=1}^{N_n} \mathbf{a}_i(t) N_i(\mathbf{x}) \quad (3.10)$$

$$\mathbf{w}(\mathbf{x}, t) = \sum_{i=1}^{N_n} \mathbf{w}_i(t) N_i(\mathbf{x}) \quad (3.11)$$

where $\mathbf{x}_i(t)$, $\mathbf{u}_i(t)$, $\mathbf{v}_i(t)$ and $\mathbf{a}_i(t)$ are the nodal coordinates, displacements, velocities and accelerations at time t , respectively, $\mathbf{w}_i(t)$ is the test function at grid nodes, and N_n is the total number of computational grid nodes. Therefore, Equation (3.6) at time t^k ($k=1, 2, 3 \dots$) becomes

$$\sum_{i=1}^{N_n} \mathbf{w}_i^k \cdot \sum_{j=1}^{N_n} m_{ij}^k \mathbf{a}_j^k = - \sum_{i=1}^{N_n} \mathbf{w}_i^k \cdot \sum_{p=1}^{N_p} M_p \boldsymbol{\sigma}_p^{s,k} \cdot \nabla N_i(\mathbf{x}) \big|_{\mathbf{x}=\mathbf{x}_p^k} + \sum_{i=1}^{N_n} \mathbf{w}_i^k \cdot \boldsymbol{\tau}_i^k + \sum_{i=1}^{N_n} \mathbf{w}_i^k \cdot \mathbf{b}_i^k \quad (3.12)$$

where superscript k denotes the evaluation at time t^k , and also

$$m_{ij}^k = \sum_{p=1}^{N_p} M_p N_i(\mathbf{X}_p^k) N_j(\mathbf{X}_p^k) \quad (3.13)$$

$$\hat{\boldsymbol{\tau}}_i^k = \int_{\partial\Omega_\tau} N_i(\mathbf{x}) \boldsymbol{\tau}_b(\mathbf{x}, t^k) dS \quad (3.14)$$

$$\boldsymbol{\sigma}_p^{s,k} = \boldsymbol{\sigma}^s(\mathbf{X}_p^k, t^k) \quad (3.15)$$

$$\mathbf{b}_i^k = \sum_{p=1}^{N_p} M_p \mathbf{b}(\mathbf{X}_p, t) N_i(\mathbf{X}_p^k) \quad (3.16)$$

Because the components of \mathbf{w}_i^k are arbitrary except those corresponding to the essential boundary conditions, the weak form of the governing differential equations then reduces to

$$\sum_{j=1}^{N_n} m_{ij}^k \mathbf{a}_j^k = \mathbf{f}_i^{\text{int},k} + \mathbf{f}_i^{\text{ext},k} \quad (3.17)$$

with

$$\mathbf{f}_i^{\text{int},k} = - \sum_{p=1}^{N_p} M_p \mathbf{G}_{ip}^k \cdot \boldsymbol{\sigma}_p^{s,k} \quad (3.18)$$

$$\mathbf{f}_i^{\text{ext},k} = \mathbf{b}_i^k + \hat{\boldsymbol{\tau}}_i^k \quad (3.19)$$

$$\mathbf{G}_{ip}^k = \nabla N_i(\mathbf{X}_p^k) \quad (3.20)$$

With the use of the consistent mass matrix as defined in Equation (3.13), large computational cost will be spent on the inversion of the matrix. For simplicity, the consistent mass m_{ij}^k is replaced with the lumped mass m_i^k , namely,

$$m_i^k = \sum_{p=1}^{N_p} M_p N_i(\mathbf{X}_p^k) \quad (3.21)$$

Then, Equation (3.17) becomes

$$\sum_{i=1}^{N_n} m_i^k \mathbf{a}_i^k = \mathbf{f}_i^{\text{int},k} + \mathbf{f}_i^{\text{ext},k} \quad (3.22)$$

By solving Equation (3.22), the nodal accelerations at discrete time t^k are obtained. The grid node velocities at time level $k+1$, \mathbf{v}_i^{k+1} , are then calculated by

$$\mathbf{v}_i^{k+1} = \mathbf{v}_i^k + \Delta t \mathbf{a}_i^k \quad (3.23)$$

$$\Delta t = t^{k+1} - t^k \quad (3.24)$$

Thus, the positions and velocities of the material points are updated as follows

$$\mathbf{X}_p^{k+1} = \mathbf{X}_p^k + \Delta t \sum_{i=1}^8 \mathbf{v}_i^k N_i(\mathbf{X}_p^k) \quad (3.25)$$

$$\mathbf{v}_p^{k+1} = \mathbf{v}_p^k + \Delta t \sum_{i=1}^8 \mathbf{a}_i^k N_i(\mathbf{X}_p^k) \quad (3.26)$$

where \mathbf{v}_p are position and velocity vectors at material point p , respectively. The strain increments at material points $\Delta \boldsymbol{\varepsilon}_p$ are updated with the new nodal velocities $\tilde{\mathbf{v}}_i^{k+1}$ and gradient \mathbf{G}_{ip}^{k+1}

$$\Delta \boldsymbol{\varepsilon}_p = \frac{\Delta t}{2} \sum_{i=1}^8 \left[\mathbf{G}_{ip}^k \tilde{\mathbf{v}}_i^{k+1} + (\mathbf{G}_{ip}^k \tilde{\mathbf{v}}_i^{k+1})^T \right] \quad (3.27)$$

with $\tilde{\mathbf{v}}_i^{k+1}$ being computed by

$$\sum_{i=1}^{N_n} (m \tilde{\mathbf{v}})_i^{k+1} = \sum_{p=1}^{N_p} m_p \mathbf{v}_p^{k+1} N_i(\mathbf{x}_p^k) \quad (3.28)$$

As can be seen from Equations (3.25)-(3.26), an explicit time integrator is used to update the velocity and position of material points. To ensure numerical stability, a time step should not be larger than the critical time step, i.e., the value of the smallest cell size divided by the wave speed of the material. Once the strain increments are determined by

Equation (3.27), the corresponding stress increment could be found through an appropriate constitutive model as

$$\Delta \boldsymbol{\sigma}_p = \mathbf{E}_T : \Delta \boldsymbol{\varepsilon}_p \quad (3.29)$$

where $\Delta \boldsymbol{\sigma}_p$ are the stress increments at point p and \mathbf{E}_T is the fourth-order tangent stiffness tensor derived from the constitutive model. The computational background mesh used during the current time step might be discarded and replaced with a newly defined one, if desired, for the next computation cycle. The detailed numerical algorithm of the MPM is summarized as follows:

(1) Construct the background grid, and initialize material point locations, velocities, masses,

(2) At time level $k=1, 2, \dots$, map momentum, mass, and stresses at each material point to the grid nodes,

$$m_i^k = \sum_{p=1}^{N_p} M_p N_i(\mathbf{x}_p^k) \quad (3.30)$$

$$(m_i \mathbf{v}_i)^k = \sum_{p=1}^{N_p} (M_p \mathbf{v}_p^k) N_i(\mathbf{x}_p^k) \quad (3.31)$$

$$\mathbf{f}_i^{\text{int},k} = - \sum_{p=1}^{N_p} M_p \mathbf{G}_{ip}^k \cdot \boldsymbol{\sigma}_p^{s,k}$$

(3) Apply the boundary conditions to grid nodes, and compute the nodal forces,

$$\mathbf{f}_i^k = \mathbf{f}_i^{\text{int},k} + \mathbf{f}_i^{\text{ext},k} \quad (3.32)$$

(4) Update the momenta at grid nodes,

$$(m\mathbf{v})_i^{k+1} = (m\mathbf{v})_i^k + \mathbf{f}_i^k \Delta t \quad (3.33)$$

(5) Map nodal velocities to points, and update the point locations,

$$\mathbf{v}_p^{k+1} = \sum_{i=1}^{N_n} \frac{(m\mathbf{v})_i^{k+1}}{m_i^k} N_i(\mathbf{x}_p^k) \quad (3.34)$$

$$\mathbf{X}_p^{k+1} = \mathbf{X}_p^k + \mathbf{v}_p^{k+1} \Delta t \quad (3.35)$$

(6) Map nodal accelerations to points and compute the point velocities,

$$\mathbf{a}_p^k = \sum_{i=1}^{N_n} \frac{\mathbf{f}_i^k}{m_i^k} N_i(\mathbf{x}_p^k) \quad (3.36)$$

$$\mathbf{v}_p^{k+1} = \mathbf{v}_p^k + \mathbf{a}_p^k \Delta t \quad (3.37)$$

(7) Map the updated point momenta to nodes and find the updated nodal velocities,

$$(m_i \mathbf{v}_i)^{k+1} = \sum_{p=1}^{N_p} (M_p \mathbf{v}_p^{k+1}) N_i(\mathbf{x}_p^k) \quad (3.38)$$

$$\tilde{\mathbf{v}}_i^{k+1} = \frac{(m_i \mathbf{v}_i)^{k+1}}{m_i^k} \quad (3.39)$$

(8) Apply essential boundary conditions to nodes and compute the strain increments at material points with the nodal velocities given in step (7),

$$\Delta \boldsymbol{\varepsilon}_p = \frac{\Delta t}{2} \sum_{i=1}^{N_n} \left[\mathbf{G}_{ip}^k \tilde{\mathbf{v}}_i^{k+1} + (\mathbf{G}_{ip}^k \tilde{\mathbf{v}}_i^{k+1})^T \right] \quad (3.40)$$

(9) Update the stresses at material points,

$$\boldsymbol{\sigma}_p^{k+1} = \boldsymbol{\sigma}_p^k + \Delta \boldsymbol{\sigma}_p \quad (3.41)$$

$$\Delta \boldsymbol{\sigma}_p = \mathbf{T} : \Delta \boldsymbol{\varepsilon}_p \quad (3.42)$$

(10) Identify which cell each point belongs to, and update the natural coordinates of the material point and time level,

(11) Go back to step (2) unless the required computation time is reached.

In Equations (3.34), (3.36) and (3.39), m_i^k appears as a denominator. To avoid floating-point problems, Equations (3.34), (3.36) and (3.39) are not solved at nodes i if m_i^k is less than a prescribed small positive number (1.0×10^{-30} in our code based on the given machine precision).

3.3 Numerical Examples

To be an efficient numerical method, the MPM must bear two basic features, i.e., numerical stability and convergence. The stability of the MPM can be ensured by aptly choosing the time step if the explicit time integration method is used. On the other hand, the convergence of the MPM can be demonstrated through computational experiments. Since a continuum body is represented by the Lagrangian material points and the equations are solved on an Eulerian mesh, the convergence of MPM will be examined in mesh-based and point-based ways. The former way considers the different computational mesh cell sizes with the fixed number of points in each cell. In the latter case, the cell size is constant while the number of points contained in each cell varies.

Figure 3.3 shows two quadrilateral metal bodies in the x - y plane. One is aluminum and another is steel. Both of them have a width of 0.1m and a height of 0.3m. Initially, the steel body is taken to be a stationary target and the aluminum one is moving towards the target at a velocity of 10 m/s. For the case of mesh convergence, each background square cell contains one material point, and the cell sizes of 0.01m, 0.005m and 0.002m are used. In the examination of the point convergence, the side length of the computational square cell is fixed at 0.01m while each cell contains 1, 4, or 9 material points. The time steps of 1.0×10^{-7} s and 1.0×10^{-6} s are respectively used for the mesh-based case and the point-

based case, and the total simulation time is 3.0×10^{-5} s for both cases. The material properties are listed in Table 3.1 with linear elasticity being assumed and the two-dimensional MPM is employed with the plane strain assumption. As illustrated in Figure 3.4, the time history of the normal stress along the x -direction σ_x at point A is tracked during the simulation period. Figure 3.5 shows the time histories of σ_x at point A for both mesh convergence and point convergence cases. As can be seen from the figures, the MPM is both mesh and point convergent. The comparison between Figure 3.5(a) and Figure 3.5(b), however, suggests that increasing material points gives more favorable results than the employment of the smaller mesh cell size in this impact problem.

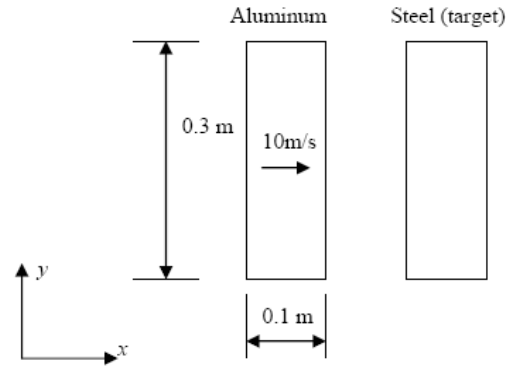


Figure 3.3 The impact of two bodies

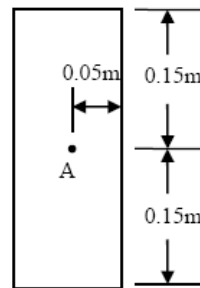


Figure 3.4 The location of point A

Table 3.1 Material properties of the aluminum and steel Bodies

Material	Young's modulus (10^{10}N/m^2)	Density (kg/m^3)	Poisson's ratio
Aluminum	7.0	2700	0.33
Steel	20.0	7800	0.3

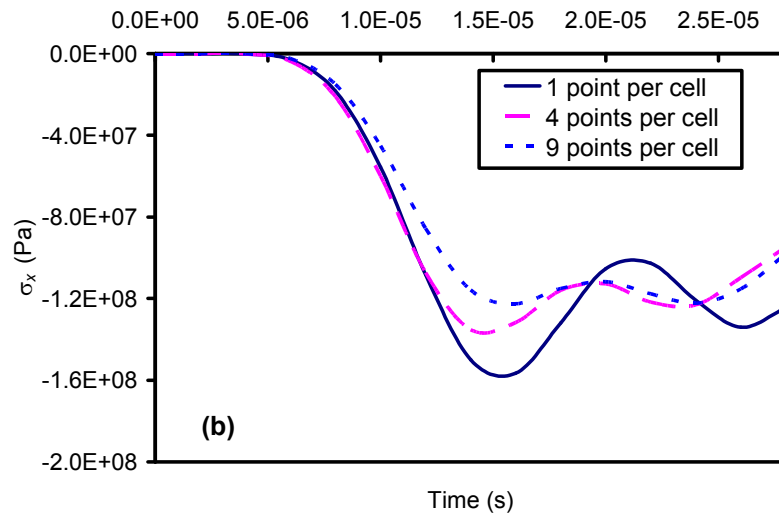
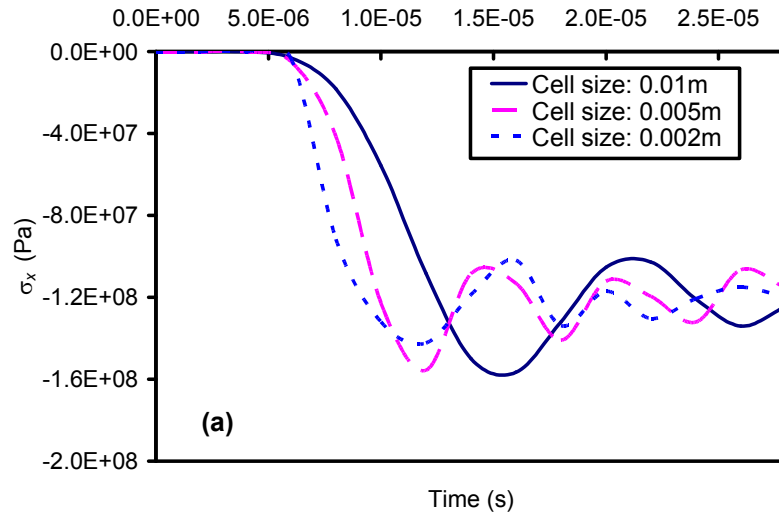


Figure 3.5 The time history of the normal stress in the x -direction at point A: (a) mesh convergence, (b) point convergence

The second example is a problem of the stress wave propagation in a bar. As shown in Figure 3.6, a 10m-long metal bar is subject to a step tensile stress of 200MPa at both ends. The wave propagation problem is solved using the three-dimensional MPM. The material properties of the metal bar are listed in Table 3.2 and the associated elastic-perfect plastic von Mises model is employed in this example. The computational background mesh is composed of 8-node cells, each of which has a side length of 0.2m, 1m and 1m along the x -, y - and z -directions, respectively. As shown in Figure 3.7, three MPM models are considered: (1) $1 \times 1 \times 1$ point (x -, y - and z -direction), (2) $3 \times 3 \times 3$ points (x -, y - and z -direction), (3) $5 \times 5 \times 5$ points (x -, y - and z -direction) are respectively initialized in each cell. The time step of 1.0×10^{-5} s is used for all simulations.

Figure 3.8 gives the profile of the equivalent stress σ_e along the x -direction at different times. Each data point in the plot is corresponding to the averages of material points initialized in each cell. As can be seen from the figure, the problem is elastic before the tensile stress waves meet in the center of the bar ($t=0.25L/c$ and $0.5L/c$, $L=10$ m, $c=5062$ m/s). When the tensile stress waves meet, the plasticity is invoked and the stress keeps equal to the yield stress 300MPa because of the perfect plasticity ($t=0.75L/c$).

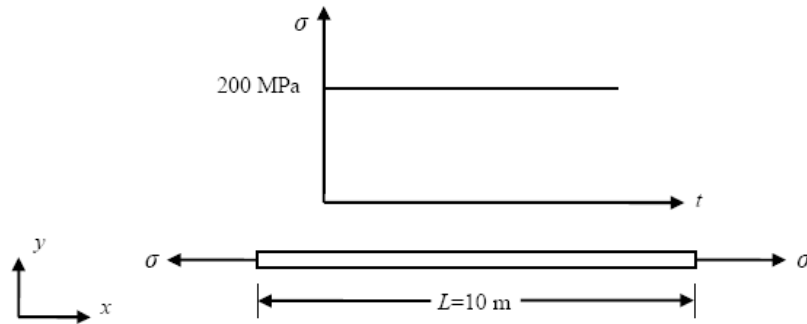


Figure 3.6 A metal bar subject to a step tension

Table 3.2 Material properties of the bar

Young's modulus (MPa)	Poisson's ratio	Density (kg/m ³)	Yield stress (MPa)	Wave speed c (m/s)
72000	0	2810	300	5062

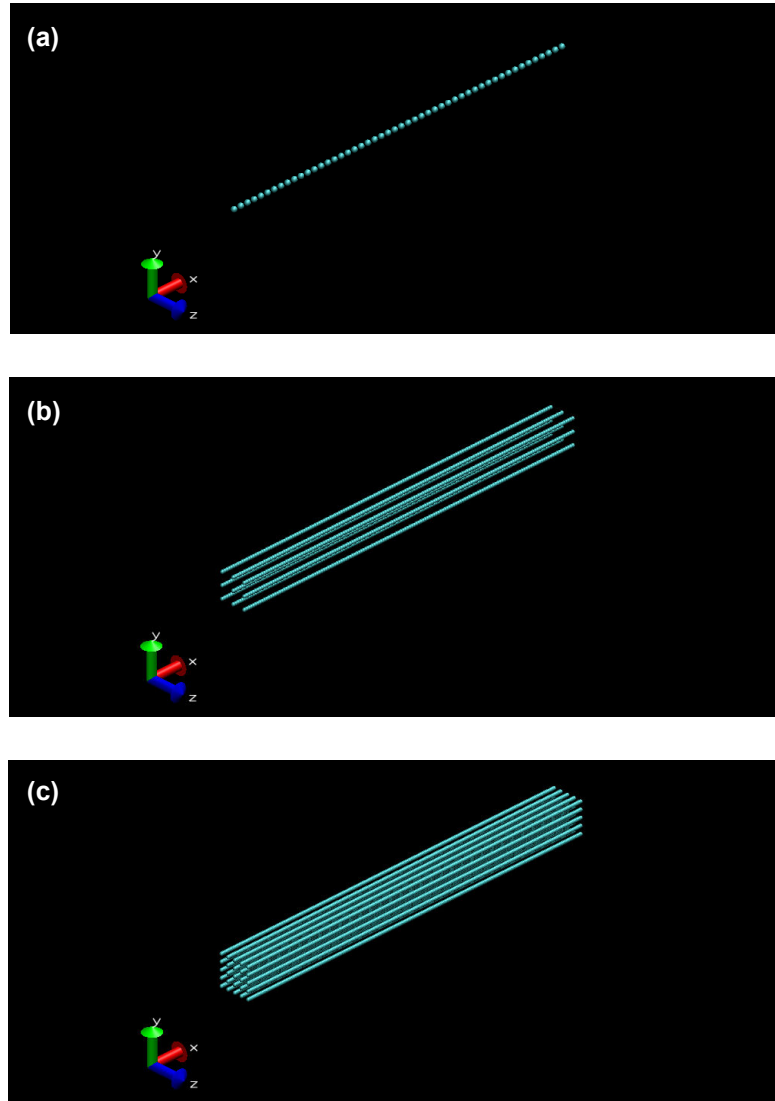


Figure 3.7 MPM models of a metal bar: (a) $1 \times 1 \times 1$ point per cell, (b) $3 \times 3 \times 3$ points per cell, (c) $5 \times 5 \times 5$ points per cell

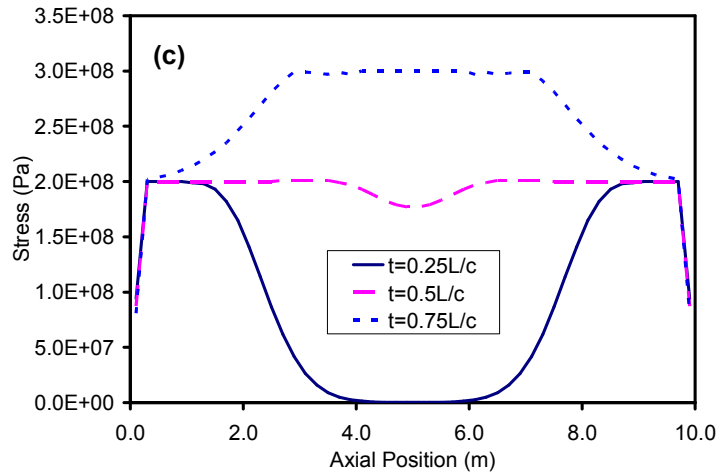
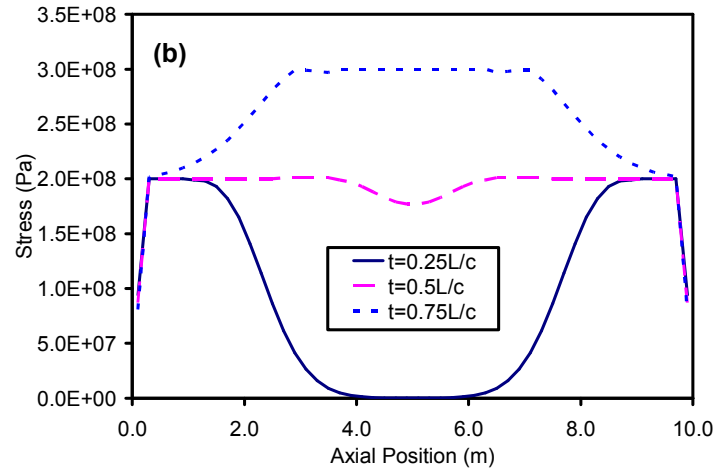
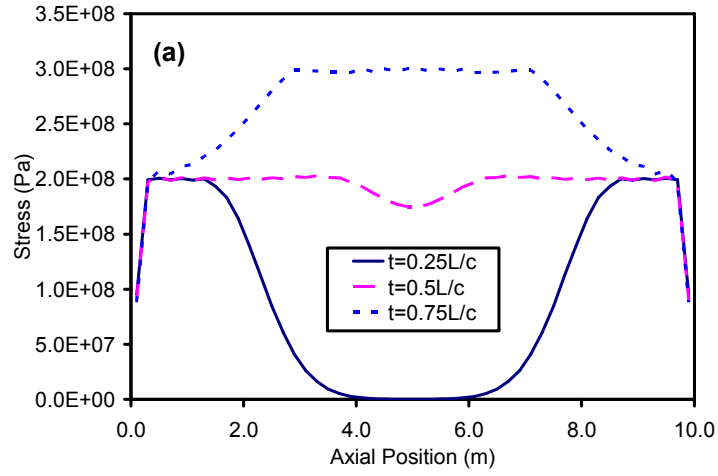


Figure 3.8 The equivalent stress profile along x-direction at different time: (a) $1 \times 1 \times 1$ point per cell, (b) $3 \times 3 \times 3$ points per cell, (c) $5 \times 5 \times 5$ points per cell

CHAPTER 4

THE MPM FOR FLUID-MEMBRANE INTERACTION

4.1 The MPM formulation for Three-dimensional Membranes

The mechanical models of biological cells are generally developed with a micro/nano-structural approach or a continuum way (Lim et al., 2006). The micro-scale cell model is used for the study of cytoskeletal mechanics at the molecular level (Boey et al., 1998; Stamenovic and Ingber, 2002; Coughlin and Stamenovic, 2003). Since the whole-cell deformation is of considerable interest in this study, the oocyte would be modeled at the continuum level. Through the examination of the oocyte deformation in the ICSI experiment for the mouse, it is noticed that the oocyte, behaving like a fluid, is able to deform continuously until the injection pipette pierces the zona pellucida. As a result, the mouse oocyte simulated here is modeled as one viscous fluid droplet surrounded by an isotropic membrane without molecular details, as sketched in Figure 4.1.

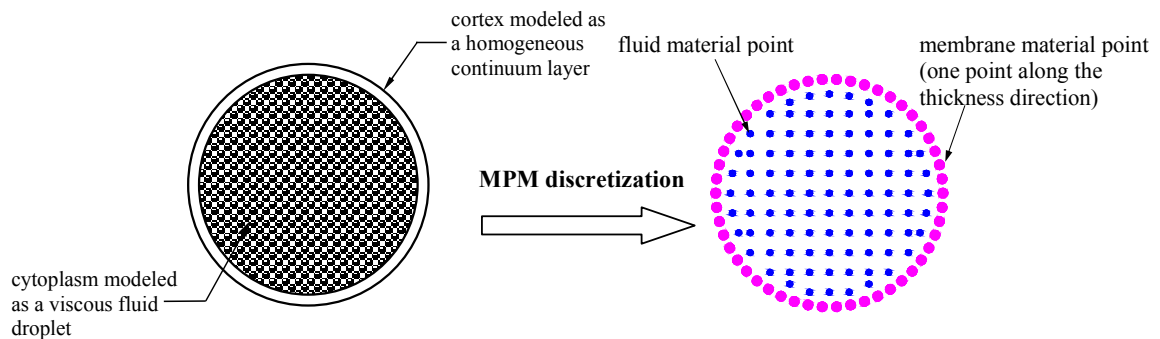


Figure 4.1 Viscous fluid droplet model of the oocyte

Continuum models of the cell membrane are broadly divided into two categories, i.e., pure-stretching model (Skalak et al., 1973) and pure-bending model (Waugh et al., 1992). The micropipette aspiration experiment has demonstrated that the bending modulus of the cell membrane is negligible as compared to its extensional rigidity (Evans and Skalak, 1980). The study conducted by Lardner and Pujara (1980) showed that the results based on the extensional modulus dominated model are consistent with the experimental data. The bending stiffness of the cell membrane seems important in the membrane tethers, spicules and undulation (Zeman et al., 1990; Waugh et al., 1992; Bozic et al., 1997; Iglic, 1997). Since the mouse zona pellucida is found to be flexible in the ICSI experiment, it is reasonable to take the pure-stretching model for the zona. Therefore, the membrane defined here is representative of a structure which only possesses the stretching stiffness in the plane tangent to the structure and has no rigidity in bending. Many existing structures could be approximated as the membrane, such as balloons, solar sails, space sunshields, and parachutes.

In the MPM, no connection exists between any two points separated by one or more grid cells. It is known that membranes have strains only in the local tangent plane while other strain components are negligible. Thus, to employ the MPM for simulating membrane structures, the original MPM algorithm must be modified to ensure the in-plane deformations of the membrane material points. Otherwise, unrealistic membrane rupture may occur due to the absence of the effective connection between neighboring membrane points through grid nodes. York II (1997) has formulated a two-dimensional MPM membrane model by adopting proper assumptions and applying the membrane constitutive model to the strains in the local normal-tangential coordinate system. Some

two-dimensional problems, such as the impact of a ball upon a net and the expansion of an airbag, have been favorably simulated with the proposed method. The MPM model for three-dimensional membranes can be developed by extending the key idea of the two-dimensional MPM membrane formulation to three dimensions. Before the presentation of the three-dimensional MPM membrane model, the two-dimensional MPM membrane formulation is first reviewed as below.

Figure 4.2(a) shows a membrane represented by material points in two dimensions, and its corresponding three-dimensional configuration is illustrated in Figure 4.2(b). The global Cartesian coordinate system is defined as the x - y - z and the x' - y' - z' is the local coordinate system at membrane point p with the x' - y' plane being the local tangential plane and the z' axis being the thickness direction. There is one layer of material points through the membrane thickness. At membrane point p , the normal stress along the z' -direction is set to be zero, and the normal strain in the y' -direction is assumed to be zero. In addition, it is assumed that there are no shearing strains in the x' - z' and x' - y' planes. Thus, strain components at the local coordinate system could be written as

$$\begin{cases} \varepsilon_{z'} = -\nu\varepsilon_{x'}/(1-\nu) \\ \varepsilon_{y'} = 0, \quad \varepsilon_{z'x'} = 0 \end{cases} \quad (4.1)$$

where ν is the Poisson's ratio of the membrane. For elastic membranes, the stresses can be calculated based on the following equations

$$\begin{Bmatrix} \sigma_{x'} \\ \sigma_{z'} \\ \sigma_{y'} \\ \sigma_{z'x'} \end{Bmatrix} = \frac{E}{(1+\nu)(1-2\nu)} \begin{bmatrix} 1-\nu & \nu & \nu & 0 \\ \nu & 1-\nu & \nu & 0 \\ \nu & \nu & 1-\nu & 0 \\ 0 & 0 & 0 & 1-2\nu \end{bmatrix} \begin{Bmatrix} \varepsilon_{x'} \\ -\nu\varepsilon_{x'}/(1-\nu) \\ 0 \\ 0 \end{Bmatrix} = \begin{Bmatrix} E\varepsilon_{x'}/(1-\nu^2) \\ 0 \\ \nu E\varepsilon_{x'}/(1-\nu^2) \\ 0 \end{Bmatrix} \quad (4.2)$$

where E is the Young's modulus of the membrane. In the MPM, the equations of motion are solved on the Eulerian grid mesh constructed in the x - y - z global coordinate system.

The strain rate at point p is calculated by

$$\dot{\boldsymbol{\varepsilon}}_p = \frac{1}{2} \left[\nabla \mathbf{v}_p + (\nabla \mathbf{v}_p)^T \right] \quad (4.3)$$

At time step $k+1$, the total strains at point p are

$$\boldsymbol{\varepsilon}_p^{k+1} = \boldsymbol{\varepsilon}_p^k + \dot{\boldsymbol{\varepsilon}}_p^{k+1} \Delta t \quad (4.4)$$

in which the superscript represents the time level and Δt is the time step. The total strains $\boldsymbol{\varepsilon}_p^{k+1}$ should be transformed to the local coordinate system for the calculation of stresses consistent with the membrane orientation. At point p showed in Figure 4.2(a), its normal strain along the x' -direction is calculated by

$$\varepsilon_{x'}^{k+1} = \varepsilon_x^{k+1} (\cos \theta)^2 + \varepsilon_z^{k+1} (\sin \theta)^2 + 2\varepsilon_{xz}^{k+1} \sin \theta \cos \theta \quad (4.5)$$

Then, stresses in the local normal-tangential coordinate system could be determined by Equations (4.1) and (4.2). After the local stresses are found, they must be transformed back to the global coordinate system for the computation of internal forces at grid nodes.

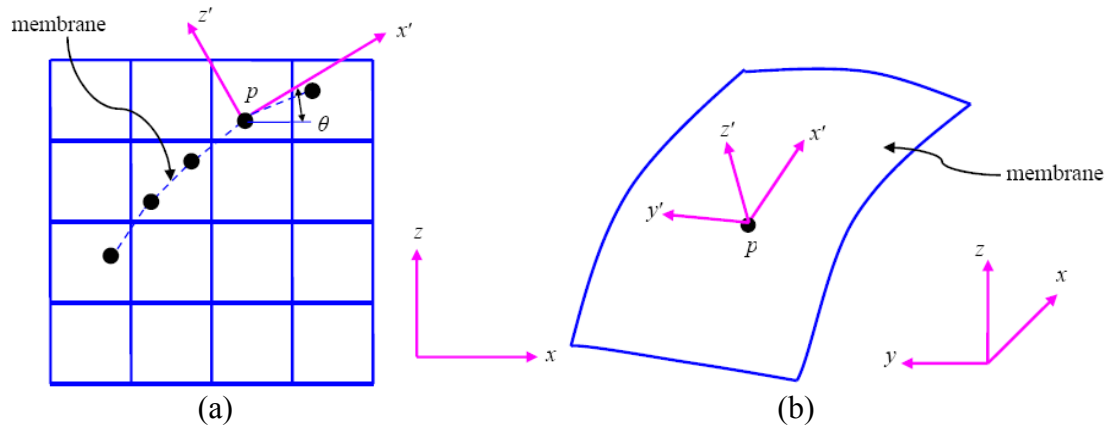


Figure 4.2 A two-dimensional membrane represented by material points: (a) material point representation in two dimensions, (b) three-dimensional view of the membrane

To implement the MPM membrane formulation, two important issues, the orientation of the tangential vector at material points and the wrinkle of the membrane, should be addressed. In two dimensions, the orientation of the tangential direction at material points can be simply found by the connectivity of material points. As illustrated in Figure 4.3, the angle between axes x and x' , θ_p , is

$$\theta_p = \frac{\theta_{p,p+1} + \theta_{p-1,p}}{2} \quad (4.6)$$

Angles of $\theta_{p-1,p}$ and $\theta_{p,p+1}$ could be determined from the coordinates of points $p-1$, p and $p+1$. Since the membrane can sustain tension only, the wrinkle may occur when tangent strains become negative. York II (1997) proposed a one-way constitutive equation to handle the membrane wrinkle, as shown in Figure 4.4. The basic idea is to assume the Young's modulus to be zero for negative tangent strains. As can be seen, the one-way constitutive equation provides a simple and convenient way to deal with the membrane wrinkle without performing the buckling or bending analysis of the membrane.

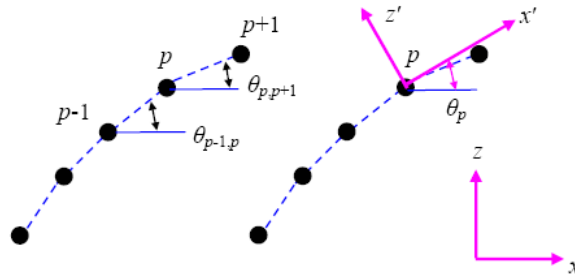


Figure 4.3 Determination of tangential angle with the connectivity of material points

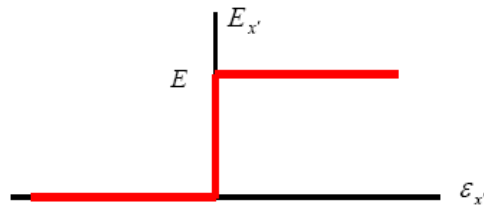


Figure 4.4 One-way constitutive model for the membrane wrinkle

In general, the way to develop the MPM formulation for three-dimensional membranes follows that for the two-dimensional MPM membrane model. As mentioned earlier, the membrane has stresses in the tangential plane only. Hence, the plane stress assumption is applied in the local tangential $x'-y'$ plane, namely,

$$\varepsilon_{z'} = -\frac{\nu(\varepsilon_{x'} + \varepsilon_{y'})}{1-\nu} \quad (4.7)$$

$$\begin{Bmatrix} \sigma_{x'} \\ \sigma_{y'} \\ \sigma_{z'} \\ \sigma_{x'y'} \end{Bmatrix} = \frac{E}{(1+\nu)(1-2\nu)} \begin{bmatrix} 1-\nu & \nu & \nu & 0 \\ \nu & 1-\nu & \nu & 0 \\ \nu & \nu & 1-\nu & 0 \\ 0 & 0 & 0 & 1-2\nu \end{bmatrix} \begin{Bmatrix} \varepsilon_{x'} \\ \varepsilon_{y'} \\ -\nu(\varepsilon_{x'} + \varepsilon_{y'})/(1-\nu) \\ \varepsilon_{x'y'} \end{Bmatrix} \quad (4.8)$$

As can be seen, $\varepsilon_{y'}$ and $\varepsilon_{x'y'}$ are no longer nullified in the three-dimensional MPM membrane formulation. To evaluate the stresses at membrane points, the total strains in the x - y - z coordinate system are required to be transformed to the local normal-tangential coordinate system. According to the tensor theory, the direction cosine tensor for the transformation of coordinates in three dimensions can be expressed as

$$\mathbf{Q} = \begin{bmatrix} Q_{xx'} & Q_{xy'} & Q_{xz'} \\ Q_{yx'} & Q_{yy'} & Q_{yz'} \\ Q_{zx'} & Q_{zy'} & Q_{zz'} \end{bmatrix} \quad (4.9)$$

with Q_{ij} ($i=x, y, z$ and $j=x', y', z'$) being the direction cosine between the global basis vector e_i and local basis vector e'_j . With the updated total strain in the global coordinate system, ε_p^{k+1} , the strains in the local $x'-y'-z'$ coordinate system can be found by the following tensor transformation formulation

$$\varepsilon'_p = \mathbf{Q}^T \varepsilon_p^{k+1} \mathbf{Q} \quad (4.10)$$

where $\boldsymbol{\varepsilon}'_p$ is the local strains at point p . Once the stresses in the local coordinate system are computed with the local strains and appropriate constitutive model, they should be transformed back to the x - y - z coordinate system by

$$\boldsymbol{\sigma}_p^{k+1} = \boldsymbol{Q} \boldsymbol{\sigma}'_p \boldsymbol{Q}^T \quad (4.11)$$

where $\boldsymbol{\sigma}_p^{k+1}$ and $\boldsymbol{\sigma}'_p$ are the symmetric stress tensor in the global and local coordinate systems at point p , respectively. It should be noted that the local stresses rather than the local strains are rotated back to the global coordinate system. As can be seen from Equations (4.10) and (4.11), the computation of the stresses at membrane points is straightforward with the determined \boldsymbol{Q} . The orientation of the local x' - y' - z' coordinate system is proposed to be determined by two steps: (1) determine the vector normal to the membrane surface, \boldsymbol{z}' , (2) find vectors \boldsymbol{x}' and \boldsymbol{y}' .

In addition to the point connectivity method, many other approaches have been proposed to determine the material point normal, such as simple color function approach, interpolation method, mass matrix approach and point-set method (York II, 1997; Torres and Brackbill, 2000). These methods, however, are not effective for complex membrane shapes, and need a large number of points to obtain the satisfied point normal. Moreover, the numerical implementation of these methods is much more complicated than that of the connectivity method. In fact, the connectivity method is quite simple and convenient except the disadvantage of the additional storage space for the connectivity data. Nowadays, the computer hardware is so powerful that the storage space requirement is no longer an issue, even for the three-dimensional case.

The original algorithm to set material points is cell-based. Material points are regularly distributed in the grid cells and each point is assigned a fraction of the mass of the associated cell. Since membrane points have no ordered relationship with grid cells, the discretization of the spherical membrane is performed in a different way to construct the connectivity information for membrane points. The membrane surface is firstly approximated by a collection of triangles, and then the membrane material points are defined on the vertices. If s is the surface area of the membrane, ρ^m is the mass per unit area of the membrane and N^P is the total number of vertices, the mass of each material point is simply set to be $s\rho^m/N^P$. As the membrane deforms, the unrealistic membrane break may happen due to the separation of membrane points by one or more cells if the membrane is represented by insufficient points. However, more points require more computation time and hardware. Thus, the triangulation of the membrane surface is usually tried a few times until a balance between the number of membrane material points and computation cost is reached. In this dissertation, the GNU Triangulated Surface Library (GTS, <http://gts.sourceforge.net>) is used for triangulating the spherical surface, as shown in Figure 4.5.

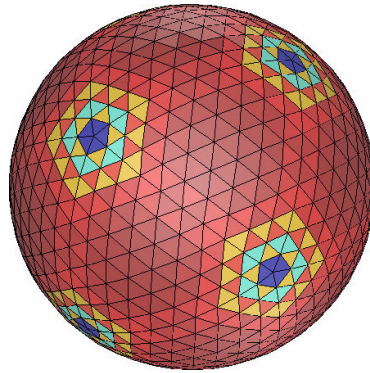


Figure 4.5 A sphere triangulated by GTS (<http://gts.sourceforge.net/gallery.html>)

Because of its initialization on the triangle vertex, each membrane material point would be shared by several triangles. The normal vector of each triangle could be easily found with the coordinates of its three vertices. As illustrated in Figure 4.6, the point normal, thus, is simply taken as the average of unit vectors normal to the triangles to which the membrane point belongs, i.e.,

$$\mathbf{n}_p = \sum_{i=1}^{N_{Tri}} \mathbf{n}_i / N_{Tri} \quad (4.12)$$

where \mathbf{n}_p is the point normal at point p , \mathbf{n}_i is the unit vector normal to triangle i , and N_{Tri} is the total number of triangles surrounding material point p . Conventionally, the normal to a triangle is determined by the right-hand rule and the outward-pointing normal is used for closed surfaces.

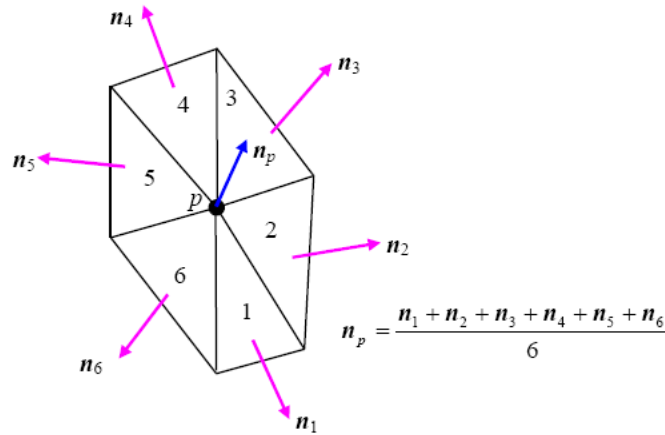


Figure 4.6 Calculation of the point normal

At a given membrane material point, \mathbf{z}'_{k+1} and \mathbf{z}'_k are used to denote the unit point normals at time levels $k+1$ and k , respectively. In three dimensions, the relation between \mathbf{z}'_{k+1} and \mathbf{z}'_k could be expressed as

$$\mathbf{z}'_{k+1} = \mathbf{S} \cdot \mathbf{z}'_k \quad (4.13)$$

where \mathbf{S} is a 3×3 orthogonal rotation matrix, namely, $\mathbf{S}^{-1} = \mathbf{S}^T$. Because of the use of the Cartesian coordinate system, vectors \mathbf{x}'_{k+1} and \mathbf{y}'_{k+1} can also be written as

$$\mathbf{x}'_{k+1} = \mathbf{S} \cdot \mathbf{x}'_k \quad (4.14)$$

$$\mathbf{y}'_{k+1} = \mathbf{S} \cdot \mathbf{y}'_k \quad (4.15)$$

The calculation of the direction cosine tensor \mathbf{Q} , hence, becomes the derivation of the orthogonal matrix, \mathbf{S} . Let the cross product of \mathbf{z}'_k and \mathbf{z}'_{k+1} be denoted by $\overline{\mathbf{w}}$, and $\hat{\mathbf{w}}$ be the normalized vector of $\overline{\mathbf{w}}$, i.e.,

$$\overline{\mathbf{w}} = \mathbf{z}'_k \times \mathbf{z}'_{k+1} \quad (4.16)$$

$$\hat{\mathbf{w}} = \overline{\mathbf{w}} / |\overline{\mathbf{w}}| \quad (4.17)$$

Furthermore, one vector, \mathbf{z}''_{k+1} , is introduced and formulated as

$$\mathbf{z}''_{k+1} = \mathbf{z}'_{k+1} - (\mathbf{z}'_k \cdot \mathbf{z}'_{k+1}) \mathbf{z}'_k \quad (4.18)$$

The unit vector of \mathbf{z}'' is $\hat{\mathbf{z}}'' = \mathbf{z}'' / |\mathbf{z}''|$. Then, the orthogonal matrix \mathbf{S} can be computed as

$$\mathbf{S} = (\hat{\mathbf{w}} \otimes \hat{\mathbf{w}}) + \mathbf{R}(\mathbf{I}_3 - \hat{\mathbf{w}} \otimes \hat{\mathbf{w}}) \quad (4.19)$$

where \mathbf{I}_3 is an identity matrix of order 3, and \mathbf{R} is given by

$$\mathbf{R} = (\mathbf{z}'_k \cdot \mathbf{z}'_{k+1}) (\mathbf{z} \otimes \mathbf{z} + \hat{\mathbf{z}}'' \otimes \hat{\mathbf{z}}'') + (\mathbf{z}''_{k+1} \otimes \mathbf{z}'_k - \mathbf{z}'_k \otimes \mathbf{z}''_{k+1}) \quad (4.20)$$

The substitution of (4.20) into (4.19) yields

$$\mathbf{S} = (\hat{\mathbf{w}} \otimes \hat{\mathbf{w}}) + (\mathbf{z}'_k \cdot \mathbf{z}'_{k+1}) (\mathbf{I} - \hat{\mathbf{w}} \otimes \hat{\mathbf{w}}) + (\mathbf{z}'_{k+1} \otimes \mathbf{z}'_k - \mathbf{z}'_k \otimes \mathbf{z}'_{k+1}) \quad (4.21)$$

Equation (4.21) is only valid for $|\overline{\mathbf{w}}| > 0$. When \mathbf{z}'_{k+1} coincides with \mathbf{z}'_k , $|\overline{\mathbf{w}}| = 0$. Then, matrix \mathbf{S} becomes a unit matrix of order 3.

To simulate the membrane wrinkle, the one-way constitutive equation is applied to principal strains. In two dimensions, $\varepsilon_{x'}$ is already a principal strain because all shearing strains are assumed to be zero. However, for three-dimensional MPM membranes, the shearing strains in the local tangent plane are not zero. The principal strains in the local tangent plane, hence, are required to be found before the application of the one-way constitutive equation. Figure 4.7 shows the rotation of strains in the local tangent plane. Axes of x_1' and y_1' are the principal directions, and θ_p is calculated by

$$\tan 2\theta_p = \frac{2\varepsilon_{x'y'}}{\varepsilon_{x'} - \varepsilon_{y'}} \quad (4.22)$$

The principal strains are given by

$$\varepsilon_{1,2} = \frac{\varepsilon_{x'} + \varepsilon_{y'}}{2} \pm \sqrt{\left(\frac{\varepsilon_{x'} - \varepsilon_{y'}}{2}\right)^2 + \varepsilon_{x'y'}^2} \quad (4.23)$$

To determine the angles to the principal directions, one value of θ_p is substituted into the following equation

$$\varepsilon_{x'_1} = \frac{\varepsilon_{x'} + \varepsilon_{y'}}{2} + \frac{\varepsilon_{x'} - \varepsilon_{y'}}{2} \cos 2\theta_p + \varepsilon_{x'y'} \sin 2\theta_p \quad (4.24)$$

The comparison of $\varepsilon_{x'_1}$ with ε_1 and ε_2 can show which value of θ_p is associated with each principal strain. The one-way constitutive model is then applied to the principal strains to obtain the principal stresses, which are rotated back to the x' - y' coordinate system by

$$\sigma_{x'} = \frac{\sigma_1 + \sigma_2}{2} + \frac{\sigma_1 - \sigma_2}{2} \cos(-2\theta_{p1}) \quad (4.25)$$

$$\sigma_{y'} = \sigma_1 + \sigma_2 - \sigma_{x'} \quad (4.26)$$

$$\tau_{x'y'} = -\frac{\sigma_1 - \sigma_2}{2} \sin(-2\theta_{p1}) \quad (4.27)$$

where σ_1 and σ_2 are principal stresses, and θ_{p1} is the angle corresponding to principal stress σ_1 .

With the procedure presented above, the three-dimensional MPM membrane model can be easily implemented by modifying the existing three-dimensional MPM code. If the material point is a membrane point, its global strains are rotated to the local coordinate system. Then, the plane stress assumption and one-way constitutive equation are applied. With an appropriate constitutive model, the local stresses at the membrane point are computed and transformed back to the global coordinate system for the evaluation of the internal forces at grid nodes. It should be noted that the elastic membrane is assumed to demonstrate the employment of the plane stress assumption and one-way constitutive equation in the MPM membrane model. When the membrane is inelastic, it is proposed that the stresses at membrane points be computed by invoking the strain increments and the membrane wrinkle be simulated by nullifying the negative principal stresses in the local tangent plane.

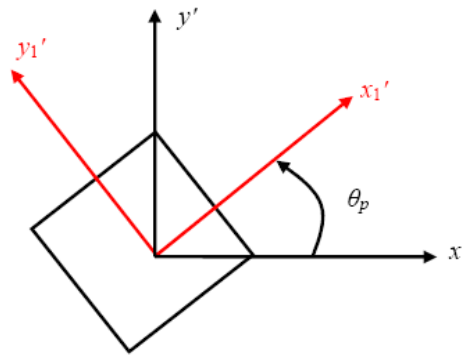


Figure 4.7 Computation of the principal strains in the local tangent plane

4.2 The MPM formulation for Fluids

The discretization procedure and numerical scheme in the standard MPM algorithm should hold for solids as well as fluids because no constitutive equations are invoked in the development of MPM momentum equations. The key difference between fluid and solid material points is the various constitutive relations they respectively follow. For fluid material points, the relation between the stresses and rate of strains is given by

$$\sigma_{ij} = 2\mu\dot{\epsilon}_{ij} + \lambda\dot{\epsilon}_{kk}\delta_{ij} - P\delta_{ij} \quad (4.28)$$

where λ is bulk viscosity, μ is shear viscosity and P is the fluid pressure. For most of fluids, Stokes condition is valid, i.e., $\lambda = -2\mu/3$. Thus, the spherical component of stress, $\sigma_{kk}/3$, is equal to the pressure P . As discussed in Chapter 3, the strain rate of the material point is computed from the grid node velocities and the gradient of the shape functions evaluated at the updated material point position, namely,

$$\dot{\epsilon}_p^k = \frac{1}{2} \sum_{i=1}^{N_n} \left[\mathbf{G}_{ip}^k \tilde{\mathbf{v}}_i^k + \left(\mathbf{G}_{ip}^k \tilde{\mathbf{v}}_i^k \right)^T \right] \quad (4.29)$$

where subscript p denotes point p and superscript k represents the evaluation at time t^k .

To find the stresses at fluid material points with Equation (4.28), an equation of state (EOS) is required for pressure P ,

$$I = I(P, \rho) \quad (4.30)$$

where I is specific internal energy. The EOS of the ideal gas is formulated as

$$P = (\gamma - 1)\rho I \quad (4.31)$$

where γ is the ratio of specific heats and a constant of 1.4. Based on the mass conservation, the density at material points can be updated by the following equation

$$\rho^{k+1} = \frac{\rho^k}{1 + \Delta t (\nabla \cdot \mathbf{v}_p)} \quad (4.32)$$

The EOS is dependent on the internal energy as well as density. The energy equation, thus, is considered at each material point. If the thermal effect is negligible, the conservation of energy gives that the change of internal energy is equal to the rate of mechanical work done by stresses on the system, namely,

$$\rho \frac{dI}{dt} = \boldsymbol{\sigma} : \dot{\boldsymbol{\epsilon}} \quad (4.33)$$

With Equations (3.3) and (4.28), the right side of Equation (4.33) is expressed as

$$\begin{aligned} \boldsymbol{\sigma} : \dot{\boldsymbol{\epsilon}} &= \sigma_x \dot{\epsilon}_x + \sigma_y \dot{\epsilon}_y + \sigma_z \dot{\epsilon}_z + 2\sigma_{xy} \dot{\epsilon}_{xy} + 2\sigma_{yz} \dot{\epsilon}_{yz} + 2\sigma_{zx} \dot{\epsilon}_{zx} \\ &= -P(\nabla \cdot \mathbf{v}_p) + \mu \left[\left(\frac{\partial u_y}{\partial x} + \frac{\partial u_x}{\partial y} \right)^2 + \left(\frac{\partial u_z}{\partial y} + \frac{\partial u_y}{\partial z} \right)^2 + \left(\frac{\partial u_x}{\partial z} + \frac{\partial u_z}{\partial x} \right)^2 \right] \\ &\quad + 2\mu \left[\left(\frac{\partial u_x}{\partial x} \right)^2 + \left(\frac{\partial u_y}{\partial y} \right)^2 + \left(\frac{\partial u_z}{\partial z} \right)^2 \right] - \frac{2}{3} \mu (\nabla \cdot \mathbf{v}_p)^2 \end{aligned} \quad (4.34)$$

where u_x , u_y and u_z are the velocity components of material points in the x -, y - and z -directions, respectively. Once the gradient terms of the point velocity are computed, the internal energy of fluid is updated by

$$I^{k+1} = I^k + \frac{\Delta t}{\rho^k} \boldsymbol{\sigma}^{k+1} : \dot{\boldsymbol{\epsilon}}^{k+1} \quad (4.35)$$

It can be found from Equations (4.30) and (4.33) that Equation (4.28) is nonlinear because its two sides contain the stress term. Thus, an iteration procedure must be employed to obtain convergent internal energy and pressure. The basic iteration steps are described as follows:

(1) At time level $k+1$, the internal energy of fluid points is initially set as

$$I^{k+1} = I^k + \frac{\Delta t}{\rho^k} \boldsymbol{\sigma}^k : \dot{\boldsymbol{\epsilon}}^{k+1} \quad (4.36)$$

(2) The density of fluid points are calculated by the equation of continuity,

$$\rho^{k+1} = \frac{\rho^k}{1 + \Delta t (\nabla \cdot \mathbf{v}_p^{k+1})} \quad (4.37)$$

(3) The pressure of fluid points is obtained by solving the equation of state,

$$I^{k+1} = I(P^{k+1}, \rho^{k+1}) \quad (4.38)$$

(4) The stress tensor of fluid points is written as

$$\sigma_{ij}^{k+1} = 2\mu \dot{\epsilon}_{ij}^{k+1} + \lambda \dot{\epsilon}_{kk}^{k+1} \delta_{ij} - P^{k+1} \delta_{ij} \quad (4.39)$$

(5) The internal energy of material points is updated by

$$I^{k+1} = I^k + \frac{\Delta t}{\rho^k} \boldsymbol{\sigma}^{k+1} : \dot{\boldsymbol{\epsilon}}^{k+1} \quad (4.40)$$

for the first iteration substep or

$$I^{k+1} = I^k + \frac{\Delta t}{\rho^k} \left(\frac{\boldsymbol{\sigma}^{k+1,pr} + \boldsymbol{\sigma}^{k+1}}{2} \right) : \dot{\boldsymbol{\epsilon}}^{k+1} \quad (4.41)$$

for the remaining substeps in the iterative loop, with the superscript *pr* denotes the result obtained in the previous iteration substep.

(6) Steps (3)-(5) are repeated until the internal energy and pressure are convergent for a given error tolerance.

The use of artificial viscosity in fluid dynamics simulations has proven to be able to smooth the numerical oscillation at the shock front and yield more accurate results. The concept of artificial viscosity is firstly introduced by Neumann and Richtmyer (1950).

They proposed artificial viscosity for the calculation of the propagation of one-dimensional shocks in inviscid fluids, q_1 ,

$$\begin{cases} q_1 = c^2 \rho (\Delta x)^2 \left(\frac{\partial \dot{x}}{\partial x} \right)^2 & \frac{\partial \dot{x}}{\partial x} < 0 \\ q_1 = 0 & \frac{\partial \dot{x}}{\partial x} \geq 0 \end{cases} \quad (4.42)$$

where c is a constant ≈ 2 , ρ is the fluid density, Δx is the grid spacing and x is the motion direction. The physics of the artificial viscosity is to spread the shock over the minimum grid spacing while damping the oscillations behind the shock (Wilkins, 1980).

Landshoff (1955) introduced the artificial viscosity linear in the velocity gradient, q_2 ,

$$\begin{cases} q_2 = c_L \rho (\Delta x) a \left| \frac{\partial \dot{x}}{\partial x} \right| & \frac{\partial \dot{x}}{\partial x} < 0 \\ q_2 = 0 & \frac{\partial \dot{x}}{\partial x} \geq 0 \end{cases} \quad (4.43)$$

in which a is the local sound speed and $a = \sqrt{\gamma P / \rho}$ for gas. It is found that the linear viscosity q_2 diffuses the shock front over an increasing distance as the shock propagates.

Landshoff (1955) suggested the employment of a linear combination of q_1 and q_2 ,

$$q = q_1 + q_2 \quad (4.44)$$

With the use of Hugoniot relations, Kuropatenko (1967) obtained a viscosity term for fluid dynamics in one dimension and time. Wilkins (1980) examined the perfect gas with the Kuropatenko method, and found that the quadratic viscosity is obtained for high shocks and the linear viscosity for low shocks.

The artificial viscosity employed in the MPM, q , is added to the pressure of fluid material points and expressed as

$$\begin{cases} q = \rho L_c (c_0 L_c \dot{\epsilon}_{kk}^2 - c_1 a \dot{\epsilon}_{kk}) & \dot{\epsilon}_{kk} < 0 \\ q = 0 & \dot{\epsilon}_{kk} \geq 0 \end{cases} \quad (4.45)$$

where c_0 and c_1 are constants and L_c is the characteristic length. In the three-dimensional MPM, the characteristic length L_c is calculated as

$$L_c = \sqrt[3]{V_{\text{cell}}} \quad (4.46)$$

where V_{cell} is the volume of the grid cell. Usually, the grid cell in the three-dimensional MPM is cubic. Thus, the characteristic length is identical to the side length of the background mesh cell. The artificial viscosity given in Equation (4.45) is also used in LS-DYNA (Hallquist, 1998), in which c_0 and c_1 default to 1.5 and 0.6, respectively. In general, the values of c_0 and c_1 should be determined through numerical tests. The MPM algorithm for fluids is summarized as follows:

- (1) Construct the background grid, and initialize material point locations, velocities, masses,
- (2) Map momentum, mass, and stresses of each material point to the grid nodes,
- (3) Apply the boundary conditions to grid nodes, and compute the nodal forces,
- (4) Update the momenta at grid nodes,
- (5) Map nodal velocities to points, and update the point locations,
- (6) Map nodal accelerations to points and compute the point velocities to update the momenta at material points,
- (7) Map the updated point momenta to nodes and find the updated nodal velocities,
- (8) Apply essential boundary conditions to nodes and compute the point strain increment with the nodal velocities given in step (7),

- (9) Compute the stresses and the internal energy of fluid points with the proposed iteration procedure,
- (10) Identify which cell each point belongs to, update the natural coordinates of the material point and time level,
- (11) Go back to step (2) unless the required computation time is reached.

4.3 Simulation of Fluid-Membrane Interaction with the MPM

In the MPM, the stresses at membrane and fluid material points are transformed into nodal forces, and the accelerations are imposed on the material points through the interpolation of the nodal accelerations. The accumulation of nodal forces, \mathbf{f}_i , from the stresses at membrane and fluid material points, $\boldsymbol{\sigma}_m$ and $\boldsymbol{\sigma}_f$, is illustrated in Figure 4.8, in which M_m and M_f are the masses of the membrane and fluid points, respectively. Therefore, the pressure from the fluid points is not directly applied to the membrane points. Instead, the interaction between the fluid and the membrane is indirectly coupled via the Eulerian grid nodes without any consideration of the fluid-membrane interface. As a result, there is no need for the MPM to identify the fluid-membrane interface and to apply the correct boundary conditions as compared with mesh-based methods. In other words, the MPM is able to handle the fluid-membrane interaction automatically without requiring additional algorithms.

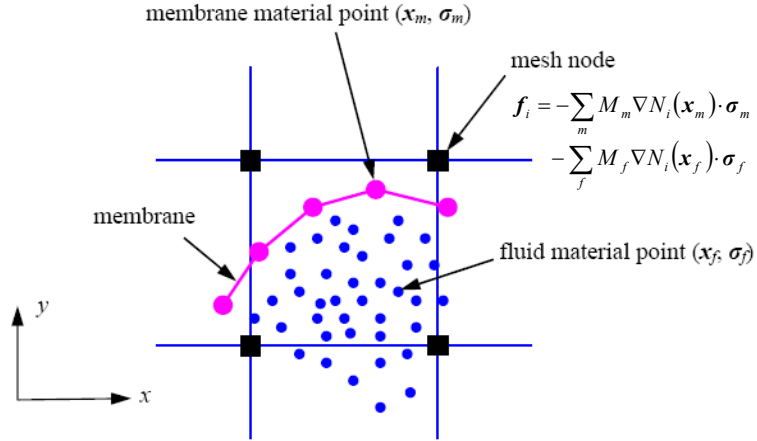


Figure 4.8 Illustration of the fluid-membrane interaction in the two-dimensional MPM

4.4 Demonstrations

4.4.1 One-dimensional shock tube

The simulation of one dimensional shock propagation in the fluid is an ideal example to test the MPM formulation for fluids because analytical solutions are available for this problem. As shown in Figure 4.9, a shock tube is divided into two halves by a diaphragm. Initially, the left region is full of ideal gas with high pressure p_L and density ρ_L , and the right region contains ideal gas with low density ρ_R and pressure p_R . The diaphragm is suddenly broken, and then the shock wave due to the pressure discontinuity propagates to the right.

The length of the tube, l , is 1 m and the initial velocities for the air in both regions is zero. Other initial conditions are $\rho_L = 1 \text{ kg/m}^3$, $p_L = 1 \text{ Pa}$, $\rho_R = 0.125 \text{ kg/m}^3$ and $p_R = 0.001 \text{ Pa}$. The ideal gas EOS is applied to the gases in both regions. This one-dimensional problem is solved with the three-dimensional MPM. The x -axis is chosen to

be the wave propagation direction. The nodal velocities along the other two directions, i.e., the y - and z -directions, are nullified. The background mesh is composed of 800 cubic cells with a side length of 0.00125 m. The initialization of material points in each cell is demonstrated in Figure 4.10. Thus, each cell has 25 points and there are 20000 points in total. The time step is 2.0×10^{-5} s and the artificial viscosity defined in Equation (4.45) is applied with $c_0=2.0$ and $c_1=1.0$.

Figure 4.11 gives the profiles of pressure, density, velocity and internal energy along the wave propagation direction at time $t=0.143$ s without using the artificial viscosity, and the corresponding profiles with the use of the artificial viscosity are presented in Figure 4.12. Figures 4.11 and 4.12 are both plotted according to the averages of material points initially located in each mesh cell. From Figure 4.11, it can be found that the pressure and density at the shock front are respectively up to 135 Pa and 578 kg/m^3 . However, the corresponding analytical solutions are 0.211 Pa and 0.73 kg/m^3 , respectively. The large oscillation is also observed in the profiles of the velocity and the internal energy. The examination of the results in Figure 4.12 shows that the artificial viscosity is able to effectively smooth the oscillation and the MPM results favorably agree with the analytical solutions. However, the noticeable oscillation is still found at the material discontinuity. Figures 4.13 and 4.14 present the MPM solutions with the artificial viscosity based on the averages of material points initialized in every two and four consecutive mesh cells, respectively. It can be seen that the oscillation at the material discontinuity becomes smaller as more material points are used to calculate the averages.

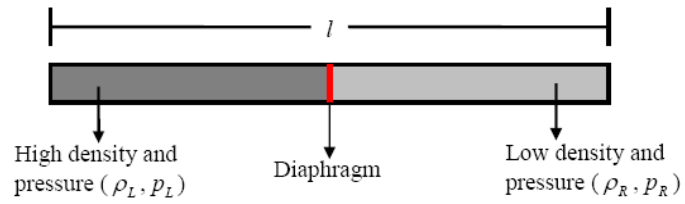


Figure 4.9 One-dimensional shock tube problem

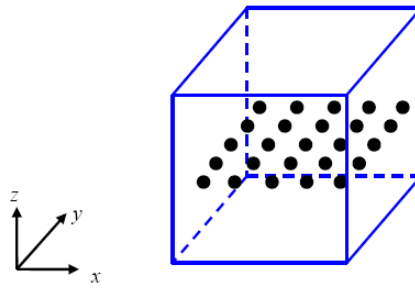
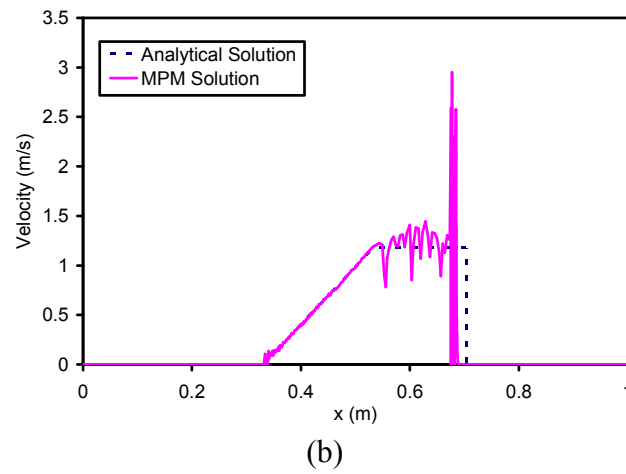
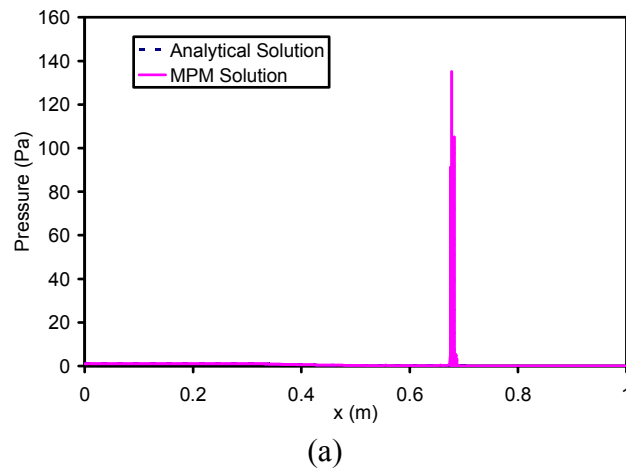


Figure 4.10 Initialization of points in one cell



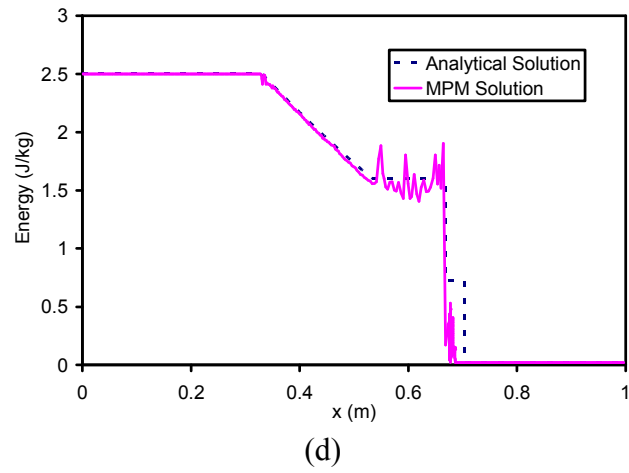
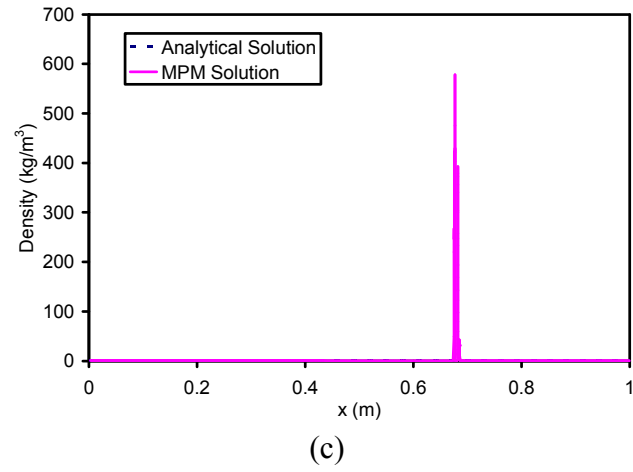
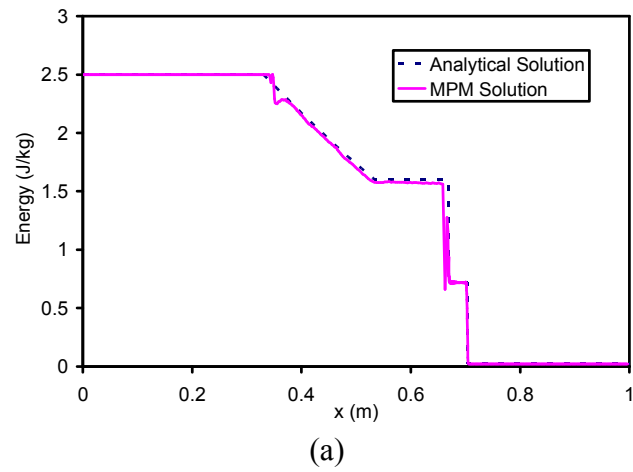


Figure 4.11 MPM solutions with no artificial viscosity (averages of material points initialized in one cell)



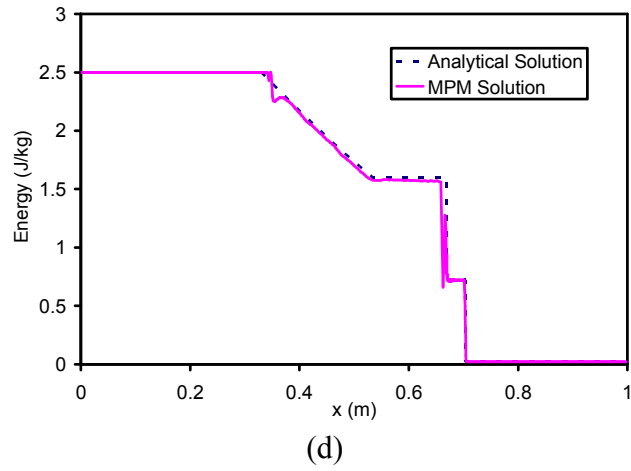
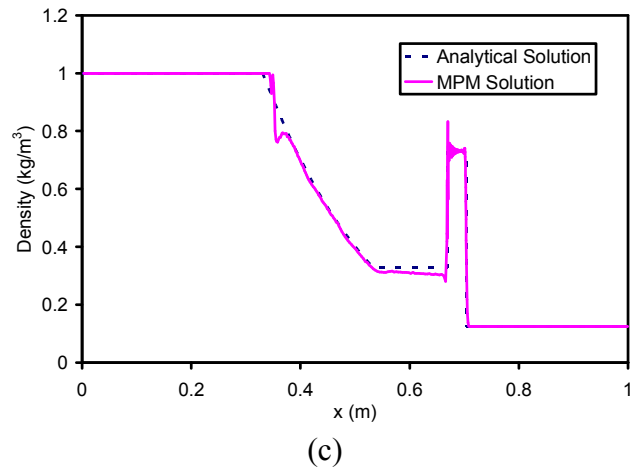
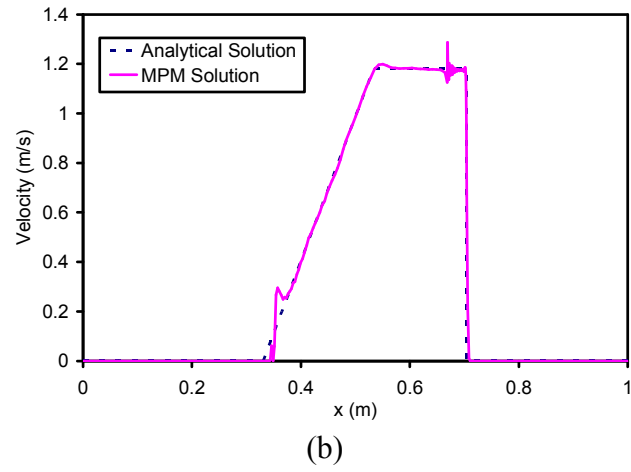
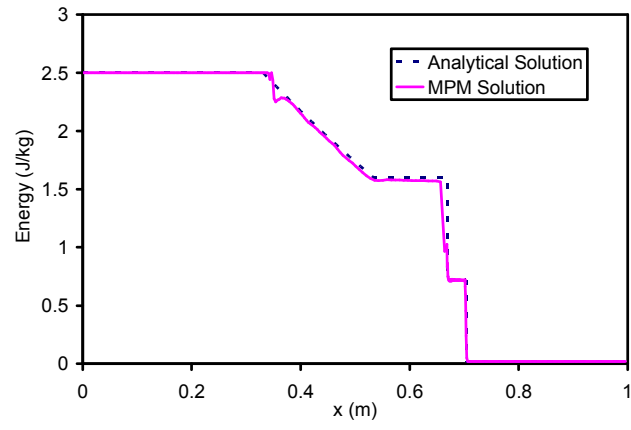
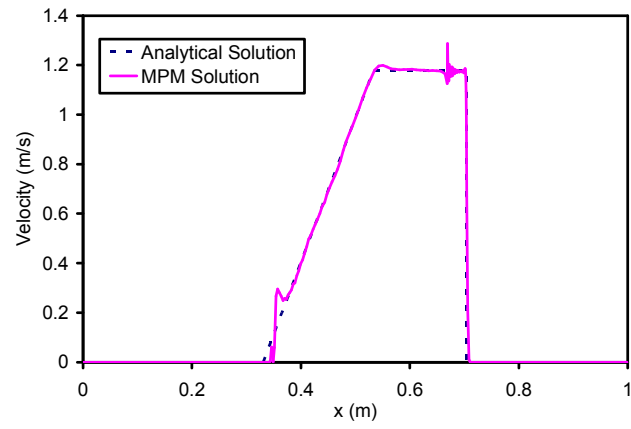


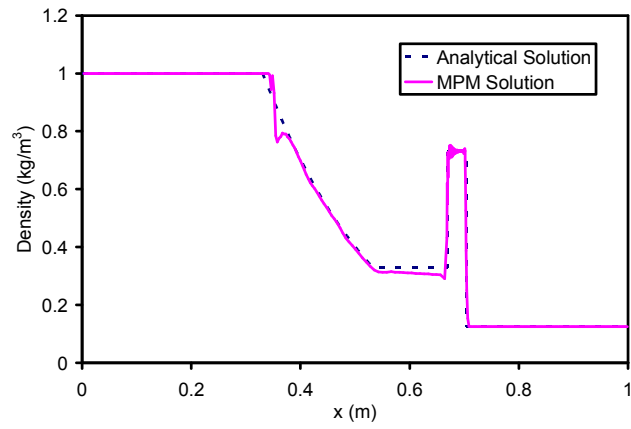
Figure 4.12 MPM solutions with artificial viscosity (averages of material points initialized in one cell)



(a)



(b)



(c)

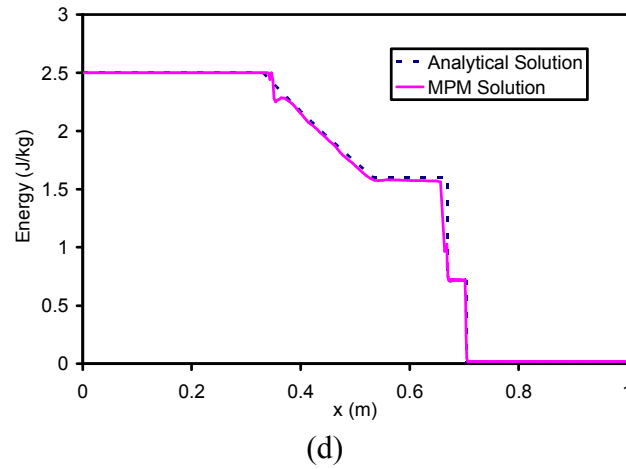
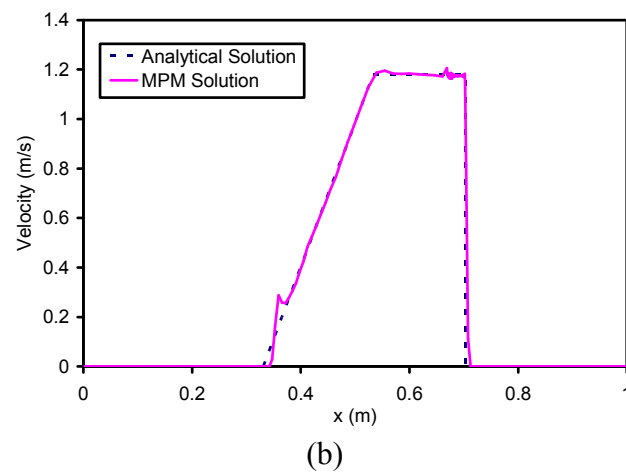
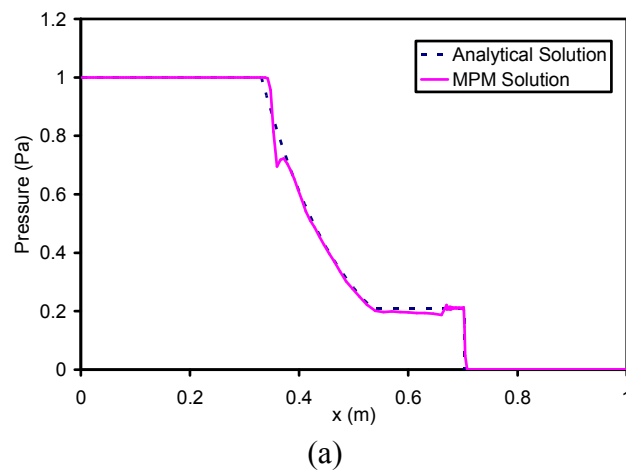
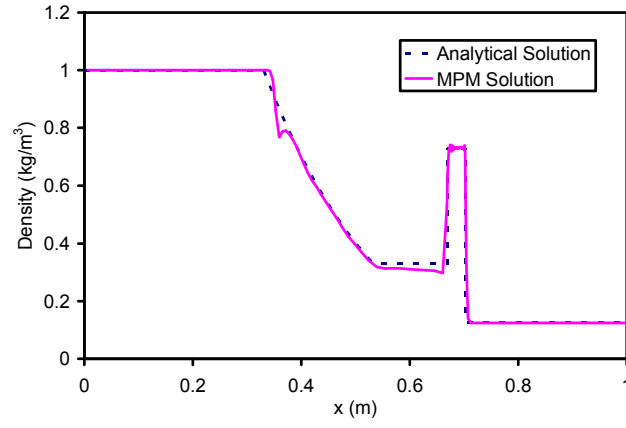
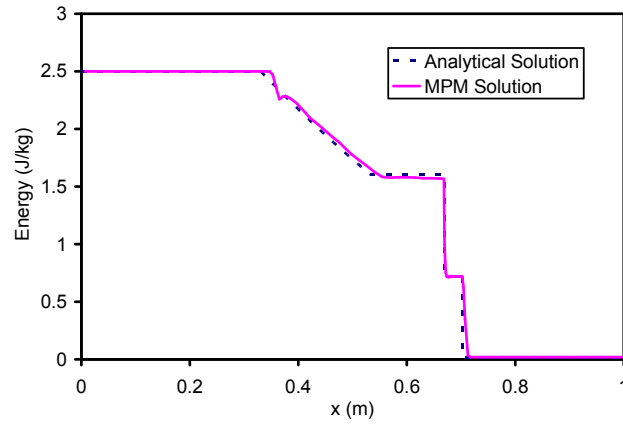


Figure 4.13 MPM solutions with artificial viscosity (averages of material points initialized in every two consecutive cells)





(c)



(d)

Figure 4.14 MPM solutions with artificial viscosity (averages of material points initialized in every four consecutive cells)

4.4.2 Impact between a membrane and an elastic solid

An example of a cuboid impacting a net is used to validate the MPM formulation for thin membranes. As shown in Figure 4.15, a cuboid solid is initially positioned above the center of a stationary net. At time $t=0$, the cuboid moves toward the net with a velocity of 1 m/s along the z -direction. Both the cuboid and the net are elastic, and their dimensions and material properties are listed in Table 4.1 and 4.2, respectively.

The MPM model is composed of 53500 material points with 40000 for the net and 13500 for the elastic cuboid. The net is triangulated with 77922 triangles. The computational mesh is built with cubic cells and three cell sizes are employed, namely, 0.05 m, 0.025 m and 0.02 m. Moreover, all simulations are performed with a time step of 1×10^{-5} s. Figure 4.16 presents the time history of the z -directional displacement at the central point of the cuboid by the MPM and the LS-DYNA. As can be seen from the figure, the solutions by the MPM and the LS-DYNA reach a good agreement and the MPM solutions are convergent as the mesh size becomes smaller. The deformations of the net at various times are shown in Figure 4.17 (0.02 m mesh size).

Table 4.1 Dimensions of the cuboid and the net

Continuum body	Length (m)	Width (m)	Height or Thickness (m)
Cuboid	0.2	0.2	0.1
Net	1	0.2	0.0125

Table 4.2 Material properties of the cuboid and the net

Continuum body	Young's Modulus (Pa)	Poisson's ratio	Density (kg/m^3)
Cuboid	2×10^7	0.2	4000
Net	2×10^7	0.0	2000

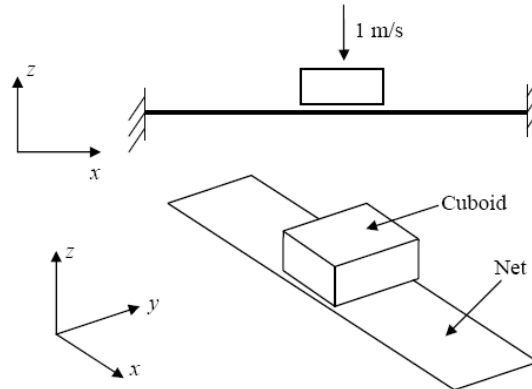


Figure 4.15 An elastic cuboid impacting a net

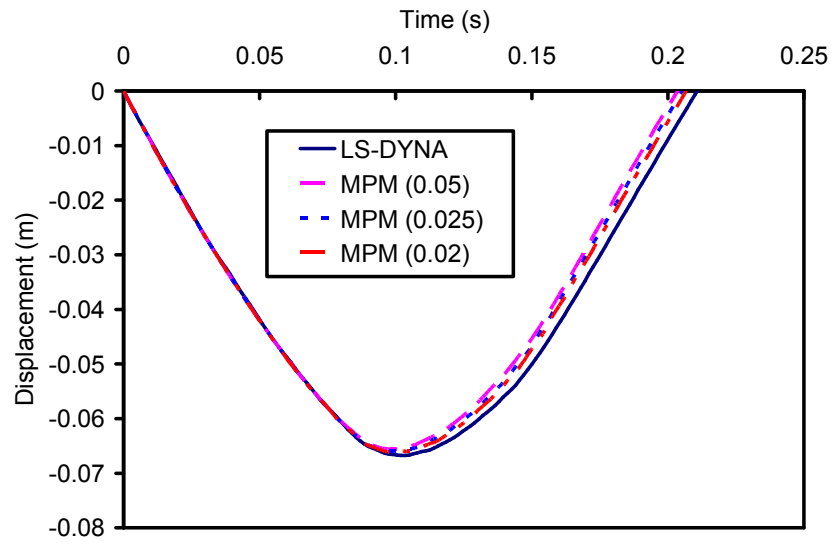
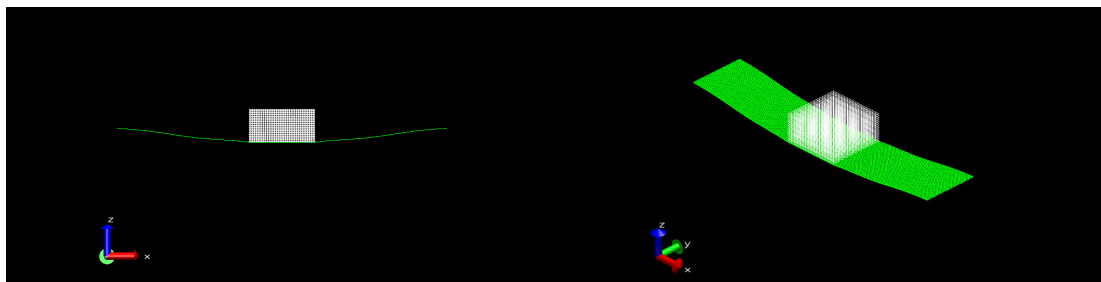
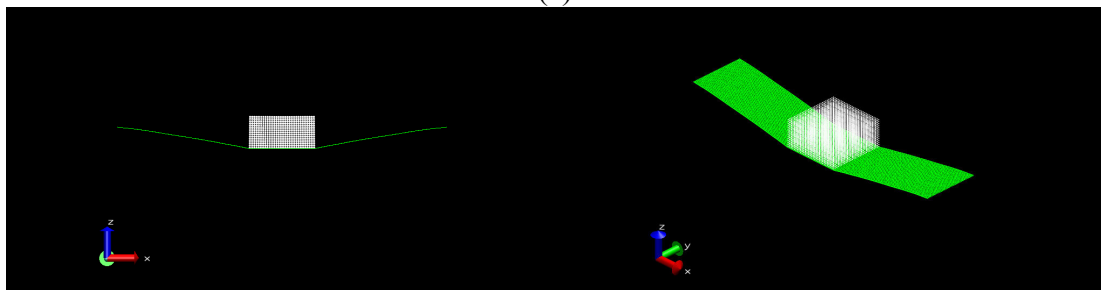


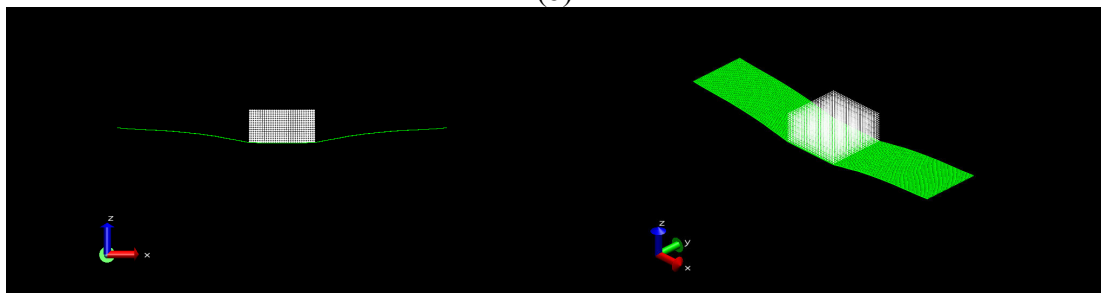
Figure 4.16 Time history of the z -directional displacement at the central point of the cuboid



(a)



(b)



(c)

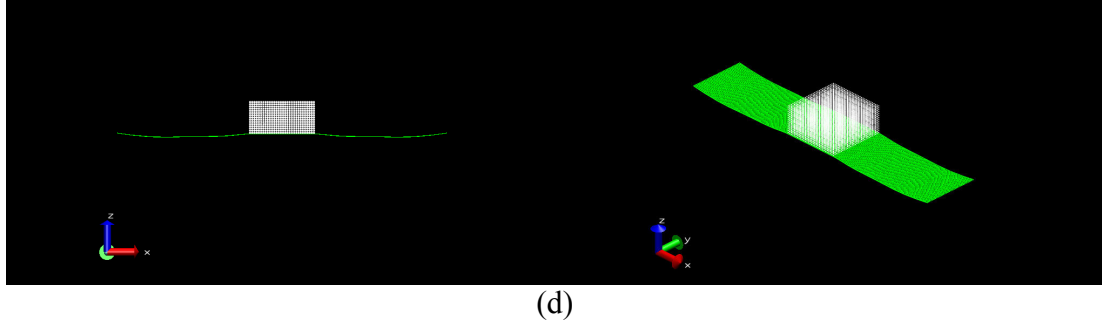


Figure 4.17 Material point position plots for the simulation of a cuboid impacting a net:
(a) $t=0.05$ s, (b) $t=0.1$ s, (c) $t=0.15$ s, (d) $t=0.2$ s (0.02 m mesh size)

4.4.3 Simulation of fluid-membrane interaction

This example is to demonstrate the MPM formulation for fluid-membrane interaction. As shown in Figure 4.18, a gas-filled box is covered by a flat membrane and other walls of the box are rigid. One elastic cube is put at the center of the membrane. The membrane perimeter is fixed and the gas in the box has an initial pressure of 800 Pa. Due to the pressure difference between the inside and outside of the box, the gas will expand and the membrane is displaced. Eventually, the cube will release from the membrane. During the time period of this simulation, no release is considered and the cube always has a close contact with the membrane.

The box is 0.2 m in length, 0.2 m in width and 0.1 m in height. The 0.01m-thick square membrane, hence, has a side length of 0.2 m. The cube has a side length of 0.04 m. The membrane is triangulated with 19602 triangles and represented by 10000 material points. The material points for the cube and the gas are initialized by the standard cell-based algorithm (York II, 1997), and there are 13824 solid points for the cube and 48000 fluid points for the gas. The linear elasticity is used for the membrane and cube with elastic parameters given in Table 4.3. The ideal-gas EOS is adopted for the gas and the artificial

viscosity is used with $c_0=2.0$ and $c_1=1.0$. The computational grid is constructed of cubic elements with the side length being 0.01m, and a time step of 1×10^{-5} s is employed. The z -directional displacement at the central point of the cube is given in Figure 4.19. The good match between the MPM and LS-DYNA solutions demonstrates that the MPM can solve fluid-membrane interaction problems without using additional algorithms. The deformed shapes of the membrane at various times are shown in Figure 4.20. Due to the inertia of the cube, the membrane points interacting with the cube have smaller velocities than other membrane points. Therefore, a concave at the membrane center can be observed in the figure.

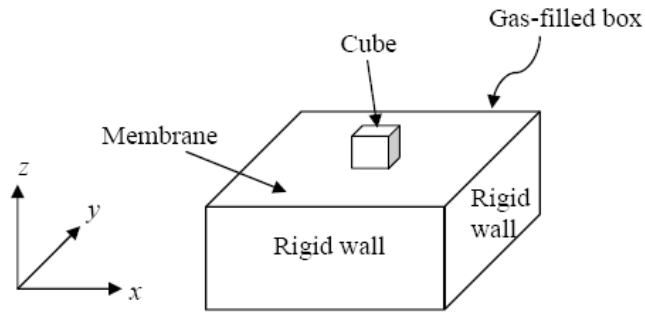


Figure 4.18 Setup of the fluid-membrane interaction problem

Table 4.3 Material properties of the cube and the membrane

	Young's Modulus (Pa)	Poisson's ratio	Density (kg/m ³)
Cube	1×10^7	0.2	1000
Membrane	1×10^5	0.45	1000

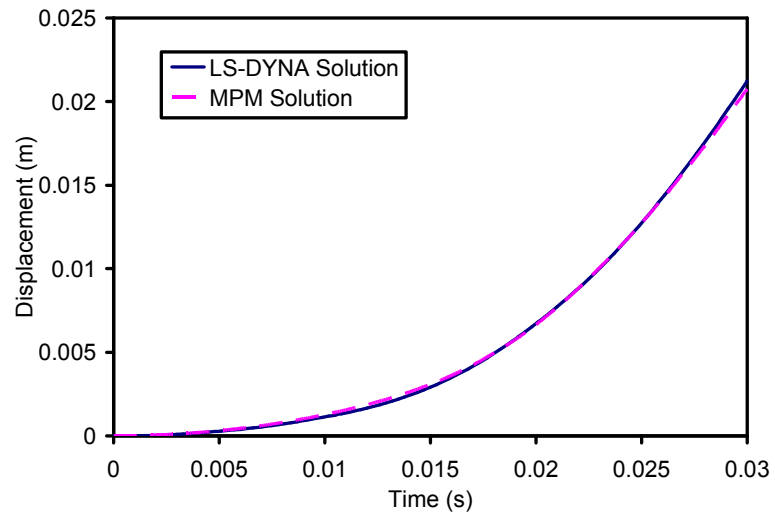
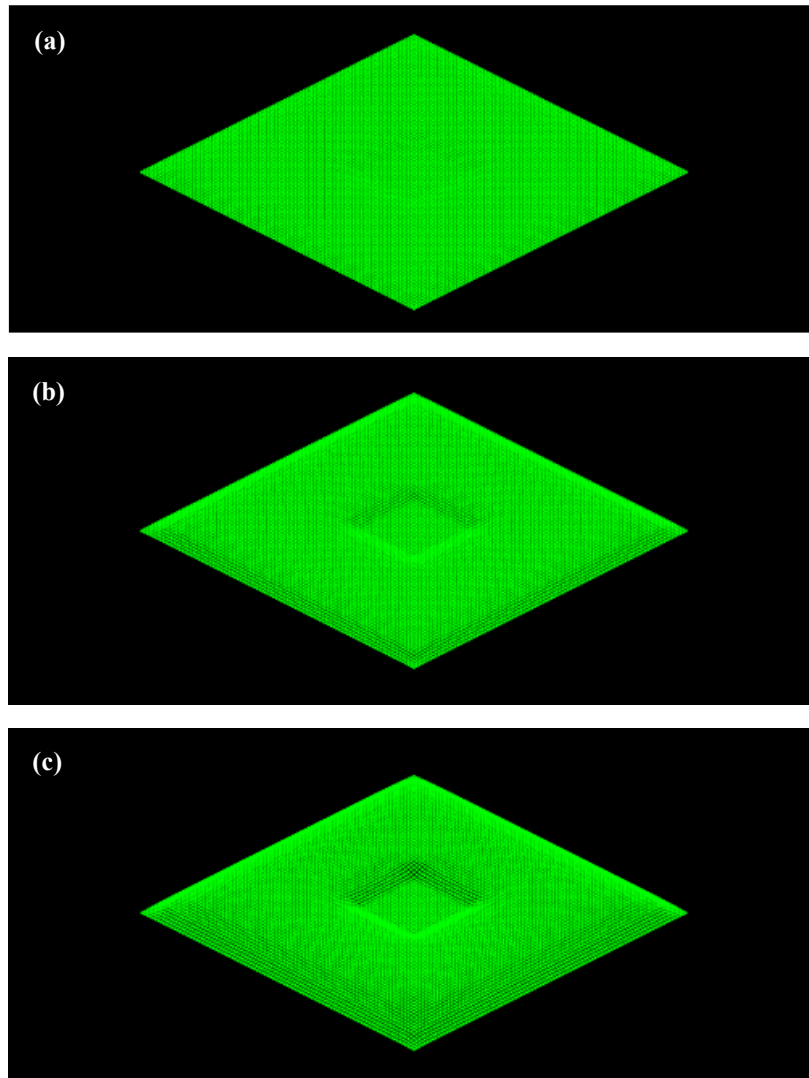


Figure 4.19 Time-history of the z-directional displacement at the central point of the cube



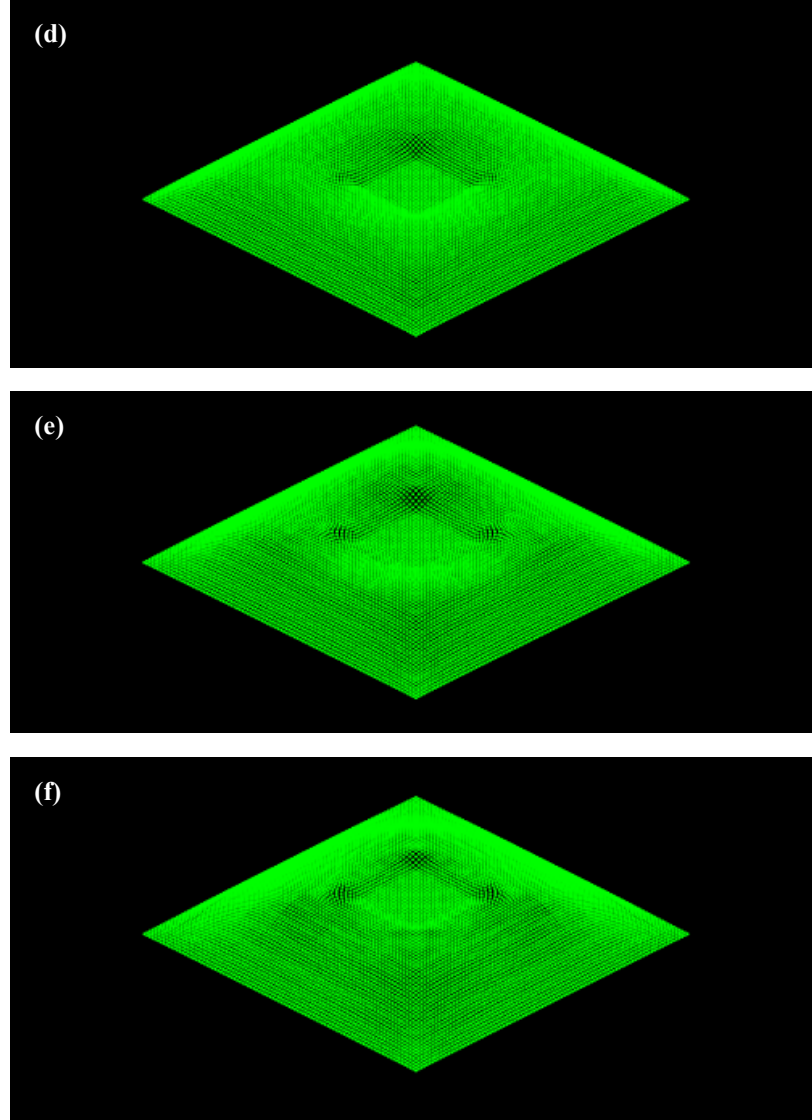


Figure 4.20 Deformed shapes of the membrane at various times: (a) $t=0.005$ s, (b) $t=0.001$ s, (c) $t=0.015$ s, (d) $t=0.02$ s, (e) $t=0.025$ s, (f) $t=0.03$ s

4.5 Summary

The three-dimensional MPM formulations for membranes, fluids and fluid-membrane interaction are discussed. For membrane and fluid points, appropriate assumptions and constitutive models are applied for the computation of their stresses. Then, the internal forces at grid nodes from material points are collected for solving the discrete equations

of motion. Due to the coupling of membrane and fluid points via the grid nodes, the MPM is able to treat the fluid-membrane interaction without resorting to any other contact algorithms. Three examples are solved with the proposed MPM formulations. The results reasonably agree with the analytical or FEM solutions, and demonstrate that the MPM is a viable method for the simulation of the piercing process in piezo-ICSI.

CHAPTER 5

SIMULATIONS OF PIEZO-ICSI

5.1 Introduction

The introduction of a piezo actuator has proven to greatly improve the success rate of the ICSI for human and mouse (Kimura and Yanagimachi, 1995; Yanagida et al., 1999). When electricity is applied to the piezo actuator, the piezo crystal contained in the actuator would extend and thereby exert forces on the attached injection micropipette. By adjusting the input voltage, the movement of the micropipette could be controlled more precisely, thus facilitating the piercing process and causing less damage to the oocyte. The piezo-ICSI procedure discussed in this study is the same as that used by Ediz and Olgac (2004). As shown in Figure 5.1, a piezo-drill consists of a piezo actuator and a pipette holder, and an injection micropipette is connected to the holder. The voltage applied to the piezo actuator is sketched in Figure 5.2 and can be adjusted by three parameters, namely, amplitude, duration and frequency. Figure 5.3 illustrates the setup of the piezo-ICSI procedure. In the piezo-ICSI procedure, the selected mouse oocyte is held by a holding pipette and the injection micropipette tip gently contacts the oocyte at the opposite position. The oocyte and the pipette tips are all immersed in a droplet of medium which is completely covered by mineral oil. A small amount of mercury is added to the injection pipette from its proximal end. When a voltage is applied to the piezo actuator, the motion of the injection pipette is initiated due to the extension of the piezo crystal in the actuator, and the zona pellucida is pierced. The injection pipette is inserted into the

egg and pushed to sag the oocyte membrane. The pulse electricity is applied again to pierce the membrane. Then, the sperm contained in the injection pipette is released and the pipette is withdrawn.

Currently, most piezo-ICSI experiments are conducted with a mercury-filled injection micropipette. However, the use of toxic mercury in piezo-ICSI may result in lower survival and fertilization rates of the oocyte after piezo-ICSI as well as birth defects in embryos. Therefore, an alternative piezo-ICSI procedure without mercury is desired, for which a scientific understanding on the role of mercury in the piercing process is necessary. In this Chapter, the zona piercing process in piezo-ICSI is simulated with the MPM. Firstly, the response of the mouse oocyte during the zona piercing process is studied to find the piercing mechanism in piezo-ICSI, where the oocyte, pipette tips and medium fluid are included in the MPM model. To the author's knowledge, no work has been done to simulate the zona piercing process in the piezo-ICSI. Secondly, the transient response of the injection micropipette due to the piezo pulse is analyzed with the FEM for the understanding of the effect of mercury on the vibration of the injection micropipette.



Figure 5.1 Injection pipette and piezo-drill (Ediz and Olgac, 2004)

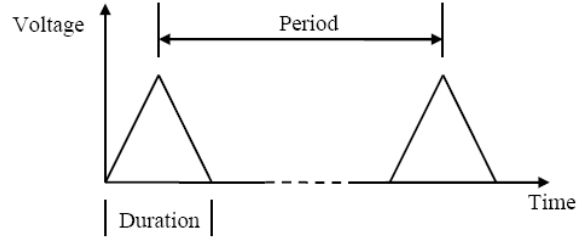


Figure 5.2 Voltage applied to the piezo-drill

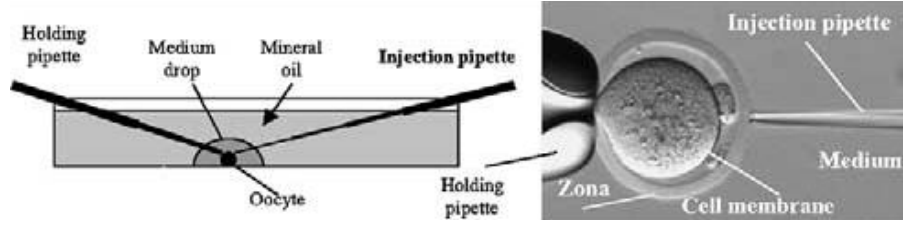


Figure 5.3 Setup of the piezo-ICSI (Ediz and Olgac, 2004)

5.2 Equation of State for Medium and Cytoplasm

The medium used to stabilize the sperm in the piezo-ICSI method is the polyvinylpyrrolidone (PVP, 12%), which is close to water in physical properties (Fan et al., 2006). Thus, the EOS for water is adopted for the fluid outside the oocyte. It is also assumed that the EOS for cytoplasm has the same form as that for water with different model parameters. The stiffened gas equation of state, derived from Grüneisen equation, has been extensively used for modeling fluids (Harlow and Amsden, 1971; Menikoff and Plohr, 1989; Cocchi and Saurel, 1997; Haller et al., 2002), and can be expressed as

$$P + (\Gamma + 1)P_{\infty} = \Gamma \rho I \quad (5.1)$$

where Γ is Grüneisen exponent and P_{∞} is a fit parameter. For water, Γ and P_{∞} are 4.0 and 6.13×10^8 Pa, respectively (Lyon and Johnson, 1992; Haller et al., 2002). If $\Gamma + 1 = 1.4$ and $P_{\infty} = 0$, Equation (5.1) is identical to the ideal-gas EOS. The Grüneisen exponent for

cytoplasm is chosen to be equal to that for water, and P_{∞} is determined by the trial and error method. With assumed value of P_{∞} , the MPM is employed to simulate the ICSI experiment illustrated in Figure 5.4 to obtain the axial displacement of the pipette corresponding to a given force f . The appropriate P_{∞} for cytoplasm can then be found by comparing the axial displacements of the pipette from the MPM simulations with the experimental results by Sun et al. (2003).

In the MPM simulations, the force applied to the pipette linearly increases to the desired value and keeps constant thereafter to eliminate the dynamic effect of loading, as shown in Figure 5.5. The fluid outside the oocyte is not modeled because its existence has no effect on the axial displacement of the pipette. The mouse oocyte is 60 μm in diameter, the zona is 4.5 μm in thickness, and the inject micropipette has an outer diameter of 6 μm and an inner diameter of 5 μm . Based on the work by Sun et al. (2003), the zona is elastic with Young's modulus being 17.9 kPa and Poisson's ratio being 0.49. The elastic injection pipette has the Poisson's ratio of 0.21. The Young's modulus of the pipette is set to be 63.4 MPa so that the simulation could be accelerated with a larger time step. Although the Young's modulus of the pipette is different from the real one, the static displacement of the pipette obtained by the simulation would not noticeably change because the pipette is still much stiffer than the oocyte cell. The density values of the cytoplasm, oocyte zona and pipette are respectively 1000, 1100 and 2300 kg/m^3 . In addition, the shear viscosity of the cytoplasm is chosen to be 8.9×10^{-4} Pa·s and Stokes condition is applied for the evaluation of stresses at fluid points.

The spherical membrane surface is discretized into 40962 membrane points and 81920 triangles. The cytoplasm and pipette are represented by 27736 fluid points and 5400 solid

points, respectively. The computational grid is constructed of cubic cells with a side length of $3\text{ }\mu\text{m}$. The force f and time t_1 defined in Figure 5.5 are $0.5\times 10^{-6}\text{ N}$ and $5\times 10^{-6}\text{ s}$, respectively. The time step is $1\times 10^{-9}\text{ s}$ and the total simulation time is $5\times 10^{-4}\text{ s}$. No artificial viscosity is employed for the simulations. Figure 5.6 shows the time-history of the axial displacement of the pipette for the cases of $P_\infty=2.12\times 10^8$ and $2.4\times 10^8\text{ Pa}$. It can be observed that the displacement gradually increases and finally keeps at one constant. This demonstrates that the employed loading function in Figure 5.5 is reasonable. Table 5.1 presents the displacement results of the pipette for different values of P_∞ . The value of 2.12×10^8 is chosen to be P_∞ for cytoplasm. It yields a pipette displacement of $7.324\text{ }\mu\text{m}$, which is 2% different from the experimental result of $7.466\text{ }\mu\text{m}$.

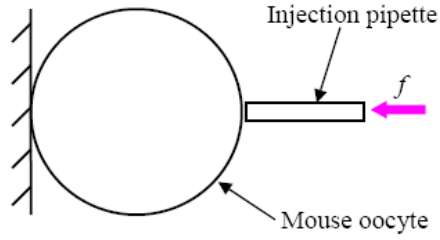


Figure 5.4 Schematic diagram of MPM simulations for the ICSI process

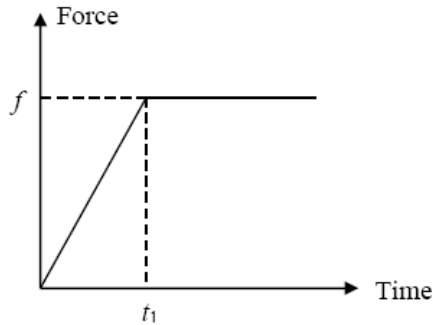
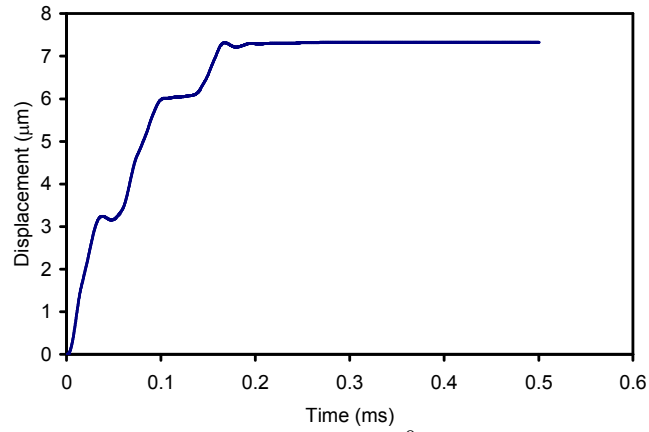
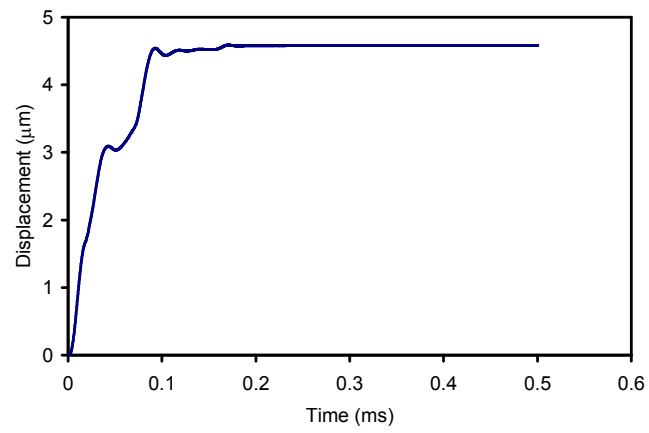


Figure 5.5 External mechanical loading function



(a) $P_{\infty} = 2.12 \times 10^8$ Pa



(b) $P_{\infty} = 2.4 \times 10^8$ Pa

Figure 5.6 Time-history of axial displacement of the injection pipette

Table 5.1 Axial displacement of the pipette

P_{∞} (10^8 Pa)	Displacement of the pipette (μm)
2.1	7.779
2.105	7.766
2.11	7.765
2.115	7.762
2.12	7.324
2.13	7.314
2.14	7.310
2.2	6.062
2.4	4.581

5.3 Constitutive Model of the Mouse Zona Pellucida

The failure criterion for the zona pellucida plays a key role in the simulation of the zona piercing in piezo-ICSI. However, the failure model for the mouse zona pellucida is still ambiguous due to limited experimental and simulation studies. Hence, it is proposed that the existing constitutive models be modified for the mouse zona pellucida and the model parameters be adjusted according to the experimental observation. Two constitutive models, namely, the isotropic elastodamage model (Chen and Schreyer, 1995) and the discontinuous decohesion model (Schreyer et al., 2002; Chen et al., 2005), are used for the mouse zona in this work.

The Clausius-Duham inequality from the principles of thermodynamics is

$$-\dot{U}(\boldsymbol{\varepsilon}, I_i) + \boldsymbol{\sigma} : \dot{\boldsymbol{\varepsilon}} \geq 0 \quad (5.2)$$

where U is the internal energy per unit volume, and I_i ($i=1,2,\dots,n$) is the internal variable representing the internal material constitution. Based on standard arguments (Coleman and Noll, 1963; Coleman and Gurtin, 1967) and the assumption that the damage unloading is elastic, it is followed that

$$\boldsymbol{\sigma} = \frac{\partial U}{\partial \boldsymbol{\varepsilon}} \quad (5.3)$$

For an elastodamage model, a decoupled theory is developed by assuming

$$U(\boldsymbol{\varepsilon}, I_i) = U^e(\boldsymbol{\varepsilon}) + U^d(\boldsymbol{\varepsilon}, I_i) \quad (5.4)$$

$$U^e = \frac{1}{2} \boldsymbol{\varepsilon} : \mathbf{E}^e : \boldsymbol{\varepsilon} \quad (5.5)$$

$$U^d = \frac{1}{2} \boldsymbol{\varepsilon} : \mathbf{E}^d(I_i) : \boldsymbol{\varepsilon} \quad (5.6)$$

where U^e and U^d are internal energy for elastic and damage processes, respectively, \mathbf{E}^e and \mathbf{E}^d are respectively secant stiffness tensors for elastic and damage processes. A combination of Equations (5.3)-(5.6) yields

$$\boldsymbol{\sigma} = \frac{\partial U}{\partial \boldsymbol{\varepsilon}} = \mathbf{E}^e : \boldsymbol{\varepsilon} + \mathbf{E}^d : \boldsymbol{\varepsilon} = \mathbf{E}^{ed} : \boldsymbol{\varepsilon} \quad (5.7)$$

$$\mathbf{E}^{ed} = \frac{\partial^2 U}{\partial \boldsymbol{\varepsilon} \partial \boldsymbol{\varepsilon}} \quad (5.8)$$

in which \mathbf{E}^{ed} is the secant elastodamage stiffness tensor. Since membrane strains can easily determined from the cell deformations observed in the piezo-ICSI experiments, the strain-based elastodamage model is used here for the mouse zona. In addition, the damage is assumed to occur in both deviatoric and volumetric spaces. Based on the work by Chen and Schreyer (1995), the isotropic elastodamage model for the mouse zona is assumed as

$$f^d = \varepsilon_{\max} - S \quad (5.9)$$

$$\mathbf{E}^d = 2c_0 \mathbf{E}^e [\exp(-c_1 \omega) - 1] \quad 0 \leq \omega < \infty \quad (5.10)$$

$$S = S_L (1 + \omega) \quad (5.11)$$

where f^d is the damage surface function, ε_{\max} is the maximum principal strain of the membrane, S is the damage hardening-softening function, S_L is the maximum principal strain corresponding to the elastic limit, c_0 and c_1 are model parameters, and ω is a monotonically increasing variable used to parameterize the damage evolution. The effects of parameters c_0 and c_1 on the change of \mathbf{E}^{ed} are illustrated in Figure 5.7. The effect of

c_0 is demonstrated with $c_1 = 1$, and the effect of c_1 is shown with $c_0 = 1$. It can be found from the figure that large values of c_0 and c_1 result in the faster damage softening.

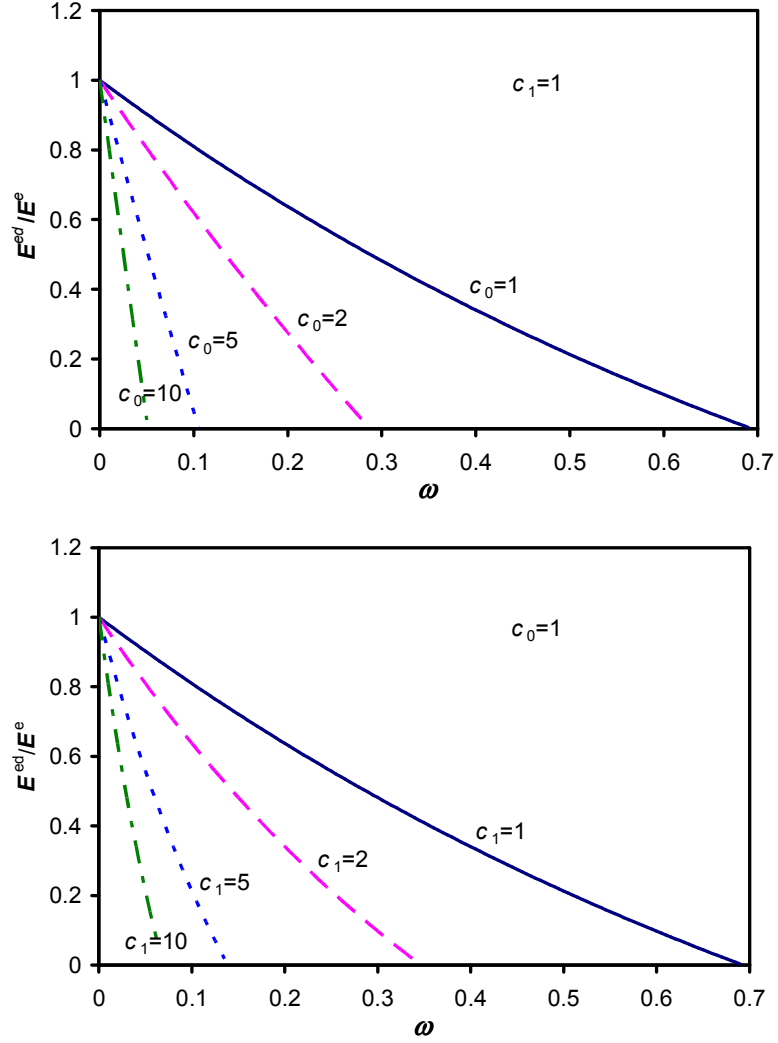


Figure 5.7 Effects of c_0 and c_1 on the change of E^{ed}

The algorithm to solve the elastodamage model in the MPM is described as follows:

- (1) At time level k , evaluate the damage surface $f^d = f^d(\varepsilon_{\max,k}, \omega_{k-1})$ at each membrane point. If $f^d > 0$, damage occurs and go to step (2). Otherwise, the process is elastic and step (3) is followed,

(2) Solve $f^d(\varepsilon_{\max,k}, \omega_k) = 0$ for ω_k and update the elastodamage stiffness tensor \mathbf{E}^{ed} by Equations (5.7) and (5.10),

(3) Update the stress tensor with $\boldsymbol{\sigma}_k = \mathbf{E}_k^{ed} : \boldsymbol{\varepsilon}_k$.

As can be seen, the strain-based elastodamage model can be implemented without invoking iterative algorithm because the total strains are already provided by the MPM computation at each time step. The stress-based damage model, however, requires an iterative scheme to find the unknown stresses.

Another constitutive model used for simulating the mouse zona is the discontinuous decohesion model. It has been found that the transition from continuous failure modes to discontinuous failure modes is characterized by the localized failure, and identified by the discontinuous bifurcation analysis (Chen, 1996; Chen et al., 1999; Chen and Fang, 2001). A bifurcation-based decohesion model, hence, has been developed (Chen et al., 2005). The associated von Mises model with strain hardening and softening is written as

$$d\boldsymbol{\sigma} = \mathbf{E} : (d\boldsymbol{\varepsilon} - d\boldsymbol{\varepsilon}^p) \quad (5.12)$$

$$f(\boldsymbol{\sigma}, I_s) = \begin{cases} 3J_2 - (\sigma_y + E_h I_s)^2 = 0, & 0 \leq I_s \leq I_p \\ 3J_2 - [\sigma_p - E_s (I_s - I_p)]^2 = 0, & I_s > I_p \end{cases} \quad (5.13)$$

$$d\boldsymbol{\varepsilon}^p = d\bar{\lambda} \frac{\partial f}{\partial \boldsymbol{\sigma}} \quad (5.14)$$

$$dI = \sqrt{d\boldsymbol{\varepsilon}^p : d\boldsymbol{\varepsilon}^p} = d\bar{\lambda} \quad (5.15)$$

where $\boldsymbol{\varepsilon}^p$ is the inelastic strain tensor, \mathbf{E} is the isotropic elastic tensor, $f(\boldsymbol{\sigma}, I_s) = 0$ is the flow surface, I_s the internal state variable, J_2 is the second variant of the deviatoric stress tensor, σ_y and σ_p are respectively the yield strength and peak strength of the

material, I_p is the value of the internal state variable corresponding to the peak strength, E_h is the hardening modulus, E_s is the softening modulus, and $\bar{\lambda}$ is a parameter characterizing the loading process. The consistence condition can be expressed as

$$df(\boldsymbol{\sigma}, I) = \frac{\partial f}{\partial \boldsymbol{\sigma}} d\boldsymbol{\sigma} + \frac{\partial f}{\partial I} dI = NN : d\boldsymbol{\sigma} + d\lambda \frac{\partial f}{\partial I} = 0 \quad (5.16)$$

with

$$N = \frac{1}{N} \frac{\partial f}{\partial \boldsymbol{\sigma}} \quad (5.17)$$

$$N = \sqrt{\frac{\partial f}{\partial \boldsymbol{\sigma}} : \frac{\partial f}{\partial \boldsymbol{\sigma}}} \quad (5.18)$$

With Equations (5.14) and (5.17), Equation (5.12) can be rewritten as

$$NN : d\boldsymbol{\sigma} = NN : \mathbf{E} : d\boldsymbol{\varepsilon} - d\lambda NN : \mathbf{E} : N \quad (5.19)$$

A combination of Equations (5.16) and (5.19) yields

$$d\lambda = \frac{N : \mathbf{E} : d\boldsymbol{\varepsilon}}{N : \mathbf{E} : N - \frac{1}{N} \frac{\partial f}{\partial I}} \quad (5.20)$$

By substituting Equations (5.14) and (5.20) into (5.12), we have

$$d\boldsymbol{\sigma} = \mathbf{E}_T : d\boldsymbol{\varepsilon} \quad (5.21)$$

$$\mathbf{E}_T = \mathbf{E} - H \boldsymbol{\sigma}^d \otimes \boldsymbol{\sigma}^d \quad (5.22)$$

$$H = \frac{4G^2}{2J_2 \left(2G - \frac{1}{N} \frac{\partial f}{\partial I} \right)} \quad (5.23)$$

in which G is the shear modulus, and $\boldsymbol{\sigma}^d$ is the deviatoric stress tensor.

Based on the work of Otteson and Runesson (1991), the discontinuous bifurcation condition takes the form of

$$1 - H \mathbf{a}^d \cdot (\mathbf{Q}^{el})^{-1} \cdot \mathbf{a}^d = 0 \quad (5.24)$$

in which $\mathbf{a}^d = \mathbf{n} \cdot \boldsymbol{\sigma}^d = \boldsymbol{\sigma}^d \cdot \mathbf{n}$, and $\mathbf{Q}^{el} = \mathbf{n} \cdot \mathbf{E} \cdot \mathbf{n}$ is the acoustic tensor of elasticity with \mathbf{n} being the vector normal to the moving surface of discontinuity. In the stress space, Equation (5.24) can be written as an ellipse equation, i.e.,

$$\frac{(\bar{\sigma} - \sigma_0)^2}{A} + \frac{\bar{\tau}^2}{B} = 1 \quad (5.25)$$

where $A = \frac{4G + 3K}{3H}$, $B = \frac{G}{H}$, $\sigma_0 = \frac{\sigma_1 + \sigma_2 + \sigma_3}{3}$, $\bar{\sigma}$ and $\bar{\tau}$ are the normal and tangential stresses on the discontinuity surface, respectively, K is the bulk modulus, and the principle stresses follow $\sigma_1 > \sigma_2 > \sigma_3$. On the other hand, the stress state can be represented by a Mohr circle, i.e.,

$$(\bar{\sigma} - \sigma_c)^2 + \bar{\tau}^2 = r^2 \quad (5.26)$$

where $\sigma_c = (\sigma_1 + \sigma_3)/2$, $r = (\sigma_1 - \sigma_3)/2$. The elimination of term $\bar{\tau}$ in Equations (5.25) and (5.26) results in

$$\frac{(\bar{\sigma} - \sigma_0)^2}{A} + \frac{r^2 - (\bar{\sigma} - \sigma_c)^2}{B} = 1 \quad (5.27)$$

Geometrically, the localized failure occurs when the Mohr circle osculates the localization ellipse (Iordache and William, 1998). This means that Equation (5.27) has only one root for $\bar{\sigma}$. By setting the discriminant of Equation (5.27) to be zero, the critical value H^{cr} for the occurrence of the discontinuous bifurcation is thus determined by

$$H^{cr} = \frac{G^2 + 3KG}{3G(\sigma_0 - \sigma_c)^2 + (G + 3K)r^2} \quad (5.28)$$

with the corresponding critical angle of the discontinuous moving surface given by

$$\tan^2 \theta^{cr} = \frac{3G(\sigma_c - \sigma_0) - (G + 3K)r}{3G(\sigma_0 - \sigma_c) - (G + 3K)r} \quad (5.29)$$

The above solution is only valid when $\frac{3G(\sigma_c - \sigma_0) - (G + 3K)r}{3G(\sigma_0 - \sigma_c) - (G + 3K)r} > 0$, as illustrated in

Figure 5.8(a). Otherwise, the critical state and failure angle are given by

$$H^{cr} = \frac{4G + 3K}{3(\sigma_c + r - \sigma_0)^2} \quad (5.30)$$

and

$$\theta^{cr} = 0 \quad (5.31)$$

In other words, the Mohr circle osculates the localization ellipse at the peak point, as shown in Figure 5.8(b). In the MPM computer code developed for the proposed model and bifurcation analysis, both Equations (5.28) and (5.30) are checked at each time step and at each material point. If H exceeds one of the critical H^{cr} values, the discontinuous failure is initiated with the failure angle θ^{cr} which remains fixed during the evolution of the discontinuous failure.

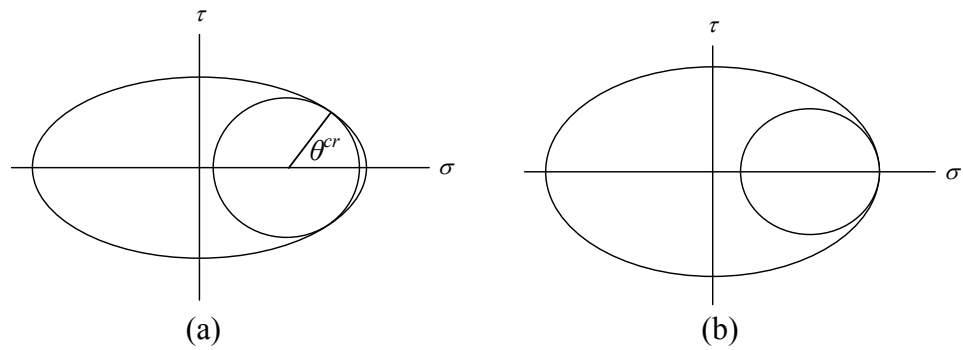


Figure 5.8 Geometry of localized failure condition

Once the onset and orientation of discontinuous failure are identified, a decohesion constitutive model is invoked to predict the failure evolution. According to the work of

Schreyer et al. (2002) and Chen et al. (2005), the decohesion model is formulated as follows:

$$\dot{\boldsymbol{\sigma}} = \mathbf{E} : (\dot{\boldsymbol{\varepsilon}} - \dot{\boldsymbol{\varepsilon}}^d) \quad (5.32)$$

$$\dot{\boldsymbol{\tau}} = \dot{\boldsymbol{\sigma}} \cdot \mathbf{n} \quad (5.33)$$

$$\dot{\mathbf{u}}^d = \dot{\lambda}^d \cdot \mathbf{m} \quad (5.34)$$

$$\dot{\boldsymbol{\varepsilon}}^d = \frac{1}{2L_e} (\mathbf{n} \otimes \dot{\mathbf{u}}^d + \dot{\mathbf{u}}^d \otimes \mathbf{n}) \quad (5.35)$$

$$F^d = \tau^e - U_0 [1 - (\lambda^d)^q] = 0 \quad (5.36)$$

where $\boldsymbol{\varepsilon}^d$ is the decohesion strain tensor with the assumption of no inelastic strain during the decohesion evolution, λ^d is a dimensionless monotonically increasing variable used to parameterize the development of the decohesion, $\boldsymbol{\tau}$ is the stress vector on the decohesion surface, the effective length L_e is the ratio of the element volume to the decohesion surface area within the element, \mathbf{u}^d is the decohesion vector used to determine the decohesion strain, U_0 is the initial energy equal to the product of the reference decohesion \bar{u}_0 and the reference traction $\bar{\tau}_0$, and F^d is the flow surface for the decohesion evolution. For simplicity, the evolution function of decohesion is chosen to be associated, namely

$$\mathbf{m} = \frac{\partial F^d}{\partial \boldsymbol{\tau}} = \bar{u}_0 \frac{\mathbf{A}_d \cdot \boldsymbol{\tau}}{(\boldsymbol{\tau} \cdot \mathbf{A}_d \cdot \boldsymbol{\tau})^{1/2}} \quad (5.37)$$

The effective traction τ^e is then computed as

$$\tau^e = \boldsymbol{\tau} \cdot \mathbf{m} = \bar{u}_0 (\boldsymbol{\tau} \cdot \mathbf{A}_d \cdot \boldsymbol{\tau})^{1/2} \quad (5.38)$$

The positive definite tensor of material parameters, \mathbf{A}_d , takes the form of

$$[A_d] = \bar{\tau}_0^2 \begin{bmatrix} 1 & 0 \\ \frac{\tau_{nf}^2}{\tau_{nf}^2} & \frac{1}{\tau_{tf}^2} \\ 0 & \frac{1}{\tau_{tf}^2} \end{bmatrix} \quad (5.39)$$

with τ_{nf} and τ_{tf} denoting the failure initiation values for the pure tension and shear cases, respectively. At the initiation of decohesion, the consistency condition given by Equation (5.36) yields $\tau^e = U_0 = \bar{u}_0 \bar{\tau}_0$. As a result, it follows that

$$\frac{\tau_n^2}{\tau_{nf}^2} + \frac{\tau_t^2}{\tau_{tf}^2} = 1 \quad (5.40)$$

where τ_n and τ_t are the normal and tangential traction components on the failure surface

at the initiation of decohesion. By introducing $c_m = \frac{\tau_{nf}}{\tau_{tf}}$, τ_{nf} and τ_{tf} can be found for a

known value of c_m since τ_n and τ_t are already known through the bifurcation analysis.

As can be seen, different values of c_m result in various failure modes. For example,

$c_m = 10$ can be used for mode I failure, 0.1 for mode II failure, and 1.0 for mix mode

failure. To meet the consistency condition of $F^d = 0$, a one-step algorithm is designed

by taking a Taylor expansion of F^d about the trial state to the order $(\Delta\lambda^d)^2$, namely,

$$F^d = \frac{\partial F^d}{\partial \lambda} \bigg|_{tr} \Delta\lambda^d + \left\{ \tau^e - U_0 \left[1 - (\lambda^d)^q \right] \right\} \bigg|_{tr} + O(\Delta\lambda^d)^2 = 0 \quad (5.41)$$

With the given local strain increments at each membrane point and at each time step, it is

assumed that no decohesion occurs in the beginning of the time step in order to get the

trial stresses and traction through Equations (5.32) and (5.33), and the value of F^d can

then be determined based on the trial state and existing value of λ^d . If $F^d \leq tol$ with tol

being a small positive number, the step is elastic without further decohesion. Otherwise, $\Delta\lambda^d$ is obtained from Equation (5.41), and decohesion variables are updated at the end of the time step.

As can be seen, the decohesion constitutive equations are invoked with the local strain increments instead of the local total strains. At each time step, the strain increments at membrane points are computed in the global coordinate system, as given in Equation (3.40). Intuitively, it seems that the local membrane strain increments can be determined by rotating these strain increments in the global coordinate system to the local tangential plane. However, this would result in the accumulation of local stresses that are not tangential to the membrane, which leads to forces inconsistent with the membrane orientation (York II, 1997). Thus, it is recommended to keep track of the total membrane strains at each time step and calculate the local strain increments by

$$\Delta\boldsymbol{\varepsilon}'_p = \boldsymbol{\varepsilon}'_p - \boldsymbol{\varepsilon}'_{p,pr} \quad (5.42)$$

where $\Delta\boldsymbol{\varepsilon}'_p$ is the local membrane strain increments, and $\boldsymbol{\varepsilon}'_{p,pr}$ are the local total membrane strains at the previous time step. To demonstrate the validity of Equation (5.42), the fluid-membrane interaction problem in subsection 4.4.3 is simulated by invoking elasticity with the local membrane strain increments in the MPM. Figure 5.9 gives the time history of the z -directional displacement at the center of the cube. It can be seen that the solution by using strain increments for the stress computation is identical to that by invoking elasticity with local total strains.

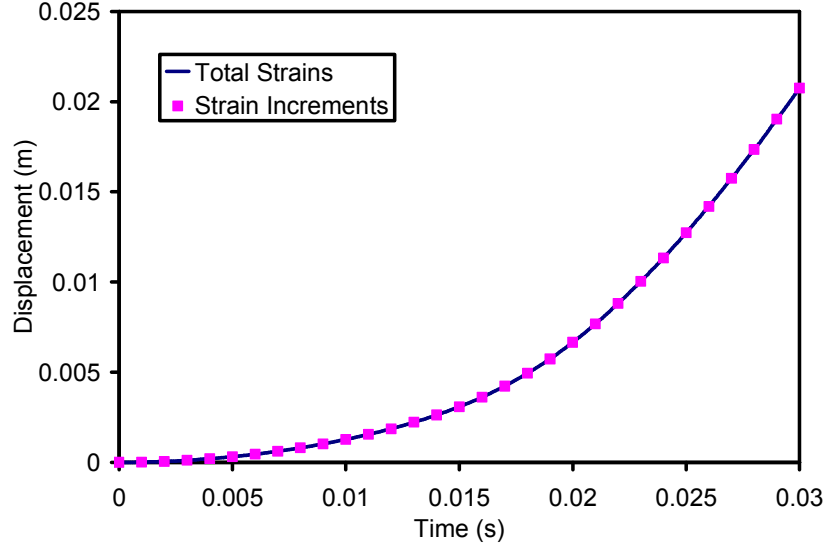


Figure 5.9 Time history of the z -directional displacement at the center of the cube

5.4 The MPM Simulations of the Mouse Zona Piercing in Piezo-ICSI

So far, no consensus of explanation provides the physics of the zona piercing in piezo-ICSI. Kimura and Yanagimachi (1995) claimed that the axial pipette motion pierces the mouse zona pellucida. Ediz and Olgac (2004) found that the pipette has a much larger lateral oscillation than the axial one during the piercing process and argued that the axial vibration is too small to pierce the mouse zona. In this work, we are trying to find the piercing mechanism through the model-based simulation of the mouse zona piercing process.

Compared with the oocyte, the dimensions of the experimental system are much larger. With limited resources, the discretization of the whole problem domain is extremely difficult and costly. Furthermore, it is unnecessary to include the whole domain in the simulation because the response of the oocyte is of major interest. Hence, a small computational domain merely containing the oocyte, tips of the injection and holding

pipettes as well as the surrounding medium is adopted to save computing cost. Due to the use of a finite computational domain, one algorithm is required to prevent the outgoing waves from being reflected by the boundary. Lysmer and Kuhlemeyer (1969) proposed a viscous damping boundary method to absorb the primary and secondary waves traveling through the media. Based on their work, the viscous damping stresses are continuously applied along the boundary to absorb stress waves, as demonstrated in Figure 5.10. The viscous damping stresses are written as

$$S_{xx} = -\rho c_p u_x \quad (5.43)$$

$$S_{xy} = -\rho c_s u_y \quad (5.44)$$

$$S_{xz} = -\rho c_s u_z \quad (5.45)$$

where c_p and c_s respectively denote the velocities of the primary and secondary waves and are calculated by

$$c_p = \sqrt{\frac{(1-\nu)E}{(1-2\nu)(1+\nu)\rho}} \quad (5.46)$$

$$c_s = \sqrt{\frac{E}{2(1+\nu)\rho}} \quad (5.47)$$

Since no secondary wave travels in liquids and gases, the viscous damping forces for fluid media become

$$S_{xx} = -\rho c_f v_x \quad (5.48)$$

$$S_{xy} = 0 \quad (5.49)$$

$$S_{xz} = 0 \quad (5.50)$$

where c_f is the speed of sound in the fluid.

In the MPM, the viscous damping stresses are treated as discrete tractions and applied to the grid nodes. The discrete applied tractions have been given in Chapter 3, namely,

$$\hat{\boldsymbol{\tau}}_i = \int_{\partial\Omega_\tau} N_i(\mathbf{x}_p) \boldsymbol{\tau}_b(\mathbf{x}_p, t) dS \quad (5.51)$$

By introducing the specific traction and the boundary layer thickness, the discrete tractions can be written as

$$\hat{\boldsymbol{\tau}}_i = \sum_{p=1}^{N_p} M_p \boldsymbol{\tau}_b^s(\mathbf{X}_p, t) h_b^{-1} N_i(\mathbf{X}_p) \quad (5.52)$$

where h_b is the boundary layer thickness, and $\boldsymbol{\tau}_b^s$ is the specific traction and defined as $\boldsymbol{\tau}_b$ divided by the mass density. To demonstrate the use of Equation (5.52) for viscous damping forces, a material point on the absorbing boundary and the grid cell to which it belongs are shown in Figure 5.11. The discrete tractions due to viscous damping stresses are given by

$$(f_{x,vis})_i = M_p \frac{S_{xx}}{\rho} h_b^{-1} N_i(\mathbf{X}_p) \quad (i=1,2,\dots,8) \quad (5.53)$$

$$(f_{y,vis})_i = M_p \frac{S_{xy}}{\rho} h_b^{-1} N_i(\mathbf{X}_p) \quad (i=1,2,\dots,8) \quad (5.54)$$

$$(f_{z,vis})_i = M_p \frac{S_{xz}}{\rho} h_b^{-1} N_i(\mathbf{X}_p) \quad (i=1,2,\dots,8) \quad (5.55)$$

where Δx , Δy and Δz are the grid cell sizes in the x -, y - and z -directions, respectively. If the media is incompressible or near incompressible, the boundary layer thickness can be chosen as Δx , Δy or Δz according to the orientation of the boundary.

The application of the proposed absorbing boundary method to the solid has been demonstrated by Shen and Chen (2005). Therefore, a piston-water interaction example is

employed to evaluate the discussed absorbing boundary method for fluids in the MPM. As shown in Figure 5.12(a), the left half of a 1m-long tube is occupied by an elastic piston and the right half is filled with water. The piston moves to the right with an initial velocity of 10 m/s. A finite domain illustrated in Figure 5.12(b) is used in the MPM simulations, and two boundary conditions, i.e., free boundary and absorbing boundary, are applied along its right side. In addition, the whole tube with the fixed right end is also modeled so that the effect of the absorbing boundary can be better examined. In all simulations, the time-history of longitudinal stress σ_{xx} at point p in Figure 5.12(a) is monitored. The material properties of the piston are taken as Young's modulus $E=2.0 \times 10^7$ Pa, Poisson's ratio $\nu=0.2$ and density $\rho=2000$ kg/m³. The water has a shear viscosity of 8.9×10^{-4} Pa·s and a density of 1000 kg/m³, and Stokes condition is assumed. The stiffened-gas EOS is used for water with $\Gamma=4.0$ and $P_\infty = 6.13 \times 10^8$ Pa (Lyon and Johnson, 1992; Haller et al., 2002). The cell size and the time step for the MPM are respectively 0.01 m and 1.0×10^{-7} s. The initialization of material points in each cell is the same as that in the shock tube example in subsection 4.4.1. The total simulation time is chosen to be 2.0×10^{-4} s and no artificial viscosity is used for water points. The time histories of σ_{xx} at point p by simulations with the three different MPM models are presented in Figure 5.13. The comparison of the results between the free boundary and absorbing boundary cases shows that the propagating wave in the water is effectively absorbed by the absorbing boundary. The time histories of σ_{xx} in the absorbing boundary case and the whole domain cases have a satisfied agreement.

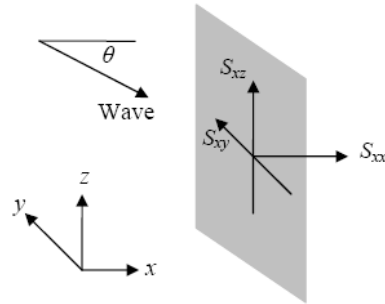


Figure 5.10 Viscous damping boundary method

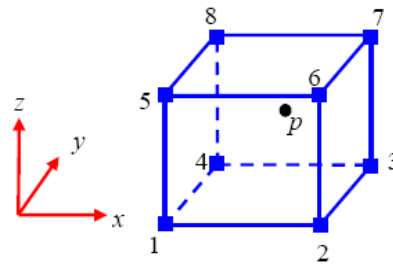


Figure 5.11 A boundary point and the grid cell

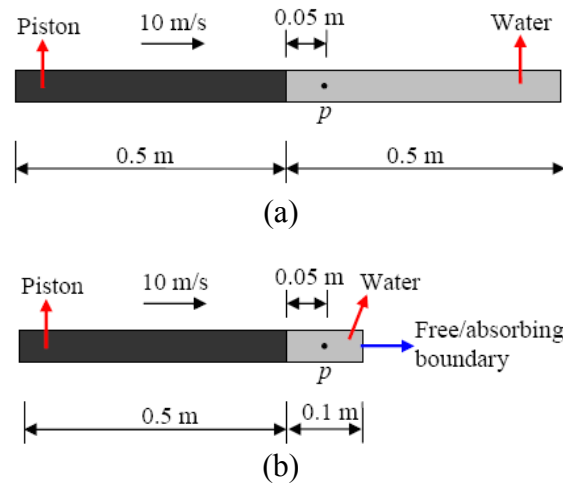


Figure 5.12 The piston problem: (a) piston-water interaction example, (b) free boundary and absorbing boundary

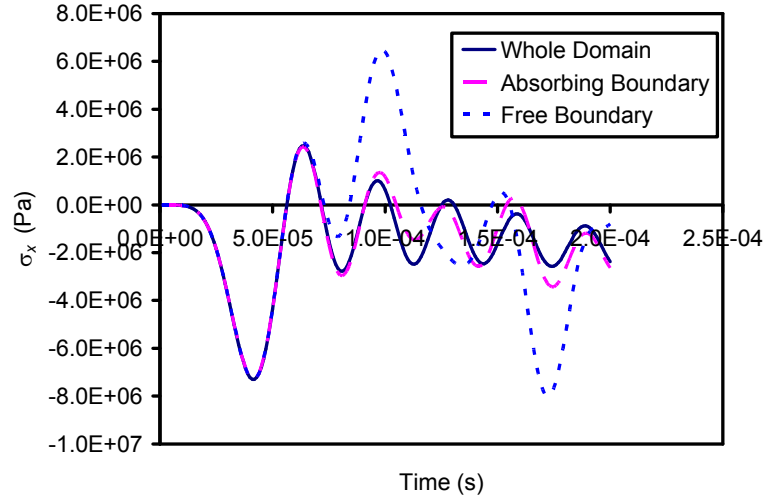


Figure 5.13 The time histories of σ_{xx} at point p

A biomembrane point-load model (Sun et al., 2003) is used to derive parameters of the elastodamage model and the discrete decohesion model for the mouse zona pellucida. Figure 5.14 shows an indentation on the mouse zona pellucida due to the force F by the injection micropipette in conventional ICSI. Because of the axial symmetry, the maximum principal strain used for evaluating the yield surface function of the elastodamage model occurs along the r -axis. Within the indentation, the ring element with the initial width of dr is stretched to a final width of $dr/\cos\theta$. The normal strain along the r -axis can then be computed as

$$\varepsilon_r = \frac{dr/\cos\theta - dr}{dr} = 1/\cos\theta - 1 \quad (5.56)$$

If angle θ is not more than 25° , the small strain assumption is valid. Based on the experimental observation, the largest value of θ is less than 22° . Then, the maximum ε_r should be less than 0.0785 by Equation (5.56). With the consideration of the variation of mouse egg cells, the maximum principal strain corresponding to the failure state of the mouse zona pellucida is assumed to be 0.06. In other words, the membrane point fails if

its maximum principal strain exceeds 0.06. It is also found from experiments that the piercing process is complete in a very short time and the force applied to the oocyte rapidly decreases to zero. As a result, parameters of c_0 and c_1 for the elastodamage model are both set to be 10 to reflect the short piercing process, which yields $S_L=0.05937$. Moreover, the Young's modulus and Poisson's ratio of the mouse zona pellucida are assumed to be 17.9 kPa and 0.5, respectively (Domke et al. 2000; Sun et al., 2003). However, to avoid the floating error, the Poisson's ratio of the mouse zona pellucida is set to be 0.49 instead. Table 5.2 summarizes all parameters of the elastodamage model for the mouse zona pellucida. For the discrete decohesion model formulated earlier, the associated von Mises elastoplasticity model with linear hardening and softening is used before the occurrence of the discontinuous bifurcation, with Young's modulus $E=17.9$ kPa, Poisson's ratio $\nu=0.49$, and yield strength $\sigma_y=1062.795$ Pa. It can be noticed that the elastic limit corresponding to σ_y is equal to S_L in the elastodamage model. In order to describe the abrupt piercing of the mouse zona pellucida, the peak strength, hardening modulus and softening modulus for the von Mises model are respectively set to be 1062.805 Pa, 17.9 Pa and 179 kPa. Once the discontinuous bifurcation is identified, the discrete decohesion model is invoked with $\bar{u}_0=1.0\times 10^{-8}$, $q=1.0$ and $c_m=10.0$ for mode I failure. The failure of the membrane point is characterized by $\lambda^d \geq 1$. It should be noted that stress components of all failure points are nullified while their mass contribution to the inertia of the model still exists. In addition, triangles containing failure membrane points would not be involved in the computation of the material point normal anymore.

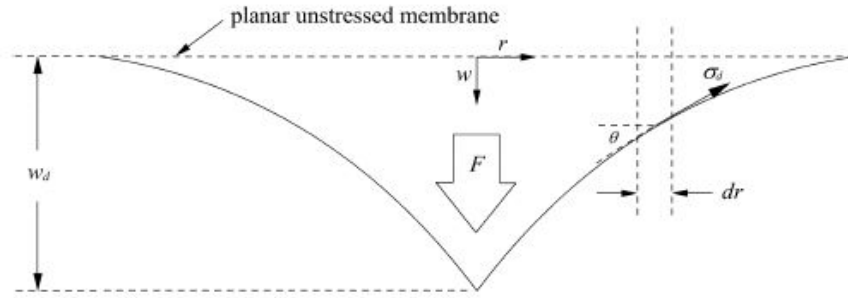


Figure 5.14 The indentation on the mouse zona by the injection pipette (Sun et al., 2003)

Table 5.2 Parameters of elatodamage model for the mouse zona pellucida

Young's modulus	Poisson's ratio	c_0	c_1	S_L
17.9 kPa	0.49	10	10	0.05937

The simulated mouse oocyte is $100\ \mu\text{m}$ in diameter and the zona pellucida is $8\ \mu\text{m}$ in thickness. The spherical zona surface is triangulated with 81920 triangles and represented by 40962 membrane points. The injection micropipette has an outer diameter of $10\ \mu\text{m}$ and an inner diameter of $8\ \mu\text{m}$. To save the computational cost, one $15\ \mu\text{m}$ -long injection pipette tip is modeled with 5400 solid points. The added mass due to mercury inside the injection pipette is evenly assigned to pipette points. The cytoplasm is initially discretized with twenty-seven fluid points in each cell, and points representing the medium fluid outside the oocyte are initialized with one point per cell. Therefore, the total number of fluid points depends on the mesh cell size. For simplicity, the holding pipette tip is modeled as one square plate to hold the oocyte and initialized with one point per cell. The thickness of the plate is three times of the mesh cell size, and its side length is either $70\ \mu\text{m}$ ($5\ \mu\text{m}$ mesh cell) or $72\ \mu\text{m}$ (4 and $6\ \mu\text{m}$ mesh cells). Figure 5.15 shows a MPM model involving the oocyte (cyan points), the injection pipette (white points), the medium fluid (red points) and the holding pipette (blue points). The Young's modulus and Poisson's

ratio for the injection and holding pipettes are 63.4 GPa and 0.21, respectively. Both the cytoplasm and the medium fluid have a shear viscosity of 8.9×10^{-4} Pa·s and a density of 1000 kg/m³, and Stokes condition is assumed for them. The density of the injection pipette is 26441 kg/m³ with the consideration of the added mass resulting from the mercury, and the holding pipette has the same density as glass, i.e., 2300 kg/m³. The density of the mouse zona pellucida is set as 1100 kg/m³. The stiffened-gas EOS is used for the cytoplasm and medium with the parameters listed in Table 5.3. No artificial viscosity is employed for fluid points. The oocyte is assumed to be free of the initial membrane stresses and fluid pressure, and the viscous damping stresses are continuously applied along all boundaries to absorb the outgoing waves.

The MPM simulations are divided into two categories: one is to study the response of the oocyte due to the lateral vibration of the injection pipette, and the other is to find the role of the axial oscillation of the pipette in the piercing process. The effect of the lateral oscillation of the injection pipette on the piercing process is studied firstly. The lateral vibration of the pipette in this study corresponds to the piezo pulse generated by a voltage with a frequency of 2 Hz, a duration time of 60 μ s and an amplitude of 10 V. The total simulation time is 100 μ s, in which the lateral oscillation of the pipette tip is approximated as a sine function with an amplitude of 13.5 μ m and a period of 100 μ s based on the free vibration analysis of the pipette and the experimental observation. It is assumed that there is no slip between the pipette tip and the zona. The computational mesh is constructed of a collection of 8-node cubic elements. A total of three mesh cell sizes, i.e., 4, 5 and 6 μ m, are used for the construction of the background grid. The total the number of material points for each cell size case is given in Table 5.4. The time step

for all MPM simulations is 5.0×10^{-10} s. Figures 5.16-5.18 show the failure patterns of the mouse zona at different times by the MPM simulations with the elastodamage model, and the oocyte deformations by simulations using the discontinuous decohesion model are given in Figures 5.19-5.21. In all figures, the failure membrane points are represented by red points.

From Figures 5.16-5.18, it can be seen that the failure points are concentrated at four corner areas around the contact zone between the pipette tip and the mouse zona pellucida. As the mesh cell size decreases, the failure points come close to the contact zone. This phenomenon indicates the convergence of the failure pattern and the mesh-dependent feature of the elastodamage model. With the discontinuous decohesion model, the failure points are evenly distributed in two narrow areas oriented along the vibration direction of the pipette, as presented in Figures 5.19-5.21. In addition, it is observed that the mesh cell size has little effect on the distribution of the failure points, that is to say, the decohesion model is independent of the mesh size. Overall, in spite of the variation in the failure pattern of the mouse zona, it can be concluded from the MPM simulations that the lateral vibration of the injection micropipette does lead to the failure of the mouse zona pellucida. This is in accordance with the experiment by Ediz and Olgac (2004) and strengthens the claim that the lateral dynamics of the injection pipette plays a critical role in the piercing process of the piezo-ICSI procedure. By examining the deformed shapes of the oocyte illustrated in Figures 5.16-5.21, it is found that the oocyte has a lagged response to the vibration of the pipette tip only when the $6\text{-}\mu\text{m}$ mesh size and the elastodamage model are used. This phenomenon might be due to two factors. Firstly, compared with the mouse oocyte with $100\text{ }\mu\text{m}$ in diameter, the $6\text{ }\mu\text{m}$ mesh cell size is too

coarse to accurately describe the deformation of the oocyte and the failure of the mouse zona pellucida. Secondly, most failure points appear within the first quarter time period in the simulations using the elastodamage model. It is deemed that a combination of the coarse mesh and the early failure would result in the unmatched oocyte deformation with respect to the pipette oscillation.

Table 5.3 Parameters of the stiffened-gas EOS for fluids

Fluid	Γ	P_{∞} (Pa)
Cytoplasm	4.0	2.12×10^8
Medium	4.0	6.13×10^8

Table 5.4 Total number of material points

Mesh Cell Size (μm)	Number of material points			
	Fluid	Membrane	Solid	Total
6	77864	40962	5832	124658
5	128572	40962	5988	175522
4	243966	40962	6372	291300

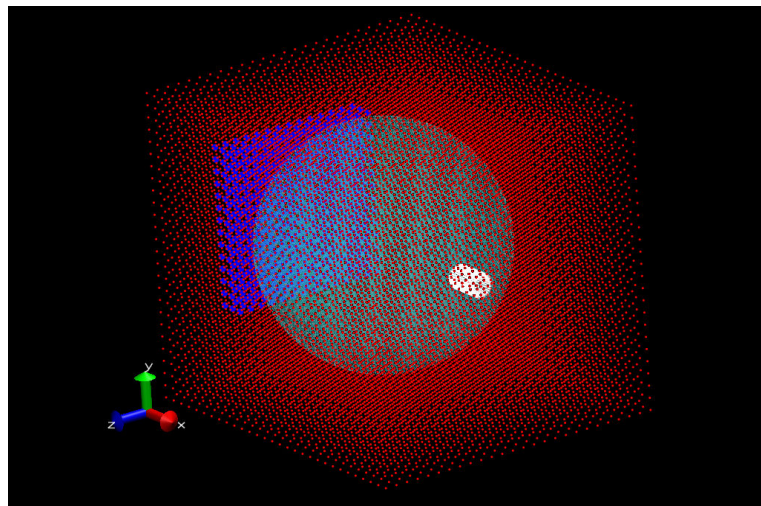
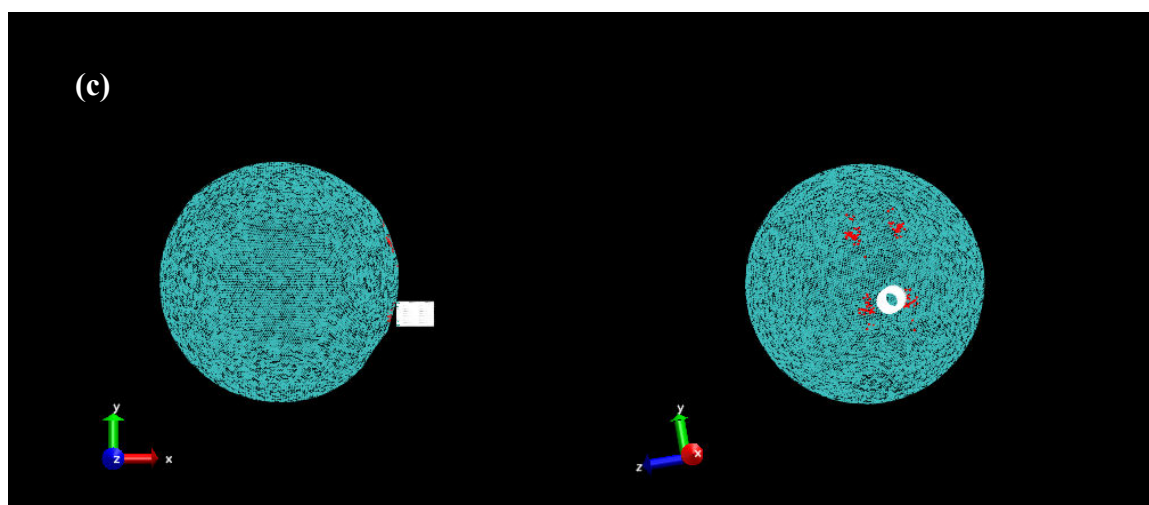
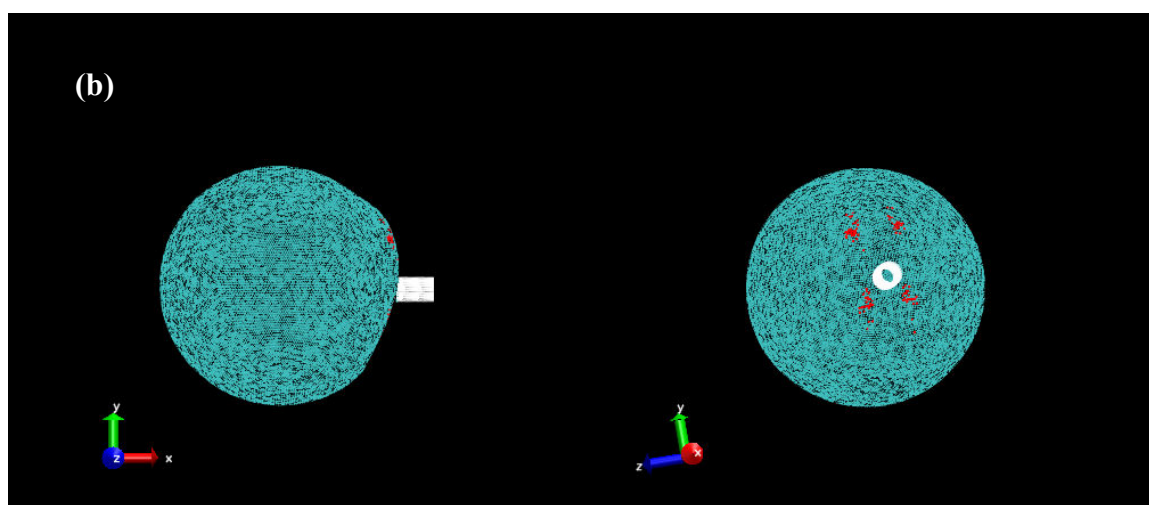
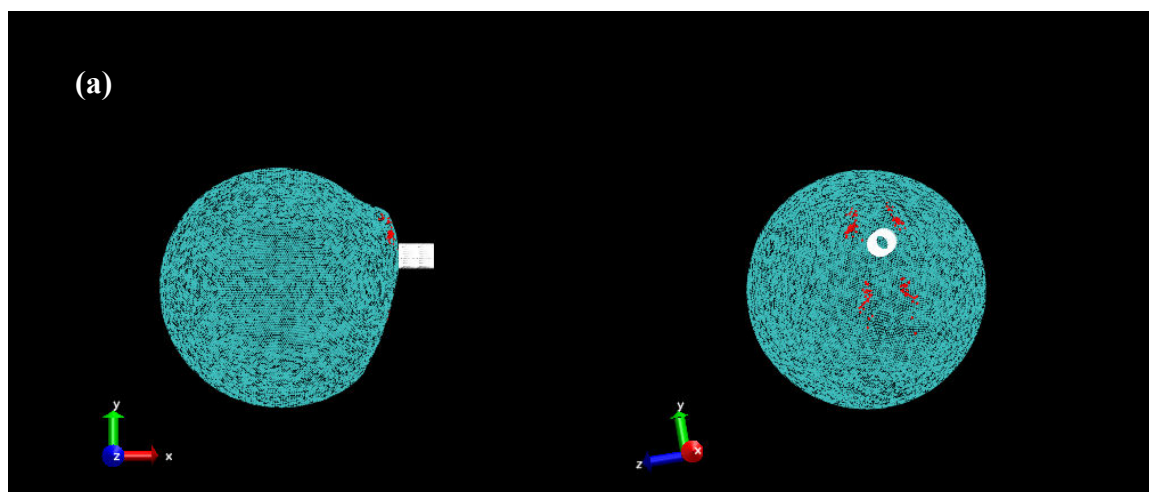


Figure 5.15 The MPM model for the simulations of the piercing process in piezo-ICSI (oocyte: cyan, injection pipette: white, medium: red, holding pipette: blue)



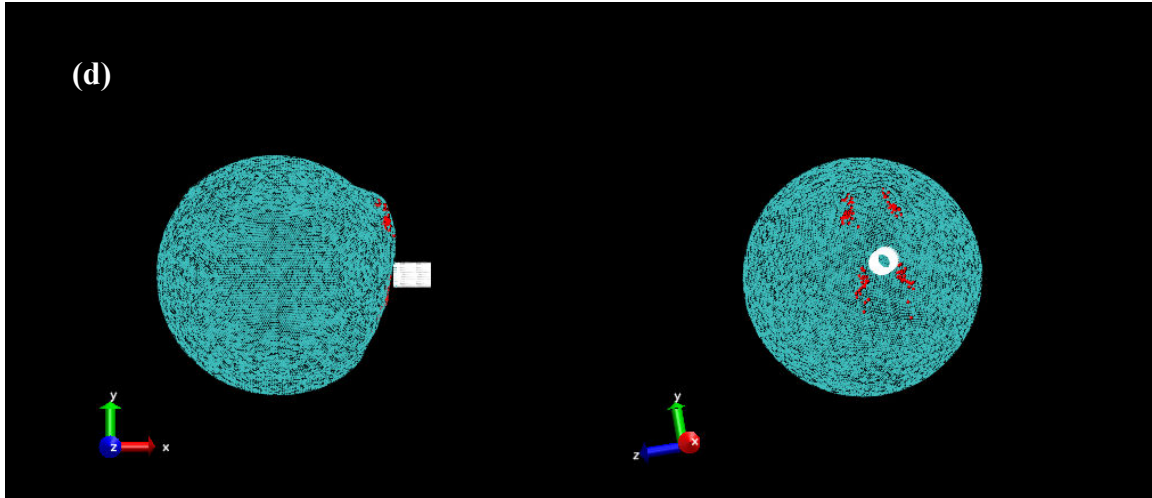
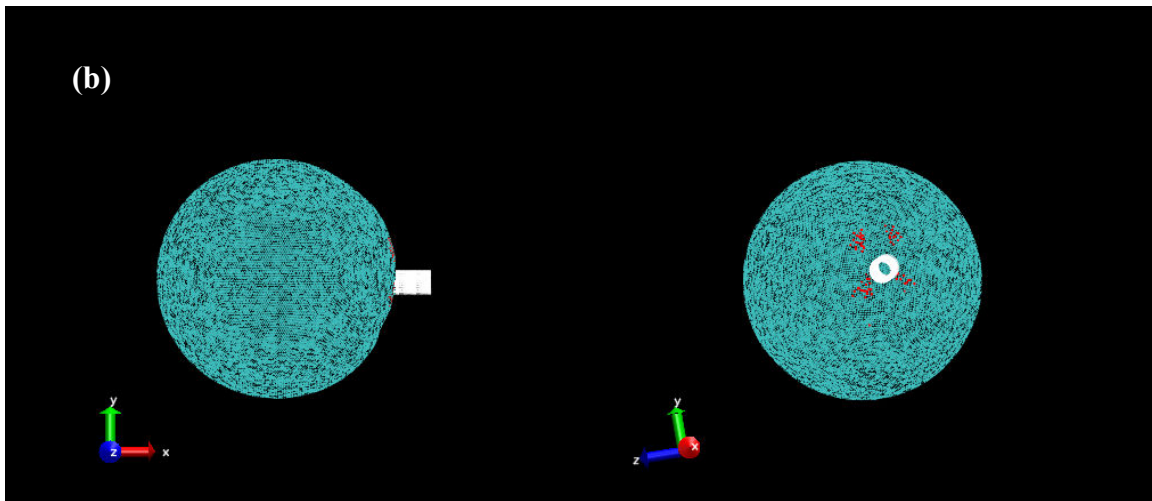
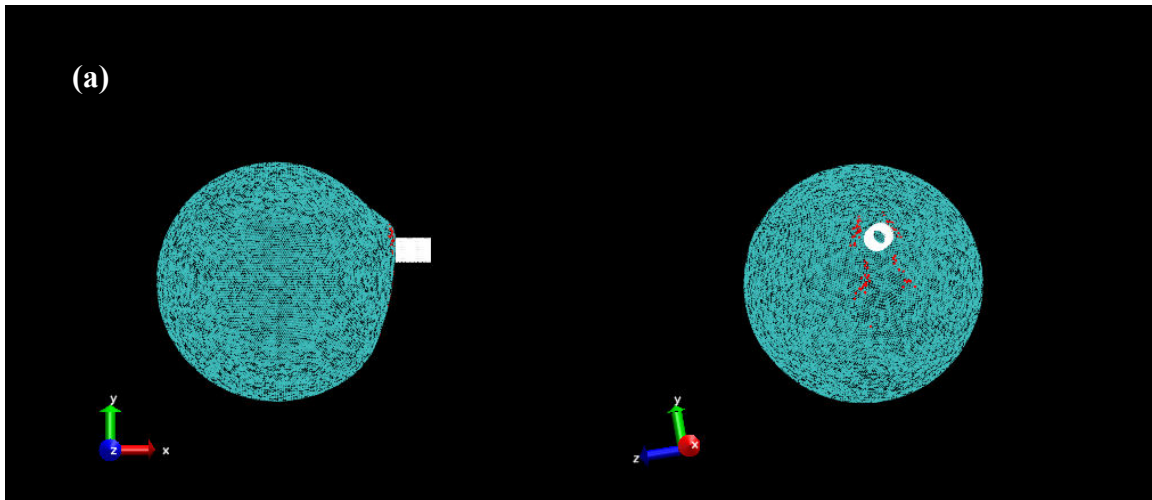


Figure 5.16 Deformation shapes of the oocyte at different times ($6\text{ }\mu\text{m}$ cell size and elastodamage model): (a) $t=28\text{ }\mu\text{s}$, (b) $t=52\text{ }\mu\text{s}$, (c) $t=76\text{ }\mu\text{s}$, (d) $t=100\text{ }\mu\text{s}$



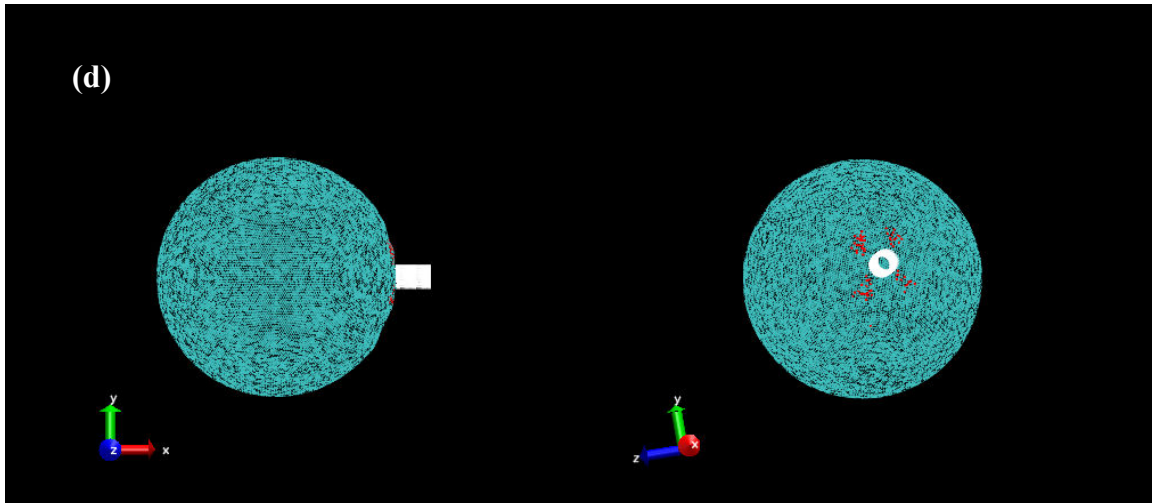
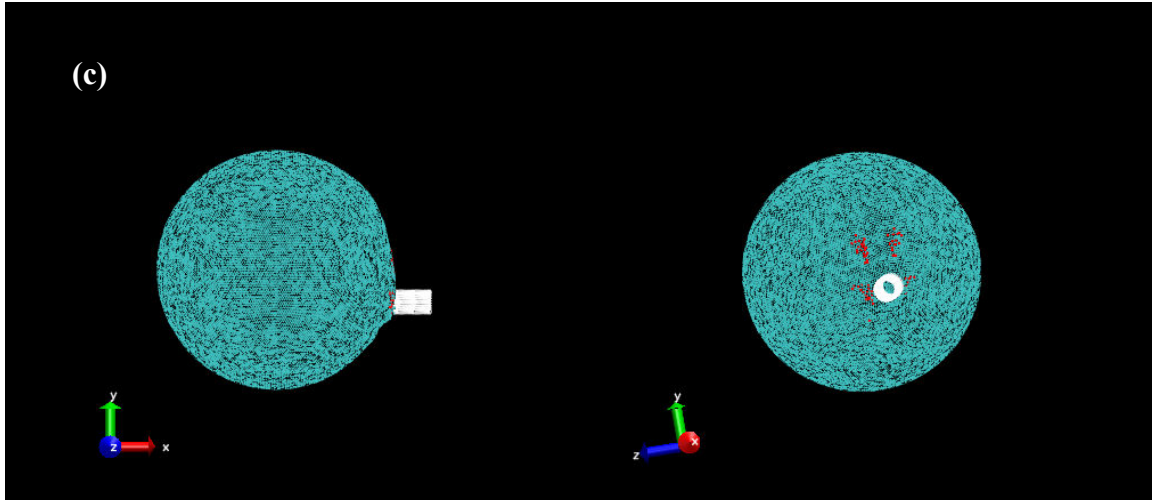
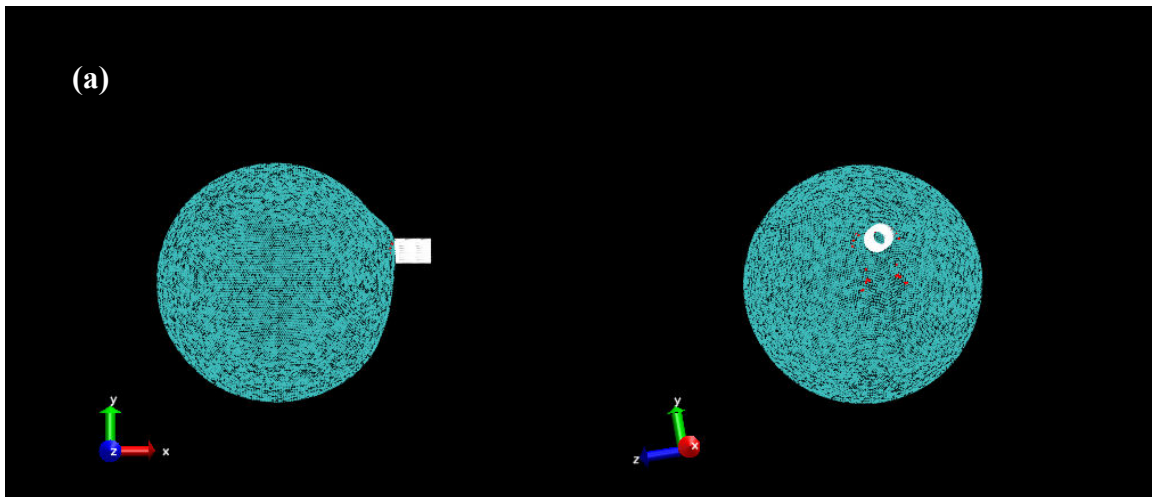


Figure 5.17 Deformation shapes of the oocyte at different times ($5\text{ }\mu\text{m}$ cell size and elastodamage model): (a) $t=28\text{ }\mu\text{s}$, (b) $t=52\text{ }\mu\text{s}$, (c) $t=76\text{ }\mu\text{s}$, (d) $t=100\text{ }\mu\text{s}$



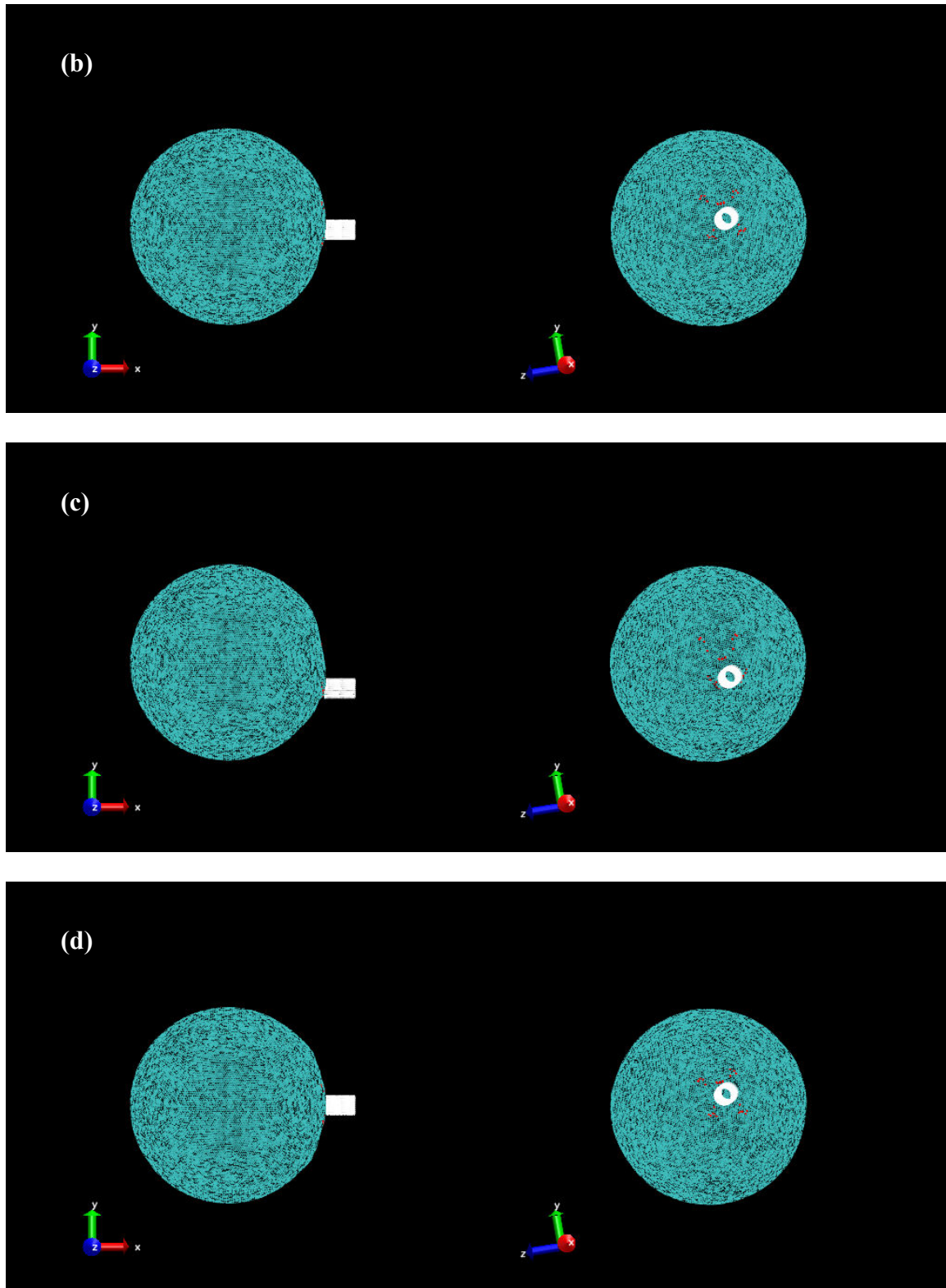
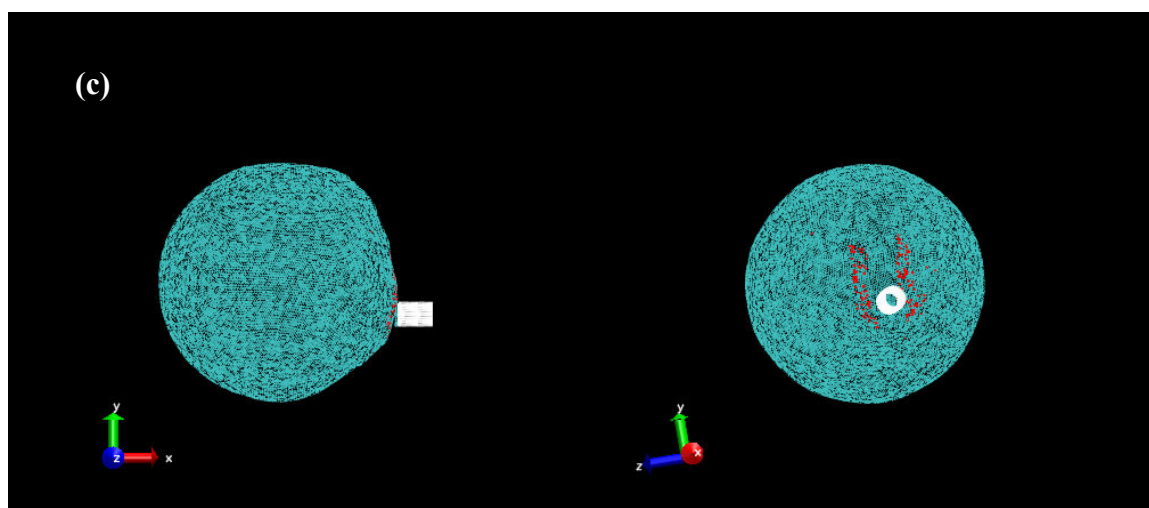
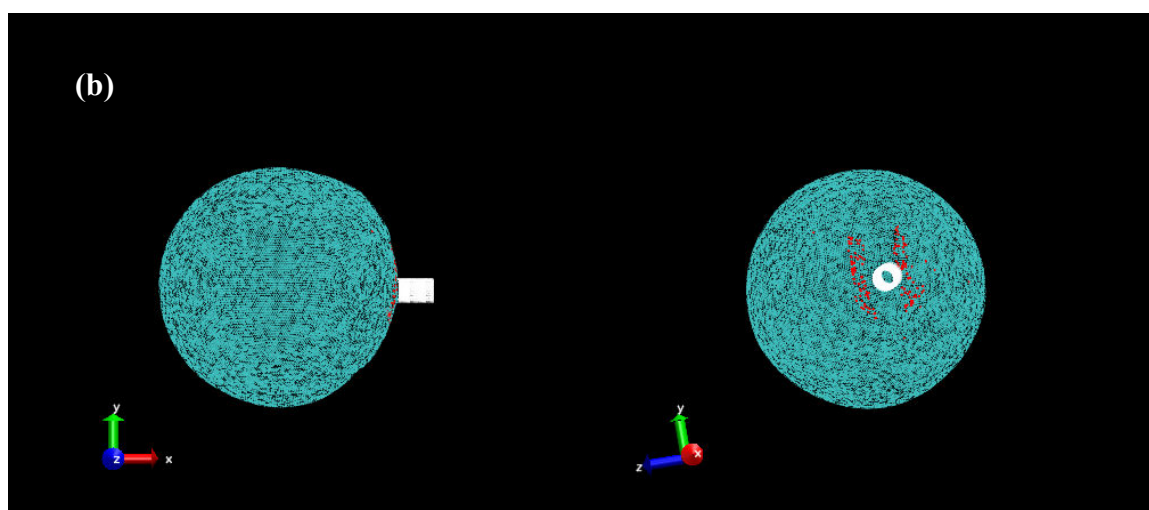
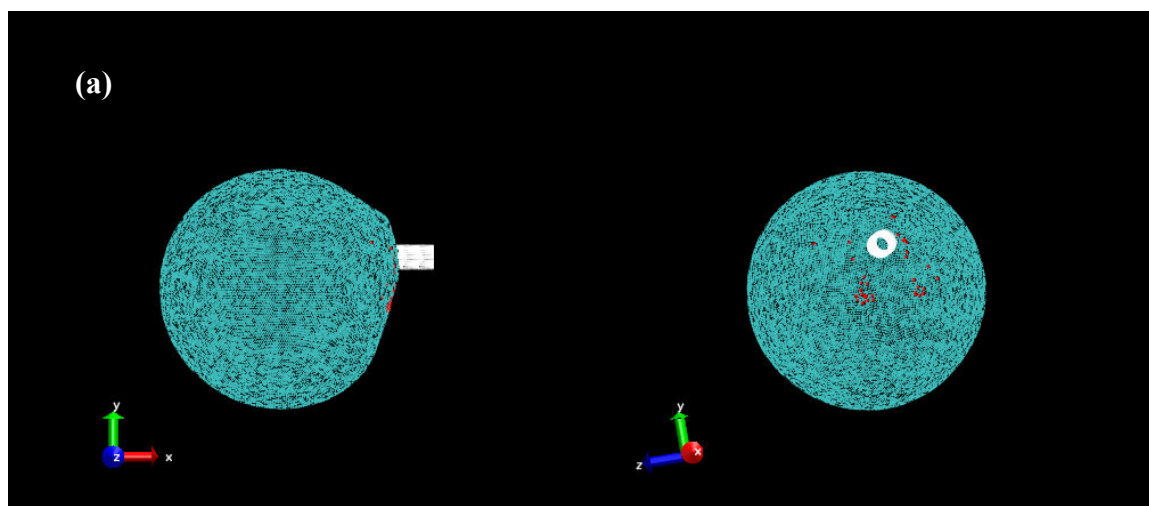


Figure 5.18 Deformation shapes of the oocyte at different times ($4\text{ }\mu\text{m}$ cell size and elastodamage model): (a) $t=28\text{ }\mu\text{s}$, (b) $t=52\text{ }\mu\text{s}$, (c) $t=76\text{ }\mu\text{s}$, (d) $t=100\text{ }\mu\text{s}$



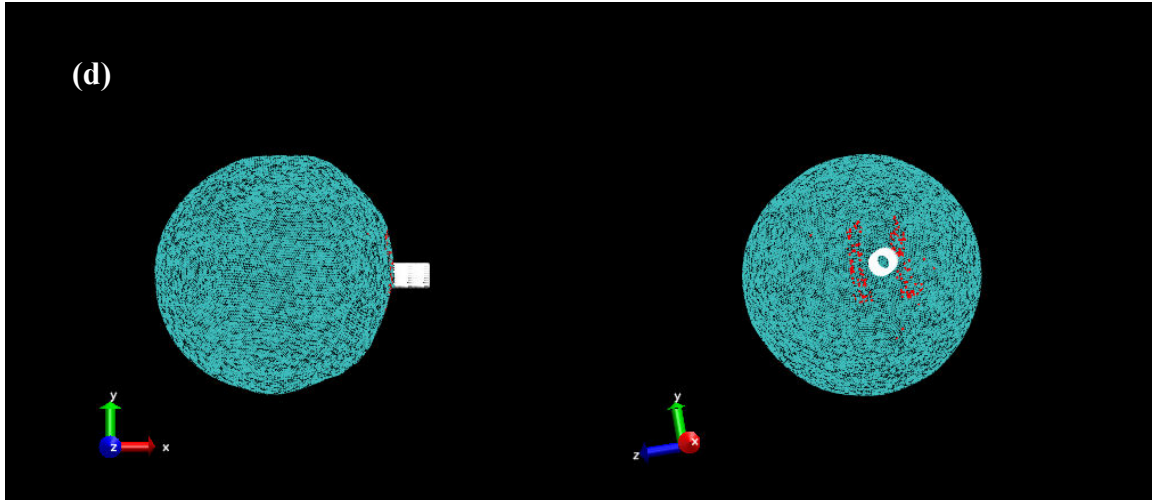
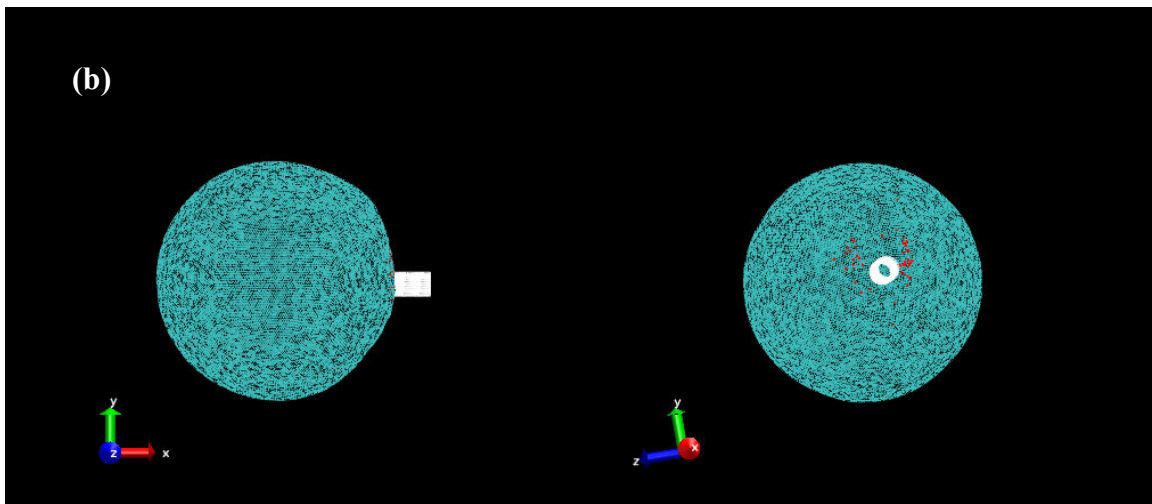
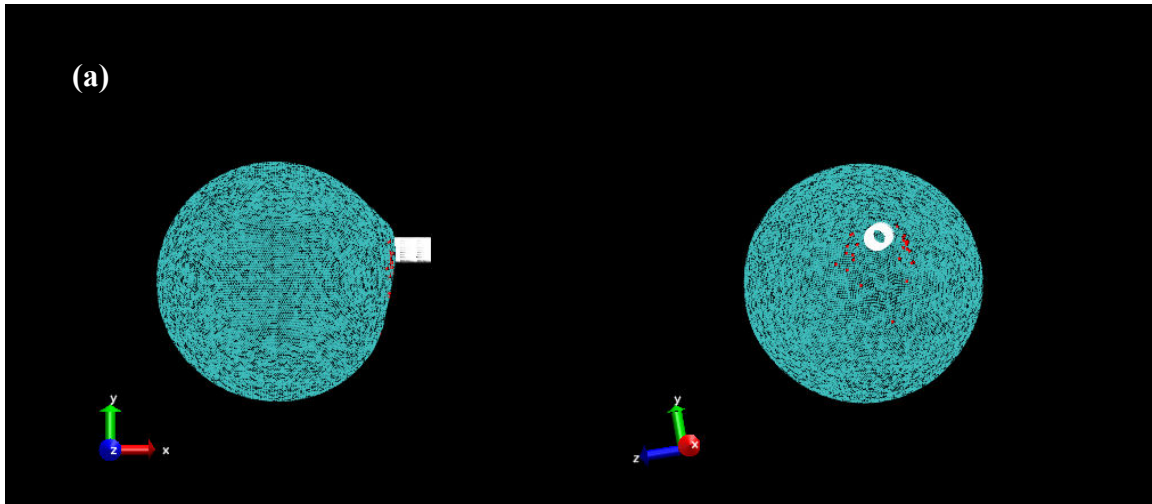


Figure 5.19 Deformation shapes of the oocyte at different times ($6\text{ }\mu\text{m}$ cell size and decohesion model): (a) $t=28\text{ }\mu\text{s}$, (b) $t=52\text{ }\mu\text{s}$, (c) $t=76\text{ }\mu\text{s}$, (d) $t=100\text{ }\mu\text{s}$



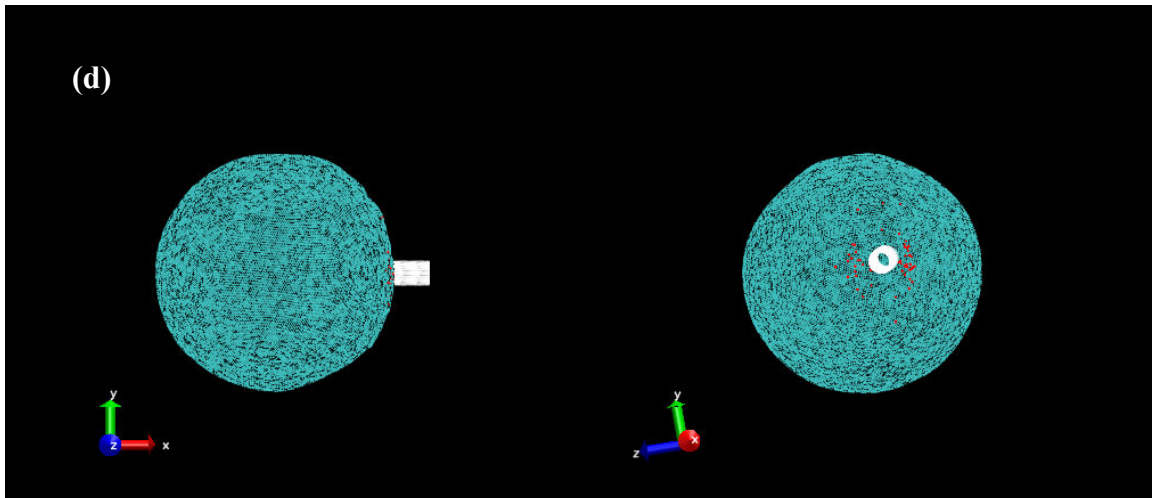
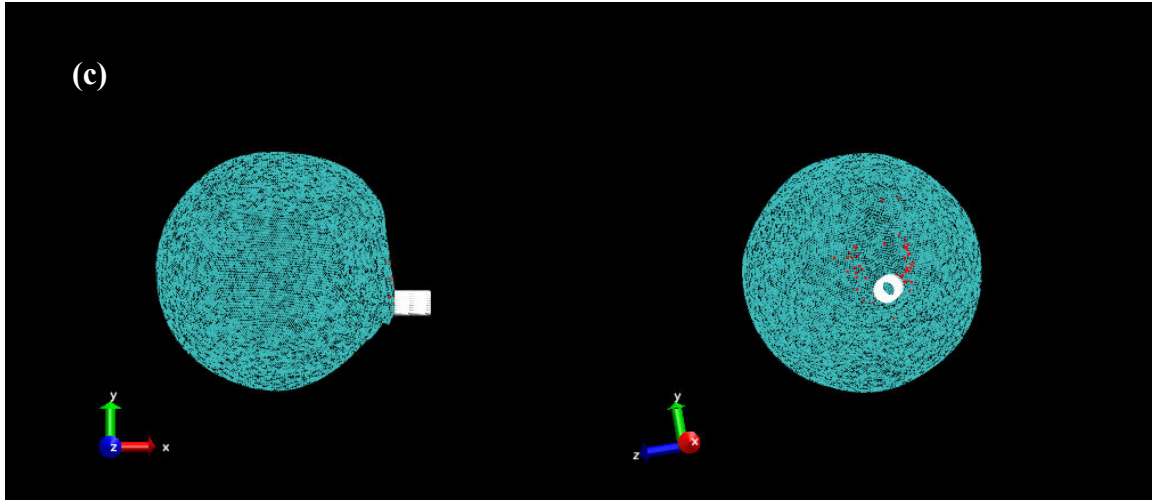
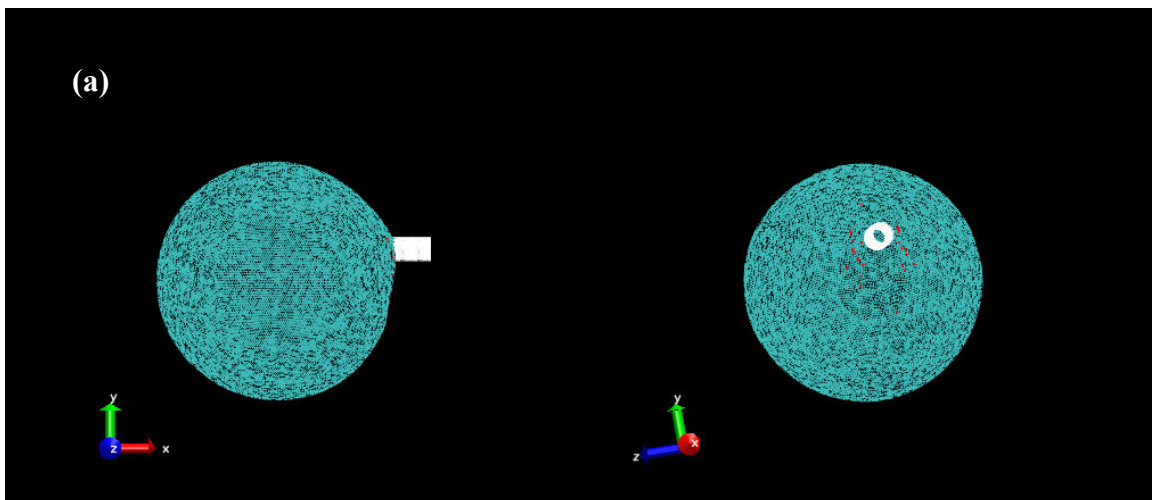


Figure 5.20 Deformation shapes of the oocyte at different times ($5\text{ }\mu\text{m}$ cell size and decohesion model): (a) $t=28\text{ }\mu\text{s}$, (b) $t=52\text{ }\mu\text{s}$, (c) $t=76\text{ }\mu\text{s}$, (d) $t=100\text{ }\mu\text{s}$



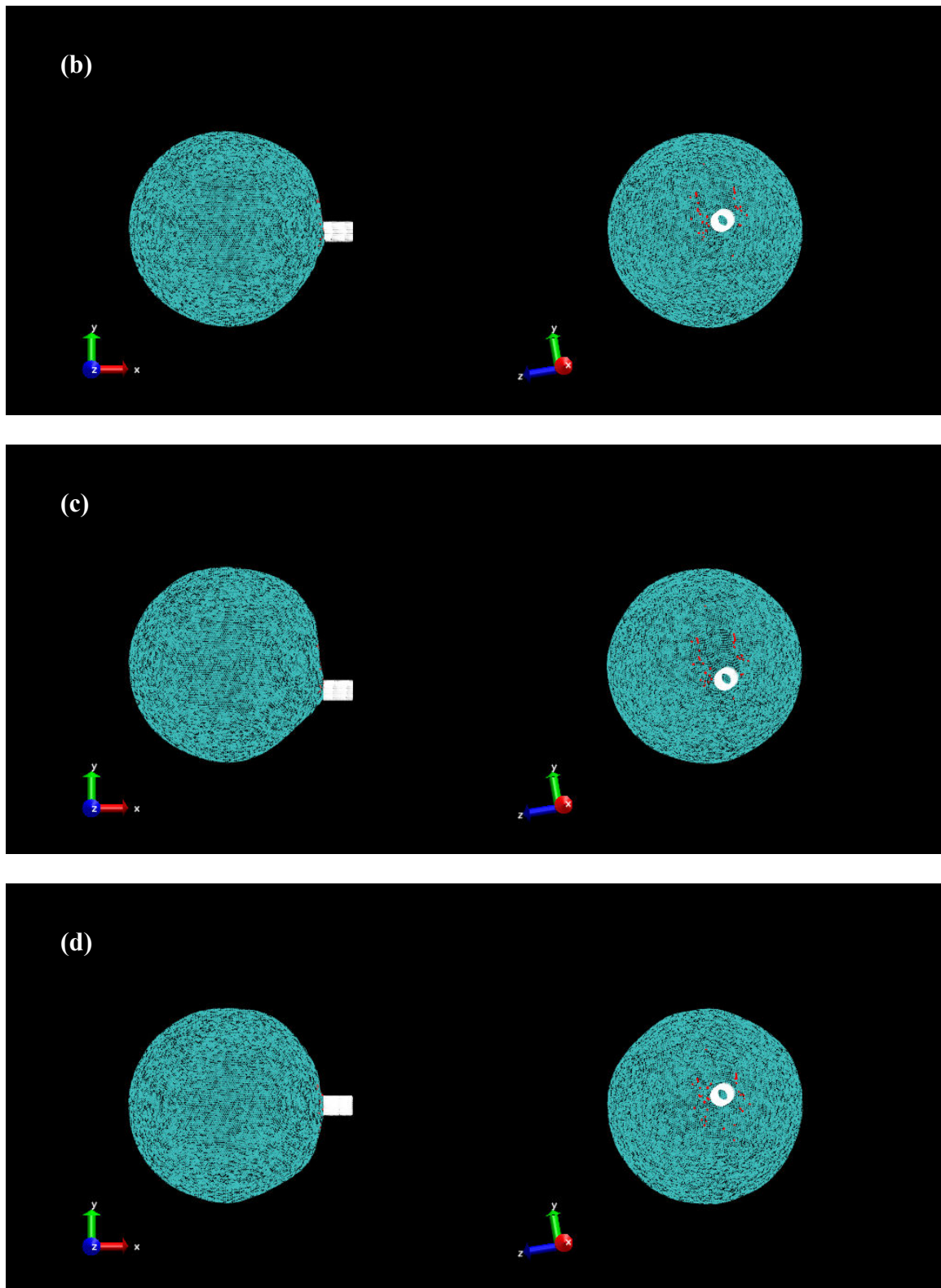
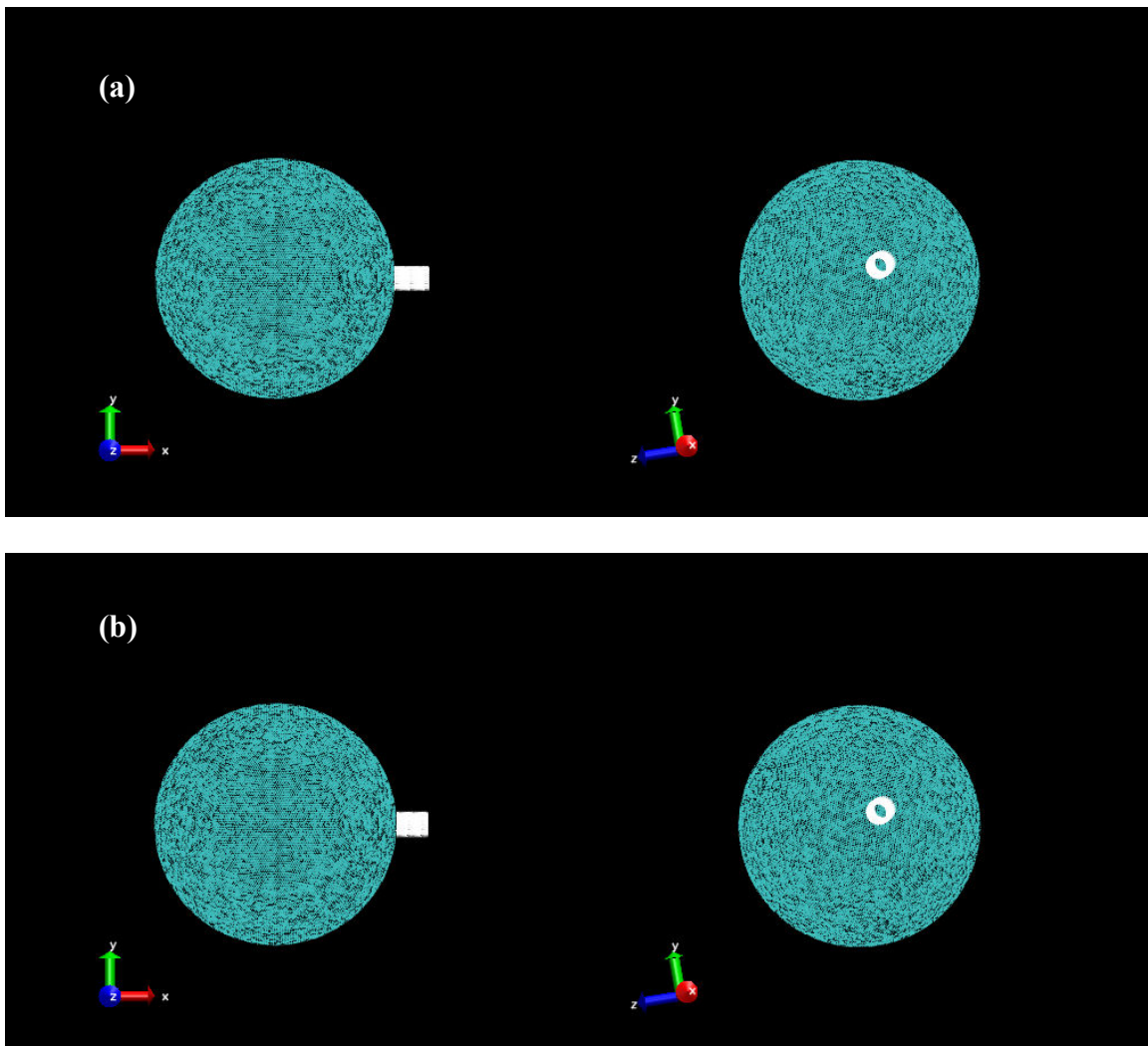


Figure 5.21 Deformation shapes of the oocyte at different times ($4\text{ }\mu\text{m}$ cell size and decohesion model): (a) $t=28\text{ }\mu\text{s}$, (b) $t=52\text{ }\mu\text{s}$, (c) $t=76\text{ }\mu\text{s}$, (d) $t=100\text{ }\mu\text{s}$

In the second category of the MPM simulations, the injection pipette has the longitudinal displacement only. Due to its high rigidity in the axial direction, the axial vibration of the injection pipette can be neglected. Therefore, the displacement of the injection pipette tip is the same as that of the pipette holder because the pipette is always firmly attached to the holder during the piezo-ICSI procedure. Since the axial displacement of the injection pipette results from the extension of the piezo crystal due to the voltage, the longitudinal displacement of the pipette takes the same triangular pulse form as the voltage and the duration time is $60\text{ }\mu\text{s}$ as well. The response of the mouse oocyte corresponding to an individual pulse is studied because the pulse duration is considerably smaller than the time between two consecutive piezo pulses. The experiment has shown that the axial displacement of the pipette holder is up to $0.08\text{ }\mu\text{m}$ for the 10-V voltage amplitude. It is obvious that an axial displacement of $0.08\text{ }\mu\text{m}$ is not enough to pierce the mouse zona. It is noticed that the pulse amplitude ranges from 0 to 100 V (<http://documents.exfo.com/specsheets/PiezoDrillan.pdf>). Therefore, to investigate the possibility of the zona piercing due to the axial movement of the injection pipette, the axial displacement amplitude of the pipette in the MPM simulations is set to be $1.8\text{ }\mu\text{m}$ (22.5 times of $0.08\text{ }\mu\text{m}$) instead. The mesh cell size of $4\text{ }\mu\text{m}$ is employed only and the time step is $5.0\times 10^{-10}\text{ s}$. Both the elastodamage and decohesion models have been employed for the mouse zona pellucida. The setup of the MPM model and all material parameters are the same as those for the case of $4\text{ }\mu\text{m}$ mesh size in the first category of MPM simulations. The deformation shapes of the oocyte corresponding to the elastodamage model and the decohesion model are given in Figures 5.22 and 5.23, respectively. It can be found that the oocyte has no evident deformation except for one

dent on the mouse zona surface due to the axial displacement of the pipette. This may be explained by the fast movement of the pipette and the small pipette diameter with respect to the oocyte size. Moreover, no failure membrane points are observed from the simulation results. This outcome disconfirms the argument that the puncture of the mouse zona pellucida in piezo-ICSI is caused by the axial displacement of the injection micropipette.



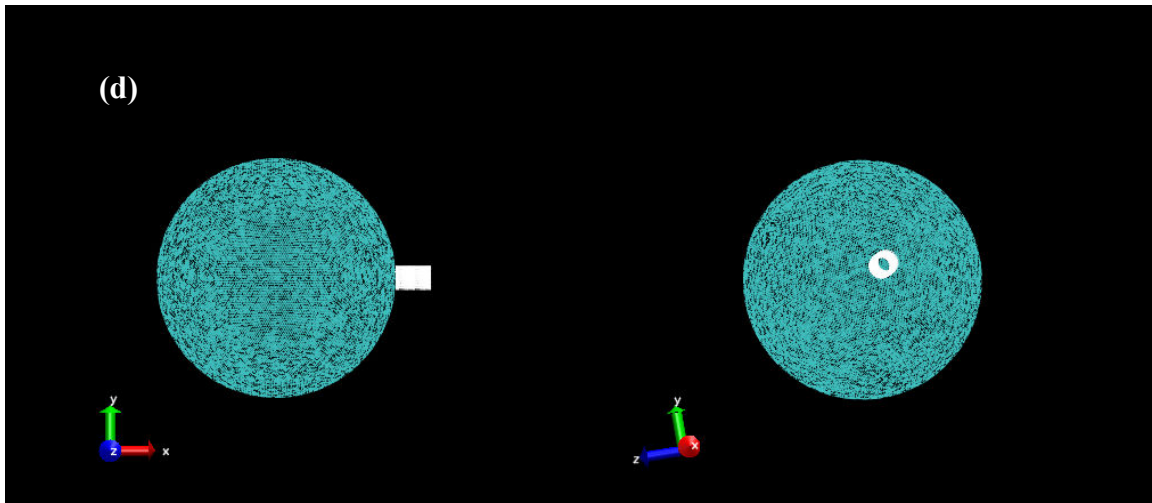
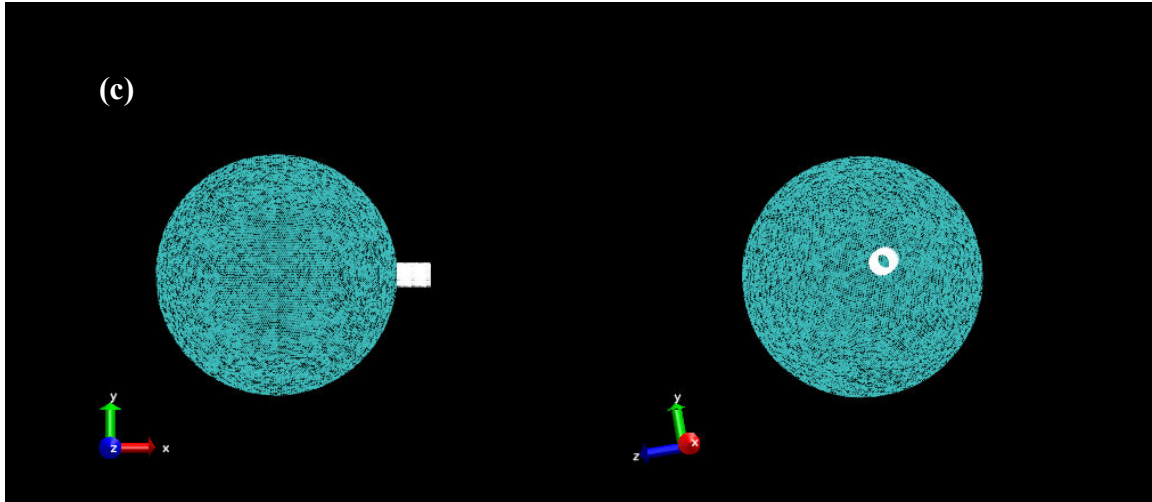
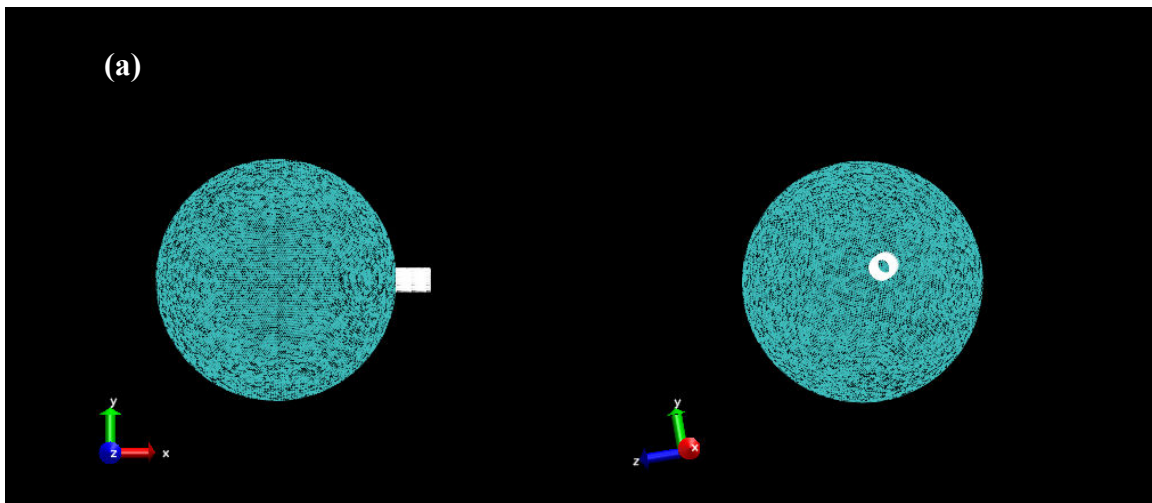


Figure 5.22 Deformation shapes of the oocyte at different times ($4\text{ }\mu\text{m}$ cell size and elastodamage model): (a) $t=15\text{ }\mu\text{s}$, (b) $t=30\text{ }\mu\text{s}$, (c) $t=45\text{ }\mu\text{s}$, (d) $t=60\text{ }\mu\text{s}$



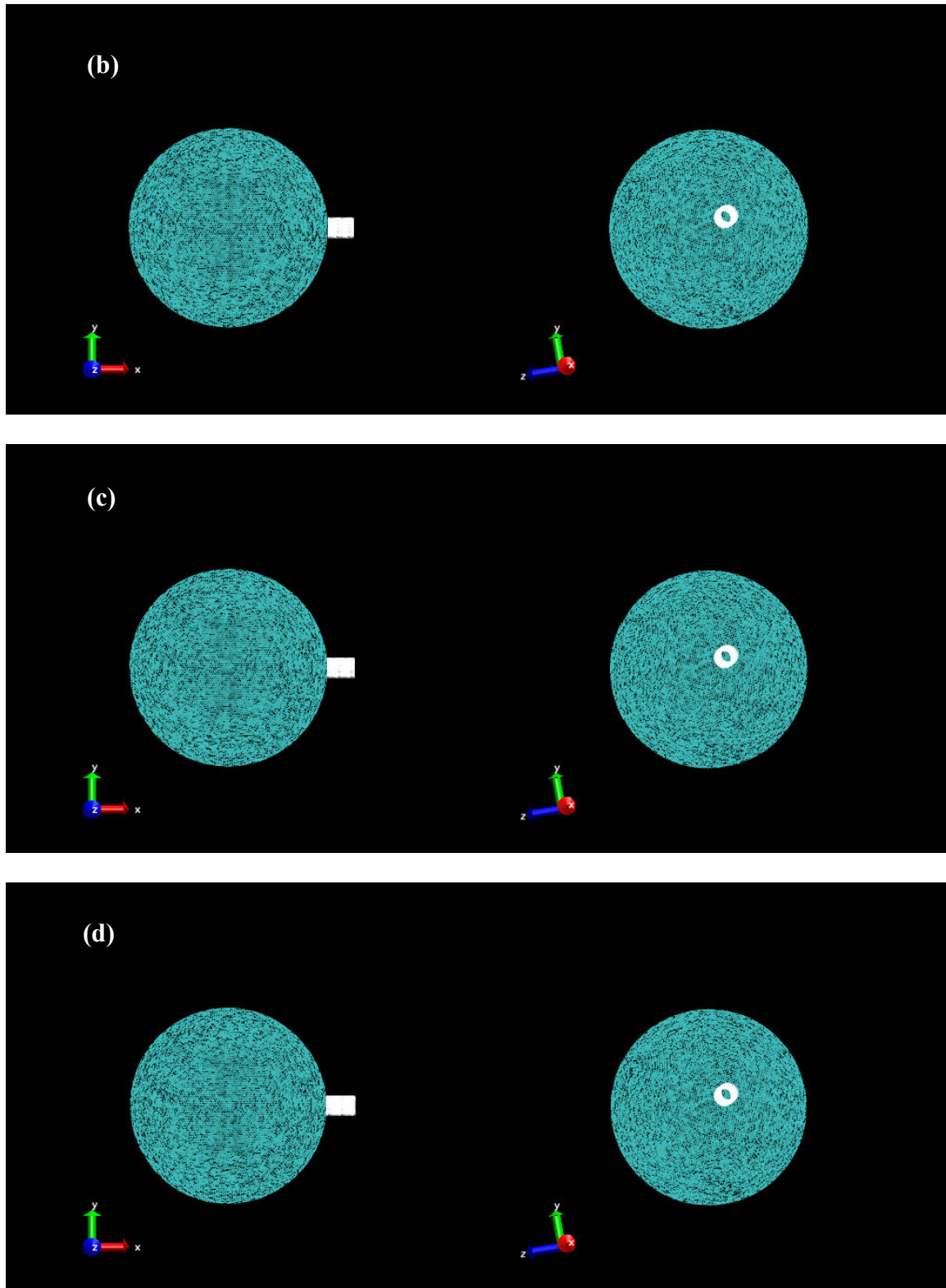


Figure 5.23 Deformation shapes of the oocyte at different times ($4 \mu\text{m}$ cell size and decohesion model): (a) $t=15 \mu\text{s}$, (b) $t=30 \mu\text{s}$, (c) $t=45 \mu\text{s}$, (d) $t=60 \mu\text{s}$

5.5 Role of Mercury in the Piercing Process

As demonstrated by the MPM simulations and experiments, the lateral vibration of the injection micropipette instead of the axial oscillation is a crucial factor for the mouse zona piercing in the piezo-ICSI. The study on the role of mercury in the piercing process, therefore, is focused on the effect of mercury on the lateral vibration of the pipette. For the purpose of simplicity, the vibration of the pipette in the air is analyzed using the FEM in this work. The injection micropipette is fabricated by pulling a glass capillary tube with a diameter of 1 mm. As compared with the pipette with an outer diameter of 10 μm , the capillary is very rigid. The injection micropipette, thus, could be modeled as a cantilever beam subject to the lateral translation at the fixed end, as sketched in Figure 5.24. The Euler-Bernoulli beam theory is used for the model because the height and deflection of the pipette are much smaller than its length. In addition, no plasticity would occur in the pipette due to the high strength of the glass.

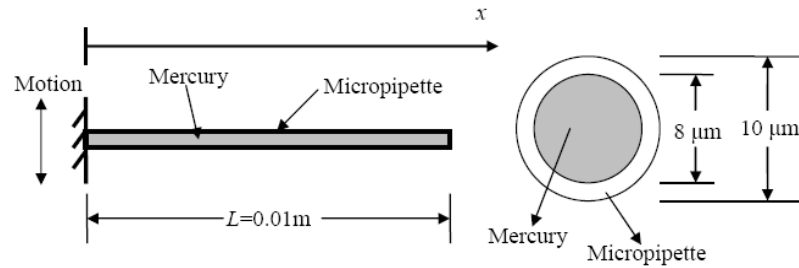


Figure 5.24 Cantilever beam model of the injection micropipette

The governing equation for the transverse vibration of the beam is expressed as (Weaver et al., 1990)

$$EI \frac{\partial^4 v(x,t)}{\partial x^4} + \bar{\rho} \frac{\partial^2 v(x,t)}{\partial t^2} = \bar{f}(x,t) \quad (5.57)$$

where EI is the flexural rigidity of the beam, $\bar{\rho}$ is the mass per unit length of the beam, v is the transverse deflection of the beam and \bar{f} is the transverse force applied to the beam.

Let us consider the free vibration of the beam. Then, Equation (5.57) becomes

$$EI \frac{\partial^4 v(x,t)}{\partial x^4} + \bar{\rho} \frac{\partial^2 v(x,t)}{\partial t^2} = 0 \quad (5.58)$$

The boundary conditions for the cantilever beam in Figure 5.24 are

$$v(0,t) = 0 \quad (5.59)$$

$$\left. \frac{\partial v}{\partial x} \right|_{x=0} = 0 \quad (5.60)$$

$$\left. \frac{\partial^2 v}{\partial x^2} \right|_{x=L} = 0 \quad (5.61)$$

$$\left. \frac{\partial^3 v}{\partial x^3} \right|_{x=L} = 0 \quad (5.62)$$

The free vibration of the cantilever beam is considered first by the method of separation of variables (Weaver et al., 1990; Asmar, 2000). With $v(x,t) = V(x)T(t)$, Equation (5.58) becomes

$$\frac{V^{(4)}}{V} = -\frac{T''}{\bar{c}^2 T} = \alpha^4 \quad (5.63)$$

where $\bar{c}^2 = EI/\bar{\rho}$, and α is a positive constant. The boundary problem for $V(x)$ is written as

$$V^{(4)} - \alpha^4 V = 0 \quad (5.64)$$

$$V(0) = 0 \quad (5.65)$$

$$V'(0) = 0 \quad (5.66)$$

$$V''(L) = 0 \quad (5.67)$$

$$V'''(L) = 0 \quad (5.68)$$

The solution of this problem is

$$V(x) = C_1(\cos \alpha x + \cosh \alpha x) + C_2(\cos \alpha x - \cosh \alpha x) \\ + C_3(\sin \alpha x + \sinh \alpha x) + C_4(\sin \alpha x - \sinh \alpha x) \quad (5.69)$$

The application of boundary conditions, Equations (5.65) and (5.66), to $V(x)$ gives

$C_1 = C_3 = 0$. From Equations (5.67) and (5.68), it can be found that

$$\cosh \alpha L \cos \alpha L = -1 \quad (5.70)$$

The n th positive root of Equation (5.70) is denoted by α_n . Then, the corresponding solution to T is

$$T_n = A_n \cos \alpha_n^2 ct + A_n^* \sin \alpha_n^2 ct \quad (5.71)$$

where A_n and A_n^* are coefficients determined by initial conditions. Therefore, the circular frequency of vibration of the n th mode is

$$\omega_n = \alpha_n^2 c = \alpha_n^2 \sqrt{\frac{EI}{\bar{\rho}}} \quad (5.72)$$

For the mercury-filled injection pipette shown in Figure 5.24, its physical parameters and first six natural frequencies are listed in Tables 5.5 and 5.6, respectively.

Table 5.5 Physical parameters of the mercury-filled injection pipette

EI (Pa·m ⁴)	$\bar{\rho}$ (kg/m ³)
183.86×10^{-13}	7.486×10^{-7}

Table 5.6 The first six natural frequencies of the mercury-filled injection pipette

n	1	2	3	4	5	6
$f_n = \frac{\omega_n}{2\pi}$	27.729	173.791	486.666	953.692	1576.353	2354.919

In the piezo-ICSI procedure, the transverse vibration of the injection micropipette is caused by the support motion rather than the external forces. Weaver et al. (1990) studied the vibration of beams subjected to support motions and formulated the beam response. Let us consider one simply-supported beam subjected to transverse motions at both ends. The absolute deflection of the beam is divided into two parts: the relative deflection and the translational deflection, i.e.,

$$v(x, t) = v^*(x, t) + v_g(x, t) \quad (5.73)$$

where $v(x, t)$ and $v^*(x, t)$ are the absolute deflection and the relative deflection, respectively, and $v_g(x, t)$ is the translational deflection. By using the Duhamel's integral and the superposition principle, the relative response of the beam could be given as

$$v^*(x, t) = -\sum_{i=1}^{\infty} \frac{1}{\omega_i} \sin \frac{i\pi x}{l} \left[\int_0^L \left(1 - \frac{x}{l}\right) \sin \frac{i\pi x}{l} dx \int_0^t \ddot{g}_1(t') \sin \omega_i(t - t') dt' \right. \\ \left. + \int_0^L \frac{x}{l} \sin \frac{i\pi x}{l} dx \int_0^t \ddot{g}_2(t') \sin \omega_i(t - t') dt' \right] \quad (5.74)$$

where $g_1(t)$ and $g_2(t)$ respectively denote the motions at the left and right ends of the beam, and l is the length of the beam. The translational deflection $v_g(x, t)$ is computed by

$$v_g(x, t) = \left(1 - \frac{x}{l}\right) g_1(t) + \frac{x}{l} g_2(t) \quad (5.75)$$

With Equations (5.73)-(5.75), the total response of a simply-supported beam as illustrated in Figure 5.25 is investigated. The beam has the same dimensions and configuration as the injection pipette shown in Figure 5.24. The transverse support motion $g_1(t)$ takes the form of $A \sin(\bar{\omega}t)$ with A being $10 \mu\text{m}$ and $g_2(t)$ is zero. Three values of $\bar{\omega}$, 5200, 52000 and 208000 are considered. The time-histories of the deflection at the beam center obtained by Equations (5.73)-(5.75) are presented in Figure 5.26. It can be found that the deflection amplitude becomes large as the frequency of the support motion increases. When $\bar{\omega}=208000$, the maximum deflection is 26% of the beam length and the problem should be nonlinear, which clearly contradicts with the real physics. As $\bar{\omega}$ becomes large, the vibration modes with higher frequencies will be excited and the response of the beam should accordingly become smaller. In fact, the derivation of Equations (5.73)-(5.75) does not consider the wave propagation in the beam and assumes the wave originated from one end travels to the other end instantaneously. However, with the increase of $\bar{\omega}$, the effect of the wave propagation on the beam vibration becomes more pronounced and can not be neglected. Therefore, the method proposed by Weaver et al. (1990) does not hold for the vibration analysis of the injection pipette in the piezo-ICSI procedure because of the short duration of the piezo pulse.

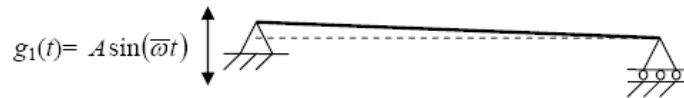


Figure 5.25 One simply-supported beam subjected to support motion at its left end

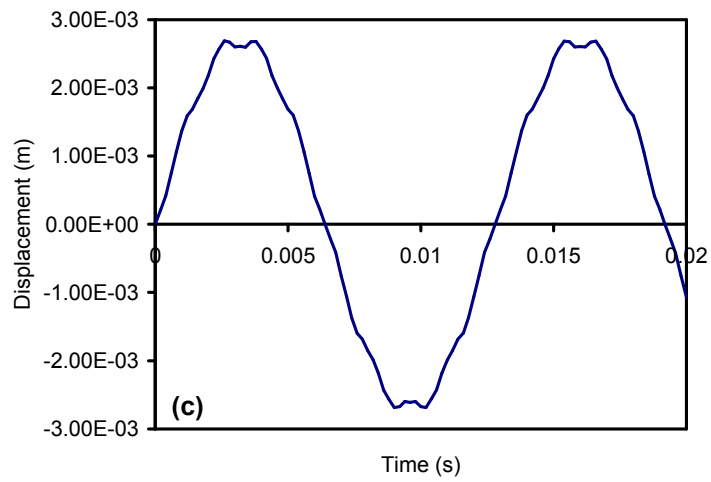
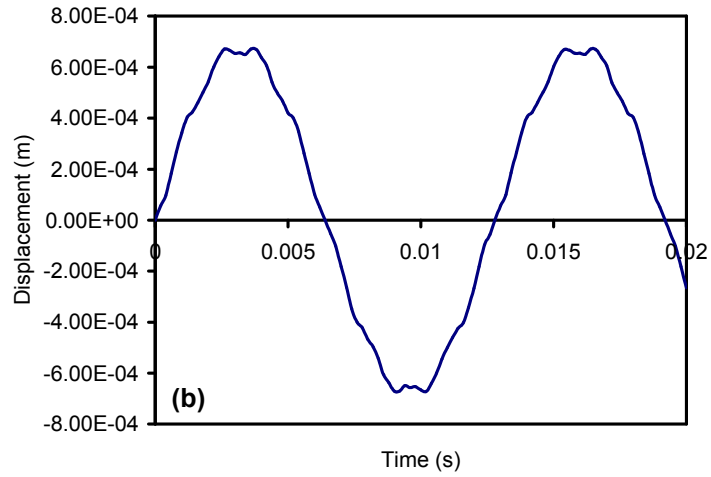
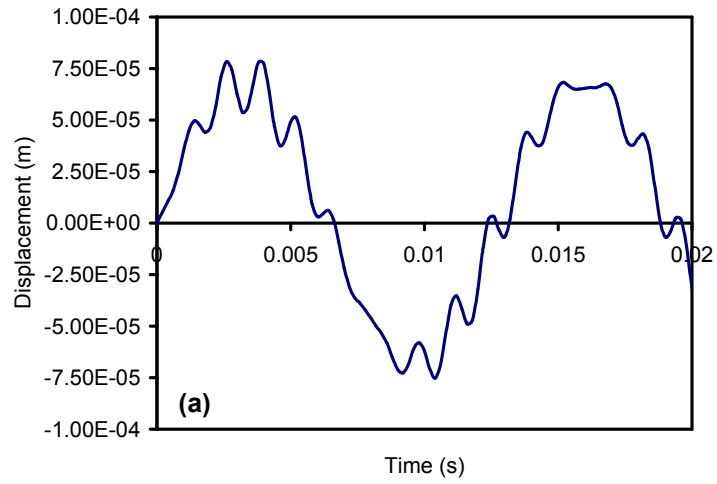


Figure 5.26 Time-history of the deflection at the beam center: (a) $\bar{\omega} = 5200$, (b) $\bar{\omega} = 52000$, (c) $\bar{\omega} = 208000$

The response of the injection micropipette is investigated with the FEM code, ANSYS. Since the fundamental goal is to find the role of mercury in the piercing process, a pipette without liquid inside and pipettes filled with mercury, fluorinert and water are considered. The densities of the fluids are listed in Table 5.7. According to the piezo-drill specifications (<http://documents.exfo.com/specsheets/PiezoDrillan.pdf>), the piezo pulse has a duration range between 60 and 600 μs and is applied at a frequency between 1 and 100 Hz. As compared with the time between two adjacent pulses, the pierce process and the pulse duration are extremely short. Furthermore, the repetition frequency of the piezo pulse is much lower than the natural frequency of the pipette. Thus, the transient response of the pipette under a single pulse is studied. The support motion is represented as one triangular pulse illustrated in Figure 5.27. To further investigate the effect of duration on the vibration of the pipette, the pulse duration varies from 60 to 600 μs with an increment of 60 μs . The pipette is discretized with twenty beam elements. The total simulation time is 5 ms and the time step is 0.6 μs . The dimensionless amplitudes of the pipette tips are presented in Figure 5.28, in which the dimensionless amplitude is defined as the ratio of the amplitude to the peak support displacement.

It is demonstrated from Figure 5.28 that the employment of fluids generally results in smaller amplitude of the pipette tip, and the amplitude of the pipette tip decreases with the increase of the fluid density. Ediz and Olgac (2005) also found that the lateral amplitude of the mercury-filled pipette tip is considerably smaller as compared with that of the pipette without mercury. The role of mercury seems to reduce the damage to the oocyte and accordingly improve the success rate of the piezo-ICSI procedure. As the duration of the piezo pulse becomes shorter, smaller amplitude of the pipette tip is

generally observed. Thus, an alternative piezo-ICSI procedure with no mercury is possible by properly choosing a nontoxic substitute for mercury, the dimensions of the injection pipette and the piezo-drill controller parameters as well.

Table 5.7 Densities of fluids

Mercury (kg/m ³)	Fluorinert (kg/m ³)	Water (kg/m ³)
13600	1780	1000

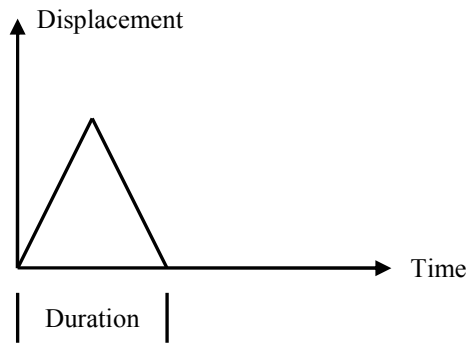


Figure 5.27 The triangular support motion

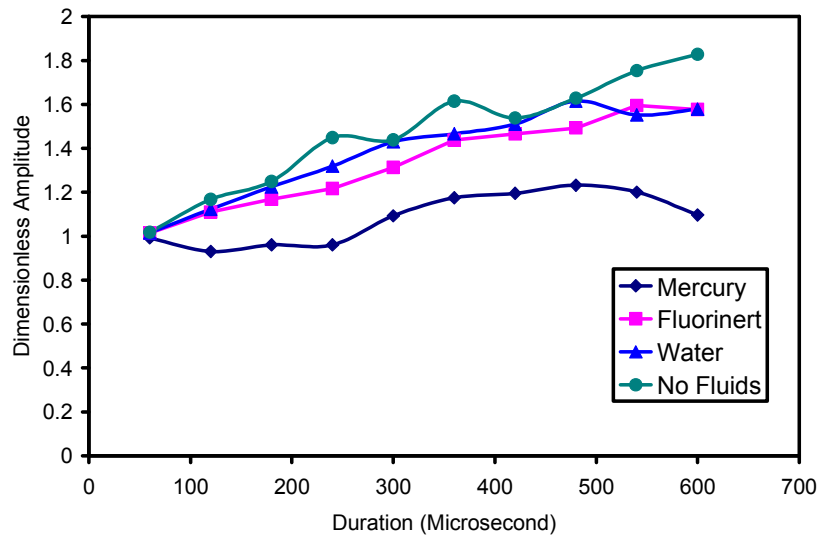


Figure 5.28 The amplitude of the pipette tip

5.6 Summary

The effects of the axial and lateral displacements of the injection pipette on the mouse zona piercing process in piezo-ICSI are studied with the MPM simulations, where the isotropic elastodamage and the discontinuous decohesion constitutive equations are employed for the mouse zona pellucida. It is demonstrated that the puncture of the mouse zona is primarily due to the lateral vibration rather than the axial one. Then, the lateral transient response of the injection pipette is analyzed with the FEM to investigate the role of mercury in the piercing process. The employment of a mercury-filled injection micropipette is found to be able to reduce the amplitude of the pipette tip, which might lead to less damage to the oocyte and hence yield higher fertilization and pregnancy rates of the oocyte after piezo-ICSI. It is also discovered that the amplitude is reduced as the duration of the piezo pulse gets short. Therefore, the development of a piezo-ICSI procedure without using mercury is possible by changing the dynamic characteristics of the injection micropipette and the piezo-drill controller parameters.

CHAPTER 6

CONCLUDING REMARKS AND FUTURE WORK

6.1 Summary

The piezo-ICSI method has become a popular and important microinjection technique for assisted fertilization. In the piezo-ICSI procedure, a mercury-filled injection micropipette is commonly used for a higher success rate. The usage of mercury, however, should be restricted due to its toxicity. The development of an alternative piezo-ICSI procedure without using mercury is desired, for which the role of mercury in the piercing process must be understood. So far, there is no agreement on the explanations for the physics of the zona piercing in piezo-ICSI. To the author's knowledge, no simulation work has been done to model this piercing process. Therefore, the major goal of this dissertation is to find out the response of the oocyte to the piezo pulses and the role of mercury in the piercing process by performing model-based simulations.

In order to model the piercing process in piezo-ICSI, an effort has been made to formulate a three-dimensional MPM model for fluid-membrane interaction. By applying the plane stress assumption in the local tangent plane, the original MPM algorithm is modified to simulate the thin membrane structure. An iterative algorithm is designed to compute the stresses at fluid points with the use of the relation between stress and rate of strain, the conservation equations of mass and energy as well as the equation of state for the fluid. The interaction between the fluid and the membrane is indirectly coupled via

the Eulerian grid nodes without any consideration of the fluid-membrane interface. Thus, no modification to the original MPM algorithm is needed for the treatment of fluid-membrane interaction. To find the physics of the zona piercing in piezo-ICSI, the proposed MPM model has been employed to simulate the mouse zona piercing process involving the oocyte, micropipette tip as well as fluids inside and outside the egg. Finally, the role of mercury played in the transient response of the injection pipette is analyzed with the FEM.

6.2 Findings and Conclusions

The model-based simulations of the zona piercing process have been performed with the MPM for an understanding of the piercing mechanism in piezo-ICSI. The MPM simulations are divided into two categories: one is to study the response of the oocyte to the lateral vibration of the pipette, and the other is to investigate the effect of the longitudinal oscillation of the pipette on the piercing process. It is observed from the simulations that the lateral vibration of the injection micropipette results in the noticeable oocyte deformation and the occurrence of the zona failure. On the contrary, no evident deformation and zona failure have been observed from the simulations with the longitudinal oscillation of the pipette only. The failure pattern of the mouse zona pellucida is found to be dependent on its constitutive model. With the use of the elastodamage model, failure points are concentrated at four corner areas around the contact area between the pipette tip and the zona. For the decohesion model, failure points are evenly distributed in narrow areas oriented along the vibration direction of the pipette. In addition, the comparison among the MPM simulations with different

computational cell sizes indicates that the elastodamage model is mesh-dependent whereas the decohesion model is independent of the cell size.

To further find out the effect of mercury on the zona piercing, the lateral vibration of an injection pipette without fluids inside and pipettes filled with mercury, fluorinert and water has been analyzed using the FEM, in which the pipette is modeled as a cantilever beam subject to the pulse support motion. It is found that the employment of fluids generally reduces the amplitude of the pipette tip and the amplitude decreases with the increase of the fluid density. Moreover, smaller vibration amplitude is in general observed when the piezo pulse with a shorter duration time is applied.

Based on the work presented in this dissertation, the following conclusions can be drawn:

(1) It is disconfirmed that the puncture of the mouse zona pellucida in piezo-ICSI is mainly due to the axial displacement of the pipette.

(2) The lateral vibration of the injection pipette plays a key role in the zona piercing process of piezo-ICSI, which is consistent with the experimental observation.

(3) The effect of mercury in piezo-ICSI might lie in causing less oocyte damage due to the reduced amplitude of the pipette tip, thereby improving the success rate of the piezo-ICSI procedure.

(4) The development of a piezo-ICSI procedure without using mercury is possible by changing the dynamic characteristics of the injection micropipette and the piezo-drill controller parameters, such as properly choosing a nontoxic substitute for mercury, adjusting the dimensions of the micropipette and decreasing the duration of the piezo pulse, etc.

6.3 Future Work

The presented MPM results have disproved the argument that the axial displacement of the pipette pierces the zona and strengthened the importance of the lateral vibration of the injection micropipette in the piercing process of piezo-ICSI. Due to the absence of the well-formulated constitutive model for the mouse zona, the exact oocyte behavior in piezo-ICSI can not be given in this study. Both experiments and molecular-level simulations, thus, are proposed to formulate a reasonable constitutive model for the oocyte zona. During the FEM vibration analysis of the injection micropipette, the pipette is modeled as one cantilever beam with the pipette shoulder being the fixed end. The unknown relation between the piezo-drill controller parameters and the shoulder motions obstructs the further study for the scientific guidance of the pulse parameter adjustment in piezo-ICSI. Hence, a well-designed experiment is required to obtain a clear relation between the piezo forces and the shoulder displacements. In addition, to better simulate the piercing process in the piezo-ICSI procedure, the MPM and the FEM might be coupled so that the whole immersed pipette tips, the oocyte and the medium could be modeled in a single computational domain with less computational cost. In this dissertation, all simulations are performed at the continuum-level without the consideration of any molecular details. The future research on the molecular-level response of the oocyte in the piezo-ICSI would provide a deep insight of the oocyte damage due to the piezo forces, and thus help improving the piezo-ICSI procedure for the reduction of the cellular damage.

REFERENCES

- Aboulghar, M.A., Mansour, R.T., Serour, G.I., Sattar, M.A. and Amin, Y.M. (1996) "Intracytoplasmic sperm injection and conventional in vitro fertilization for sibling oocytes in cases of unexplained infertility and borderline semen". *Journal of Assisted Reproduction and Genetics*, **13**, 38-42.
- Anghileri, M., Castelletti, L.-M.L. and Tirelli, M. (2005) "Fluid-structure interaction of water filled tanks during the impact with the ground". *International Journal of Impact Engineering*, **31**, 235-254.
- Antoci, C., Gallati, M. and Sibilla, S. (2007) "Numerical simulation of fluid-structure interaction by SPH". *Computers and Structures*, **85**, 879-890.
- Asmar, N. (2000) "Partial differential equations and boundary value problems". Prentice-Hall, New Jersey.
- Bagchi, P., Johnson, P.C. and Popel, A.S. (2005) "Computational fluid dynamics simulation of aggregation of deformable cells in a shear flow". *Journal of Biomechanical Engineering*, **127**, 1070-1080.
- Bilodeau, G.G. (1992) "Regular pyramid punch problem". *Journal of Applied Mechanics*, **59**, 519-523.
- Boey, S.K., Boal, D.H. and Discher, D.E. (1998) "Simulations of the erythrocyte cytoskeleton at large deformation. I. Microscopic Models". *Biophysical Journal*, **75**, 1573-1583.
- Bonet, J. and Kulasegaram, S. (2000) "Correction and stabilization of smoothed particle hydrodynamics method with applications in metal forming simulations". *International Journal for Numerical Methods in Engineering*, **47**, 1189-1214.
- Bozic, B., Svetina, S. and Zeks, B. (1997) "Theoretical analysis of the formation of membrane microtubes on axially strained vesicles". *Physical Review E*, **55**, 5834-5842.
- Brackbill, J.U. (1987) "On modeling angular momentum and vorticity in compressible fluid flow". *Computer Physics Communications*, **47**, 1-16.
- Brackbill, J.U. (1988) "The ringing instability in particle-in-cell calculations of low speed flow". *Journal of Computational Physics*, **75**, 469-492.

- Brackbill, J.U. (1991) "FLIP-MHD: A particle-in-cell method for magneto-hydrodynamics". *Journal of Computational Physics*, **96**, 163-192.
- Brackbill, J.U. and Ruppel, H.M. (1986) "FLIP: a method for adaptively zoned, particle-in-cell calculations of fluid flows in two dimensions". *Journal of Computational Physics*, **65**, 314-343.
- Buijk, A.J. and Low, T.C. (1993) "Significance of gas dynamics in airbag simulations" In: *The 26th ISATA, Aachen, Germany*.
- Buijk, A.J., and Florie, C.J.L. (1991) "Inflation of folded driver and passenger airbags". In: *The 1991 MSC World Users Conference, Los Angeles, California*.
- Caille, N., Thoumine, O., Tardy, Y. and Meister, J.-J. (2002) "Contribution of the nucleus to the mechanical properties of endothelial cells". *Journal of Biomechanics*, **35**, 177-187.
- Chang, M.C. (1959) "Fertilization of rabbit ova in vitro". *Nature*, **184**, 466-467.
- Chen, B.M. and Grinnell, A.D. (1997) "Kinetics, Ca^{2+} dependence, and biophysical properties of integrin-mediated mechanical modulation of transmitter release from frog motor nerve terminals". *Journal of Neuroscience*, **17**, 904-916.
- Chen, J.K., Beraun, J.E. and Carney, T.C. (1999) "A corrective smoothed particle method for boundary value problems in heat conduction". *Computer Methods in Applied Mechanics and Engineering*, **46**, 231-252.
- Chen, Z. (1996) "Continuous and discontinuous failure modes". *Journal of Engineering Mechanics*, **122**, 80-82.
- Chen, Z. and Fang, H.E. (2001) "A study on the link between coupled plasticity/damage and decohesion for multi-Scale modeling". *Journal of Mechanical Engineering Science - Proceedings of the Institution of Mechanical Engineers Part C*, **215**, 259-263.
- Chen, Z. and Schreyer, H.L. (1995) "Formulation and computational aspects of plasticity and damage models with application to quasi-brittle materials". Sandia National Laboratories Report, SAND95-0329.
- Chen, Z., Qian, D. and Xin, X. (1999) "A study of localization problems based on the transition between governing equations". *International Journal of Advances in Structural Engineering*, **2**, 289-304.
- Chen, Z., Shen, L., Mai, Y.-W. and Shen, Y.-G. (2005) "A bifurcation-based decohesion model for simulating the transition from localization to decohesion with the MPM". *Journal of Applied Mathematics and Physics (ZAMP)*, **56**, 908-930.

Cocchi, J.-P. and Saurel, R. (1997) “A Riemann problem based method for the resolution of compressible multimaterial flows”. *Journal of Computational Physics*, **137**, 265-298.

Coleman B.D. and Gurtin, M.E. (1967) “Thermodynamics with internal state Variables”. *Journal of Chemical Physics*, **47**, 597-613.

Coleman, B.D. and Noll, W. (1963) “The thermodynamics of elastic materials with heat conduction and viscosity”. *Archives of Rational Mechanical Analysis*, **13**, 167-178.

Cooper, K., Ohler, N., Gupta, A. and Beaudoin, S. (2000) “Analysis of contact interactions between a rough deformable colloid and a smooth substrate”. *Journal of Colloid and Interface Science*, **222**, 63-74.

Coughlin, M.F. and Stamenovic, D. (2003) “A Prestressed Cable Network Model of the Adherent Cell Cytoskeleton”. *Biophysical Journal*, **84**, 1328-1336.

Dawson, J.M. (1983) “Particle simulation of plasmas”. *Reviews of Modern Physics*, **55**, 403-447.

Derjaguin, B.V., Muller, V.M. and Toporov, Y.P. (1975) “Effect of contact deformations on the adhesion of particles”. *Journal of Colloid and Interface Science*, **53**, 314-326.

Dike, L., Chen, C.S., Mrkisch, M., Tien, J., Whitesides, G.M. and Ingber, D.E. (1999) “Geometric control of switching between growth, apoptosis, and differentiation during angiogenesis using micropatterned substrates”. *In Vitro Cellular & Developmental Biology-Animal*, **35**, 441-448.

Domke, J., Dannöhl, S., Parak, W.J., Müller, O., Aicher, W.K. and Radmacher, M. (2000) “Substrate dependent differences in morphology and elasticity of living osteoblasts investigated by atomic force microscopy”. *Colloids and Surfaces B: Biointerfaces*, **19**, 367-379.

Donea, J. (1983) “Arbitrary Lagrangian-Eulerian Finite Element Methods”. In: *Computational Methods for Transient Analysis*, Elsevier, Amsterdam, 473-516.

Donea, J., Fasoli-Stella, P. and Giuliani, S. (1977), “Lagrangian and Eulerian Finite Element Techniques for Transient Fluid-Structure Interaction Problems”. In: *Transactions of the 4th International Congress on Structural Mechanics in Reactor Technology*, **B**, San Francisco, California.

Dong, C. and Skalak, R. (1992) “Leukocyte deformability: finite element modeling of large viscoelastic deformation”. *Journal of Theoretical Biology*, **158**, 173-193.

Dong, C., Skalak, R. and Sung, K.L. (1991) “Cytoplasmic rheology of passive neutrophils”. *Biorheology*, **28**, 557-567.

- Dong, C., Skalak, R., Sung, K.L., Schmid-Schonbein, G.W. and Chien, S. (1988) "Passive deformation analysis of human leukocytes". *Journal of Biomechanical Engineering*, **110**, 27-36.
- Drury, J.L. and Dembo, M. (2001) "Aspiration of Human Neutrophils: Effects of Shear Thinning and Cortical Dissipation". *Biophysical Journal*, **81**, 3166-3177.
- Ediz, K. and Olgac, N. (2004) "Microdynamics of the piezo-driven pipettes in ICSI". *IEEE Transactions on Biomedical Engineering*, **51**, 1262-1268.
- Ediz, K. and Olgac, N. (2005) "Effect of mercury column on the microdynamics of the piezo-driven pipettes". *Journal of Biomechanical Engineering*, **127**, 531-535.
- Elson, E.L. (1988) "Cellular mechanics as an indicator of cytoskeletal structure and function". *Annual Review of Biophysics and Biophysical Chemistry*, **17**, 397-430.
- Evans, E. and Kukan, B. (1984) "Passive material behavior of granulocytes based on large deformation and recovery after deformation tests". *Blood*, **64**, 1028-1035.
- Evans, E.A. and Skalak, R. (1980) *Mechanics and Thermodynamics of Biomembranes*, Section 3.5, CRC Press, Boca Raton, Florida.
- Fabry, B., Maksym, G.N., Butler, J.P., Glogauer, M., Navajas, D., Taback, N.A., Millet, E.J. and Fredberg, J.J. (2003) "Time scale and other invariants of integrative mechanical behavior in living cells". *Physical Review E*, **68**, 041914.
- Florie, C.J.L, Buijk, A.J., Venis, A.C.J. and Luttwak, G. (1991) "Three-Dimensional fluid structure interaction applied in airbag and birdstrike analyses," In: the MSC European Users Conference, Munich, Germany.
- Folkman, J. and Moscona, A. (1978) "Role of cell shape in growth control". *Nature*, **273**, 345-349.
- Fuller, K.N.G. and Tabor, D. (1975) "The effect of surface roughness on the adhesion of elastic solids". *Proceedings of the Royal Society of London Series A*, **345**, 327-342.
- Gay, M., Zhang, L. and Liu, W.K. (2006) "Stent modeling using immersed finite element method". *Computer Methods in Applied Mechanics and Engineering*, **195**, 4358-4370.
- Gingold, R.A. and Monaghan, J.J. (1977) "Smoothed particle hydrodynamics: theory and application to non-spherical stars". *Monthly Notices of the Royal Astronomical Society*, **181**, 375-389.

Greenwood, J.A. (1997) "Adhesion of elastic spheres". Proceedings of the Royal Society of London Series A, **453**, 1277-1297.

Greenwood, J.A. and Johnson, K.L. (1981) "The mechanics of adhesion of viscoelastic solids". Philosophical Magazine A, **43**, 697-711.

Gross, M.B. and Hofmann, R., (1977) "Fluid-Structure interaction calculations". In: Transactions of the 4th International Congress on Structural Mechanics in Reactor Technology, **B**, San Francisco, California.

Guilak, F., Tedrow, J.R. and Burgkart, R. (2000) "Viscoelastic Properties of the Cell Nucleus". Biochemical and Biophysical Research Communications, **269**, 781-786.

Haller, K.K., Ventikos, Y. and Poulidakosa, D. "Computational study of high-speed liquid droplet impact". Journal of Applied Physics, **92**, 2821-2828.

Hallquist, J.O. (1998) "LS-DYNA Theoretical Manual". Livermore Software Technology Corporation, Livermore, California.

Harlow, F.H. (1964) "The particle-in-cell computing method for fluid dynamics". In: Methods in Computational Physics, **3**, 319-343.

Harlow, F.H. and Amsden, A.A. (1971) "Fluid Dynamics". Los Alamos Scientific Laboratory Report, LA-4700.

Hiramoto, Y. (1996) "Microinjection of the live spermatozoa into sea urchin eggs". Experimental Cell Research, **27**: 416-426.

Hirt, C.W., Amsden, A.A. and Cook, J.L. (1974) "An arbitrary Lagrangian-Eulerian computing method for all flow speeds". Journal of Computational Physics, **14**, 227-253.

Hosoi, Y., Miyake, M., Utsumi, K. and Iritani, A. (1988) "Development of rabbit oocytes after microinjection of spermatozoa". In: Proceedings of the 11th International Congress on Animal Reproduction and Artificial Insemination. Abstract 331.

Hu, H.H., Patankar, N.A. and Zhu, M.Y. (2001) "Direct numerical simulations of fluid-solid systems using the arbitrary Lagrangian-Eulerian technique". Journal of Computational Physics, **169**, 427-462.

Iglic, A. (1997) "A possible mechanism determining the stability of spiculated red blood cells". Journal of Biomechanics, **30**, 35-40.

Ingber, D.E. (1990) "Fibronectin controls capillary endothelial cell growth by modulating cell shape". Proceedings of the National Academy of Sciences, **87**, 3579-3583.

- Ingber, D.E. (1993) "Cellular tensegrity: defining new rules of biological design that govern the cytoskeleton". *Journal of Cell Science*, **104**, 613-627.
- Ingber, D.E. (2003a) "Tensegrity I: Cell structure and hierarchical systems biology". *Journal of Cell Science*, **116**, 1157-1173.
- Ingber, D.E. (2003b) "Tensegrity II: How structural networks influence cellular information processing networks" *Journal of Cell Science*, **116**, 1397-1408.
- Ingber, D.E. and Jamieson, J.D. (1982) "Tumor formation and malignant invasion: role of basal lamina". In: *Tumor Invasion and Metastasis*, The Hague, The Netherlands, 335-357.
- Ingber, D.E. and Jamieson, J.D. (1985) "Cells as tensegrity structures: architectural regulation of histodifferentiation by physical forces transduced over basement membrane". In: *Gene Expression During Normal and Malignant Differentiation*, Academic Press, Orlando, Florida, 13-32.
- Ingber, D.E., Madri, J.A. and Jamieson, J.D. (1986) "Basement membrane as a spatial organizer of polarized epithelia: exogenous basement membrane reorients pancreatic epithelial tumor cells in vitro". *American Journal of Pathology*, **122**, 129-139.
- Iordache, M.M. and William, K. (1998) "Localized failure analysis in elastoplastic cosserat continua". *Computer Methods in Applied Mechanics and Engineering*, **151**, 559-586.
- Iritani, A. (1989) "Micromanipulation of oocytes and embryos". In: *Proceedings of 13th World Congress on Fertility and Sterility*, Marrakech, Morocco, Parthenon Publishing, Carnforth, UK.
- Johnson, K.L. (1985) "Contact Mechanics". Cambridge University Press, Cambridge, Great Britain.
- Johnson, K.L., Kendall K. and Roberts A.D. (1971) "Surface energy and the contact of elastic solids". *Proceedings of the Royal Society of London Series A*, **324**, 301-313.
- Kalitzin, G., Iaccarino, G. and Khalighi, B. (2003) "Towards an immersed boundary solver for RANS simulations". *AIAA Paper*, 2003-0770.
- Kan, H.C., Udaykumar, H.S., Shyy, W. and Tran-Son-Tay, R. (1998) "Hydrodynamics of a compound drop with application to leukocyte modeling". *Physics of Fluids*, **10**, 760-774.
- Kawase, Y., Iwata, T., Toyoda, Y., Wakayama, T., Yanagimachi, R. and Suzuki, H. (2001) "Comparison of intracytoplasmic sperm injection for inbred and hybrid mice," *Molecular Reproduction and Development*, **60**, 74-78.

Kimura, Y. and Yanagimachi R. (1995) "Intracytoplasmic sperm injection in the mouse". *Biology of Reproduction*, **52**, 709-720.

Kimura, Y., Yanagimachi, R., Kuretake, S., Bortkiewicz, H., Perry, A.C.F. and Yanagimachi, H. (1998) "Analysis of mouse oocyte activation suggests the involvement of sperm perinuclear material," *Biology of Reproduction*, **58**, 1407-1415.

Kuropatenko, V.F. (1967) "On difference methods for the equations of hydrodynamics". In: *Difference Methods for Solutions of Problems of Mathematical Physics*, **1**, American Mathematical Society, Providence, Rhode Island.

Landshoff, R. (1955) "A numerical method for treating fluid flow in the presence of shocks". Los Alamos Scientific Laboratory Report LA-1930.

Lanzendorf, S., Maloney, M.K., Veeck, L.L., Slusser, J., Hodgen, G.D. and Rosenwaks, Z. (1988) "A preclinical evaluation of pronuclear formation by microinjection of human spermatozoa into human oocytes". *Fertility and Sterility*, **49**, 835-842.

Lardner T.J. and Pujara P. (1980) "Compression of spherical cells". In: *Mechanics Today*, **5**, 161-176.

Leboeuf, J.N., Tajima, T. and Dawson, J.M. (1979) "A magnetohydrodynamic particle code for fluid simulation of plasmas". *Journal of Computational Physics*, **31**, 379-408.

Li, M.L., Aggeler, J., Farson, D.A., Hatier, C., Hassell, J. and Bissell, M.J. (1987) "Influence of a reconstituted basement membrane and its components on casein gene expression and secretion in mouse mammary epithelial cells". *Proceedings of the National Academy of Sciences*, **84**, 136-140.

Lim, C.T., Zhou, E.H. and Quek, S.T. (2006) "Mechanical models for living cells-a review". *Journal of Biomechanics*, **39**, 195-216.

Liu, W.K and Ma, D.C. (1981) "Computer Implementation Aspects for Fluid-Structure Interaction Problems". *Computer Methods in Applied Mechanics and Engineering*, **31**, 129-148.

Liu, W.K., Liu, Y., Farrell, D., Zhang, L., Wang, S.X., Fukui, Y., Patankar, N., Zhang, Y., Bajaj, C., Lee, J., Hong, J., Chen, X. and Hsu, H. (2006) "Immersed finite element method and its applications to biological systems". *Computer Methods in Applied Mechanics and Engineering*, **195**, 1722-1749.

Liu, Y., Zhang, L., Wang, X. and Liu, W.K. (2004) "Coupling of Navier–Stokes equations with protein molecular dynamics and its application to hemodynamics". *International Journal for Numerical Methods in Fluids*, **46**, 1237-1252.

Lucy, L.B. (1977) "A numerical approach to the testing of the fission hypothesis". The Astronomical Journal, **82**, 1013-1024.

Lundin, K., Sjogren, A. and Hamberger, L. (1996) Reinsemination of one-day-old oocytes by use of intracytoplasmic sperm injection". Fertility and Sterility, **66**, 118-121.

Lyon, S.P. and Johnson, J.D. "SESAME: The Los Alamos National Laboratory Equation Of State Database". (1992) Los Alamos National Laboratory Report, LA-UR-92-3407.

Lysmer, J. and R.L. Kuhlemeyer (1969) "Finite dynamic model for infinite media". Journal of the Engineering Mechanics Division, ASCE, **95**, 859-877.

Mansour, R. (1998) "Intracytoplasmic sperm injection: a state of the art technique". Human Reproduction Update, **4**, 43-56.

Mansour, R.T., Aboulghar, M.A., Serour, G.I., Amin, Y.M. and Ramzi, A.M. (1995) "The effect of sperm parameters on the outcome of intracytoplasmic sperm injection". Fertility and Sterility, **64**, 982-986.

Markert, C.L. (1983) "Fertilization of mammalian eggs by sperm injection". Journal of Experimental Zoology, **228**, 195-201.

McCrory, R.L., Morse, R.L. and Taggart, K.A. (1977) "Growth and saturation of instability of spherical implosions driven by laser or charged particle beams". Nuclear Science and Engineering, **64**, 163-176.

McMaster, W.H. (1984) "Computer codes for Fluid-Structure interactions". In: ASME Pressure Vessel and Piping Conference, San Antonio, Texas.

McQueen, D.M. and Peskin, C.S. (2001) "Heart simulation by an Immersed Boundary method with formal second-order accuracy and reduced numerical viscosity". In: Mechanics for a New Millennium, Proceedings of the International Conference on Theoretical and Applied Mechanics (ICTAM) . Kluwer Academic Publishers, Dordrecht.

Menikoff, R. and Plohr, B.J. (1989) "The Riemann problem for fluid flow of real materials". Reviews of Modern Physics, **61**, 75-130.

Miller, L.A. and Peskin, C.S. (2004) "When vortices stick: an aerodynamic transition in tiny insect flight". The Journal of Experimental Biology, **207**, 3073-3088.

Mittal, R. and Iaccarino, G. (2005) "Immersed boundary method". Annual Review of Fluid Mechanics, **37**, 239-261.

- Monaghan, J.J. (1985) "Particle methods for hydrodynamics". Computer Physics Reports, **3**, 71-124.
- Monaghan, J.J. (1992) "Smoothed Particle Hydrodynamics". Annual Review of Astronomy and Astrophysics, **30**, 543-574.
- Monaghan, J.J. (1994) "Simulating free surface flow with SPH". Journal of Computational Physics, **110**, 399-406.
- Monaghan, J.J. (2005) "Smoothed particle hydrodynamics". Reports on Progress in Physics, **68**, 1703-1759.
- Morris, J. P., Fox, P. J. and Zhu Y. (1997) "Modeling low Reynolds number incompressible flows using SPH". Journal of Computational Physics, **136**, 214-226.
- Needham, D. and Hochmuth, R.M. (1990) "Rapid flow of passive neutrophils into a 4 mm pipet and measurement of cytoplasmic viscosity". Journal of Biomechanical Engineering, **112**, 269-276.
- Nomura, T. (1994) "ALE finite element computations of fluid-structure interaction problems". Computer Methods in Applied Mechanics and Engineering, **112**, 291-308.
- Ottosen, N. and Runesson, K. (1991) "Properties of discontinuous bifurcation solutions in elastoplasticity". Internal Journal of Solids and Structures, **27**, 401-421.
- Palermo, G., Joris, H., Derde, M.-P., Camus, M., Devroey, P. and van Steirteghem, A.C. (1993) "Sperm characteristics and outcome of human assisted fertilization by subzonal insemination and intracytoplasmic sperm injection". Fertility and Sterility, **59**, 826-835.
- Palermo, G., Joris, H., Devroey, P. and van Steirteghem, A.C. (1992) "Pregnancies after intracytoplasmic injection of single spermatozoon into an oocyte". Lancet, **340**, 17-18.
- Parker, K.K., Brock, A.L., Brangwynne, C., Mannix, R.J., Wang, N., Ostuni, E., Geisse, N.A., Adams, J.C., Whitesides, G.M. and Ingber, D.E. (2002) "Directional control of lamellipodia extension by constraining cell shape and orienting cell tractional forces". FASEB Journal, **16**, 1195-1204.
- Payne, D., Flaherty, S.P., Jeffery, R., Warnes, G.M. and Matthews, C.D. (1994) "Successful treatment of severe male factor infertility in 100 consecutive cycles using intracytoplasmic sperm injection". Human Reproduction, **9**, 2051-2057.
- Peskin, C.S. (1972) "Flow patterns around heart valves: a numerical method". Journal of Computational Physics, **10**, 220-252.
- Peskin, C.S. (1977) "Numerical analysis of blood flow in the heart". Journal of Computational Physics, **25**, 220-252.

Peskin, C.S. and McQueen, D.M. (1989) "A three-dimensional computational method for blood flow in the heart. I. Immersed elastic fibers in a viscous incompressible fluid". *Journal of Computational Physics*, **81**, 372-405.

Peskin, C.S. and McQueen, D.M. (1992) "Cardiac fluid dynamics. Critical Reviews in Biomedical Engineering". *SIAM Journal on Scientific and Statistical Computing*, **20**, 451-459.

Peskin, C.S. and McQueen, D.M. (1994) "Mechanical equilibrium determines the fractal fiber architecture of aortic heart valve leaflets". *American Journal of Physiology*, **266**, H319-H328.

Peskin, C.S. and McQueen, D.M. (1995) "A general method for the computer simulation of biological systems interacting with fluids". *Symposia of the Society for Experimental Biology Fluid Dynamics*, **49**, 265-276.

Peskin, C.S. and McQueen, D.M. (1996) "Fluid dynamics of the heart and its valves". In: *Case Studies in Mathematical Modeling-Ecology, Physiology, and Cell Biology*, Prentice-Hall, New Jersey.

Prasad, P. and Chou, C.C. (1989) "A review of mathematical occupant simulation models". In: *ASME Winter Annual Meeting, AMD-Vol 106, Crashworthiness and Occupant Protection in Transportation Systems*, San Francisco, California.

Redgment, C.J., Tang, D., Tsirigotis, M., Yazdani, N., Al Shawaf, T. and Craft, I.L. (1994) "Experience with assisted fertilization in severe male factor infertility and unexplained failed fertilization in vitro". *Human Reproduction*, **9**, 680-683.

Sawada, T. and Hisada, T. (2007) "Fluid-structure interaction analysis of the two-dimensional flag-in-wind problem by an interface-tracking ALE finite element method". *Computers & Fluids*, **36**, 136-146.

Schoenberg, I.J. (1946) "Contributions to the problem of approximation of equidistant data by analytic functions. Part A: on the problem of smoothing or graduation. A first class of analytic approximation formulae". *Quarterly of Applied Mathematics*, **4**, 45-99

Schreyer, H.L., Sulsky, D.L. and Zhou, S.J. (2002) "Modeling delamination as a strong discontinuity with the material point method. *Computer Methods in Applied Mechanics and Engineering*, **191**, 2483-2507.

Shen, L. and Chen, Z. (2005) "A Silent Boundary Scheme with the Material Point Method for Dynamic Analyses". *Computer Modeling in Engineering and Sciences*, **7**, 305-320.

- Shin, D. and Athanasiou, K. (1999) "Cytoindentation for obtaining cell biomechanical properties". *Journal of Orthopaedic Research*, **17**, 880-890.
- Skalak, R., Tozeren, A., Zarda, R.P. and Chien, S. (1973) "Strain Energy Function of Red Blood Cell Membranes". *Biophysical Journal*, **13**, 245-264.
- Stamenovic, D. and Ingber, D.E. (2002) "Models of cytoskeletal mechanics of adherent cells". *Biomechanics and Modeling in Mechanobiology*, **1**, 95-108.
- Step toe, P.C. and Edwards, R.G. (1978) "Birth after the reimplantation of a human embryo". *Lancet*, **2**, 366.
- Sulsky, D., Chen, Z. and Schreyer, H.L. (1991) "The application of a material-spatial numerical method to penetration". Sandia National Laboratories Technical Report, SAND91-7095.
- Sulsky, D., Chen, Z. and Schreyer, H.L. (1994) "A particle method for history-dependent materials". *Computer Methods in Applied Mechanics and Engineering*, **118**, 179-196.
- Sulsky, D., Zhou, S.J. and Schreyer, H.L. (1995) "Application of a particle-in-cell method to solid mechanics". *Computer Physics Communications*, **87**, 236-252.
- Sun, Y., Wan, K.-T., Roberts, K.P., Bischof, J.C. and Nelson, B.J. (2003) "Mechanical property characterization of mouse zona pellucida". *IEEE Transactions on Nanobioscience*, **2**, 279-286.
- Suresh, S., Spatz, J., Mills, J.P., Micoulet, A., Dao, M., Lim, C.T., Beil, M. and Seufferlein, T. (2005) "Connections between single-cell biomechanics and human disease states: gastrointestinal cancer and malaria". *Acta Biomaterialia*, **1**, 15-30.
- Swegle, J.W. and Attaway, S.W. (1995) "On the feasibility of using smoothed particle hydrodynamics for underwater explosion calculations". *Computational Mechanics*, **17**, 151-168.
- Takeuchi, S., Minoura, H., Shibahara, T., Shen, X., Futamura, N. and Toyoda, N. (2001) "Comparison of Piezo-Assisted Micromanipulation with Conventional Micromanipulation for Intracytoplasmic Sperm Injection into Human Oocytes". *Gynecologic and Obstetric Investigation*, **52**, 158-162.
- Tanaka, S. and Kashiwayama, K. (2006) "ALE finite element method for FSI problems with free surface using mesh re-generation method based on background mesh". *International Journal of Computational Fluid Dynamics*, **20**, 229-236.

Theret, D.P., Levesque, M.J., Sato, M., Nerem, R.M. and Wheeler, L.T. (1988) "The application of a homogeneous half-space model in the analysis of endothelial cell micropipette measurements". *Journal of Biomechanical Engineering*, **110**, 190-199.

Torres, D.J. and Brackbill, J.U. (2000) "The point-set method: Front-Tracking without connectivity". *Journal of Computational Physics*, **165**, 620-644.

Tsai, M.A., Frank, R.S. and Waugh, R.E. (1993) "Passive mechanical behavior of human neutrophils: power-law fluid". *Biophysical Journal*, **65**, 2078-2088.

van Steirteghem, A.C., Liu, J., Joris, H., Nagy, Z., Janssenswillen, C., Tournaye, H., Derde, M.-P., van Assche, E. and Devroey, P. (1993) "Higher success rate by intracytoplasmic sperm injection than by subzonal insemination. Report of a second series of 300 consecutive treatment cycles". *Human Reproduction*, **8**, 1055-1060.

van Vliet, K.J., Bao, G. and Suresh, S. (2003) "The biomechanics toolbox: experimental approaches for living cells and biomolecules". *Acta Materialia*, **51**, 5881-5905.

von Neumann, J. and Richtmyer, R.D. (1950) "A method for the numerical calculation of hydrodynamic shocks". *Journal of Applied Physics*, **21**, 232-237.

Waugh, R.E., Song, J., Svetina, S. and Zeks, B. (1992) "Local and nonlocal curvature elasticity in bilayer membranes by tether formation from lecithin vesicles". *Biophysical Journal*, **61**, 974-982.

Weaver, W., Timoshenko, S.P. and Young, D.H. (1990) "Vibration problems in engineering (5th Edition)". John Wiley & Sons, New York.

Wilkins, M.L. (1980) "Use of artificial viscosity in multidimensional fluid dynamics calculations". *Journal of Computational Physics*, **36**, 281-303.

Yanagida, K., Katayose, H., Yazawa, H., Kimura, Y., Konnai, K. and Sato, A. (1999) "The usefulness of a piezo-micromanipulator in intracytoplasmic sperm injection in humans". *Human Reproduction*, **14**, 448-453.

Yeung, A. and Evans, E. (1989) "Cortical shell-liquid core model for passive flow of liquid-like spherical cells into micropipets". *Biophysical Journal*, **56**, 139-149.

York II, A.R. (1997) "Development of modifications to the material point method for the simulation of thin membranes, compressible fluids, and their interactions". Sandia National Laboratories Technical Report, SAND97-1983.

Yun, G., Choi, H. and Kim, D. (2003) "Turbulent flow past a sphere at $Re = 3700$ and 10000 ". *Physics of Fluids*, **15**, S6.

- Zeman, K., Engelhard, H. and Sackman, E. (1990) "Bending undulations and elasticity of the erythrocyte membrane: effects of cell shape and membrane organization". *European Biophysics Journal*, **18**, 203-219.
- Zhang, L. and Gay, M. (2007) "Immersed finite element method for fluid-structure interactions". *Journal of Fluids and Structures*, **23**, 839-857.
- Zhang, L., Gerstenberger, A., Wang, X. and Liu, W.K. (2004) "Immersed finite element method". *Computer Methods in Applied Mechanics and Engineering*, **193**, 2051-2067.
- Zhang, L.T., Wagner, G.J. and Liu, W.K. (2003) "Modelling and simulation of fluid structure interaction by meshfree and FEM". *Communications in Numerical Methods in Engineering*, **19**, 615-621.
- Zhou, E.H., Lim, C.T., Tan, K.S.W., Quek, S.T., Lee, A. and Liao, B. (2004) "Investigating the progression of disease state of malaria-infected red blood cells using micropipette aspiration". In: *Proceedings of the Second World Congress for Chinese Biomedical Engineers*, Beijing, China.
- Zhu, C., Bao, G. and Wang, N. (2000) "Cell mechanics: mechanical Response, cell adhesion, and molecular deformation". *Annual Review of Biomedical Engineering*, **2**, 189-226.
- Zhu, L. and Peskin, C.S. (2003) "Interaction of two filaments in a flowing soap film". *Physics of Fluids*, **15**, 128-136.

APPENDIX 1

LINEAR INTERPOLATION SHAPE FUNCTIONS

Figure A1 presents a typical 8-node cell element used for the construction of the MPM background computational grid. The global coordinate system is denoted by x - y - z , and the corresponding logical coordinate system is defined as ξ - η - ζ with the origin set at node 1. The lengths of the element along x -, y - and z -direction are represented by Δx , Δy and Δz , respectively. Then, the logical coordinates of particle p inside the cell are computed as

$$\xi = \frac{x_p - x_1}{\Delta x}$$

$$\eta = \frac{y_p - y_1}{\Delta y}$$

$$\zeta = \frac{z_p - z_1}{\Delta z}$$

where subscripts p and 1 denote particle p and node 1.

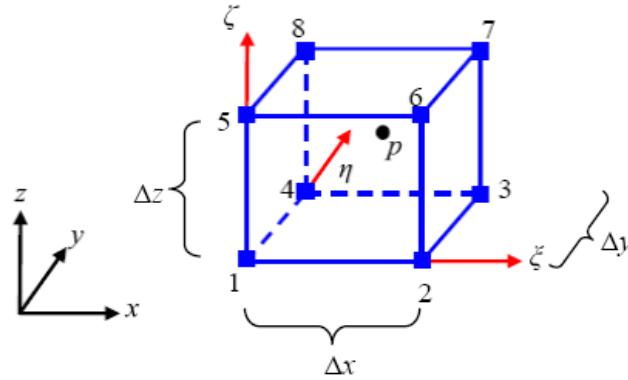


Figure A1 An 8-node cell element and the definition of the logical coordinate system

The eight linear shape functions over the cell domain are expressed as

$$N_1 = (1 - \xi)(1 - \eta)(1 - \varsigma)$$

$$N_2 = \xi(1 - \eta)(1 - \varsigma)$$

$$N_3 = \xi\eta(1 - \varsigma)$$

$$N_4 = (1 - \xi)\eta(1 - \varsigma)$$

$$N_5 = (1 - \xi)(1 - \eta)\varsigma$$

$$N_6 = \xi(1 - \eta)\varsigma$$

$$N_7 = \xi\eta\varsigma$$

$$N_8 = (1 - \xi)\eta\varsigma$$

and the derivatives of shape functions with respect to x , y and z are thus written as

$$\frac{\partial N_1}{\partial x} = -\frac{(1 - \eta)(1 - \varsigma)}{\Delta x}$$

$$\frac{\partial N_2}{\partial x} = \frac{(1 - \eta)(1 - \varsigma)}{\Delta x}$$

$$\frac{\partial N_3}{\partial x} = \frac{\eta(1 - \varsigma)}{\Delta x}$$

$$\frac{\partial N_4}{\partial x} = -\frac{\eta(1 - \varsigma)}{\Delta x}$$

$$\frac{\partial N_5}{\partial x} = -\frac{(1 - \eta)\varsigma}{\Delta x}$$

$$\frac{\partial N_6}{\partial x} = \frac{(1 - \eta)\varsigma}{\Delta x}$$

$$\frac{\partial N_7}{\partial x} = \frac{\eta\varsigma}{\Delta x}$$

$$\frac{\partial N_8}{\partial x} = -\frac{\eta\zeta}{\Delta x}$$

$$\frac{\partial N_1}{\partial y} = -\frac{(1-\xi)(1-\zeta)}{\Delta y}$$

$$\frac{\partial N_2}{\partial y} = -\frac{\xi(1-\zeta)}{\Delta y}$$

$$\frac{\partial N_3}{\partial y} = \frac{\xi(1-\zeta)}{\Delta y}$$

$$\frac{\partial N_4}{\partial y} = \frac{(1-\xi)(1-\zeta)}{\Delta y}$$

$$\frac{\partial N_5}{\partial y} = -\frac{(1-\xi)\zeta}{\Delta y}$$

$$\frac{\partial N_6}{\partial y} = -\frac{\xi\zeta}{\Delta y}$$

$$\frac{\partial N_7}{\partial y} = \frac{\xi\zeta}{\Delta y}$$

$$\frac{\partial N_8}{\partial y} = \frac{(1-\xi)\zeta}{\Delta y}$$

$$\frac{\partial N_1}{\partial z} = -\frac{(1-\xi)(1-\eta)}{\Delta z}$$

$$\frac{\partial N_2}{\partial z} = -\frac{\xi(1-\eta)}{\Delta z}$$

$$\frac{\partial N_3}{\partial z} = -\frac{\xi\eta}{\Delta z}$$

$$\frac{\partial N_4}{\partial z} = -\frac{(1-\xi)\eta}{\Delta z}$$

$$\frac{\partial N_5}{\partial z} = \frac{(1-\xi)(1-\eta)}{\Delta z}$$

$$\frac{\partial N_6}{\partial z} = \frac{\xi(1-\eta)}{\Delta z}$$

$$\frac{\partial N_7}{\partial z} = \frac{\xi\eta}{\Delta z}$$

$$\frac{\partial N_8}{\partial z} = \frac{(1-\xi)\eta}{\Delta z}$$

APPENDIX 2

RESEARCH PROJECTS UNDERTAKEN BY THE AUTHOR AT MU

1. Molecular Dynamics Simulation of the Size Effect of Carbon Nanotubes on the Bulk Modulus of a Lipid Bilayer

Abstract: Due to their nanoscale size and special features, carbon nanotubes could enter the human body via certain way. The growing use of carbon nanotubes in practical applications, hence, prompts a necessity to study the potential health risks of carbon nanotubes. A numerical study is performed in this paper to investigate the size effect of carbon nanotubes on the bulk modulus of a lipid bilayer by using the constant surface tension molecular dynamics simulation procedure. It is found that the size effect is not monotonic with the increase of nanotube length. An explanation is given on the basis of the atomic interaction between the nanotube and bilayer involved in the model system.

2. A Coupled Thermo-Mechanical Model for Simulating the Material Failure Evolution Due to Localized Heating

Abstract: A coupled thermo-mechanical constitutive model with decohesion is proposed to simulate the material failure evolution due to localized heating. A discontinuous bifurcation analysis is performed based on a thermoviscoplasticity relation to identify the transition from continuous to discontinuous failure modes as well as the orientation of the discontinuous failure. The thermo-mechanical model is then implemented within the framework of the Material Point Method (MPM) so that the different gradient and divergence operators in the governing differential equations could be discretized in a single computational domain and that continuous remeshing is not required with the evolution of failure. The proposed model-based simulation procedure is verified with analytical solutions available, and the potential of the proposed procedure is demonstrated by simulating the material failure evolution in a prestressed plate subject to laser irradiation.

3. A Continuum-Level Study of the Explosion Response of Copper Oxide/Aluminum Nanothermite Composites

Abstract: A constant- β equation of state for the explosion product of CuO/Al nanothermite composites is developed based on the CJ theory and experiments of the

nanothermite explosion. The equation of state is then implemented into a coupled CFD and CSD code via the Material Point Method for model-based simulation of the explosion response of a CuO/Al nanothermite pellet placed in a small well. The comparison between the experimental and simulation results demonstrates that the continuum theory could be used for modeling the CuO/Al nanothermite explosion response, and indicates that the large γ value for the nanothermite may be due to the multiphase nature of the nanocomposites.

VITA

Yong Gan was born on July 4, 1976, in Nanchang, Jiangxi Province, China. After attending public schools in Nanchang, he received B.E. in Structural Engineering in 1997 and M.S. in Engineering Mechanics in 2000 from Nanchang University. He entered Zhejiang University in Hangzhou, Zhejiang Province, China, in 2000 and received Ph.D. in Structural Engineering in 2003. He began his Ph.D. study with a special interest in Computational Mechanics in August 2003 at the University of Missouri-Columbia.